A Thesis Submitted for the Degree of PhD at the University of Warwick

http://go.warwick.ac.uk/wrap/61954

Development of an X-ray Excited Optical Luminescence Microscope (XEOM)

by

Matthew J. Hand

Thesis

Submitted to the University of Warwick

for the degree of

Doctor of Philosophy

Department of Physics

April 2014

THE UNIVERSITY OF
WARWICK

Contents

List of Tables

List of Figures

Acknowledgments

Of course, the most thanks must go to my supervisor, Prof. Mark Dowsett. Apart from providing me with invaluable guidance and support, without his tireless efforts in his mechanical workshop (read: garage) construction of the microscope would simply not have been possible. The input of our close colleague and my co-supervisor, Prof. Annemie Adriaens, is also greatly appreciated.

Thanks also to the beamline staff who acted as local contacts for their assistance in carrying out experiments: Paul Thompson (XMaS), Simon Brown (XMaS), Miguel Silveira (DUBBLE), and Sergey Nikitenko (DUBBLE). I'd like to give an extra special thanks to Paul who's creative thinking and willingness to offer support during beam times has been nothing short of extraordinary.

On a personal note, I'd like to thank Rosie Grayburn, Pieter-Jan Sabbe, and Alice Elia, not only for their assistance in carrying out work related to this project, but also for their moral support and for preventing me from going insane during beam times. I think it's true that a very unique bond develops between people after spending a week together working night shifts in the close confines of a synchrotron beamline. I also want to thank my fellow PhDers: Andy Grigg, Ben Green, and Steve Huband — it's been a tough ride. Finally, a heartfelt thanks go to my wife, Anne, for her understanding and support over the last few years.

Funding for the camera, filters, and lenses has been provided by Fonds Wetenschappelijk Onderzoek (FWO), Belgium. Additional funding has been provided by the Paul Instrument Fund, and the Engineering and Physical Sciences

Research Council (EPSRC).

Declarations

I declare that this thesis and the work presented in it are my own and represent my own original research. Wherever contributions of others are included, I have endeavoured to ensure that this is stated clearly and attributed with explicit references. No part of this thesis has been submitted for a degree or any other qualification to the University of Warwick or any other institution.

Abstract

X-ray excited optical luminescence (XEOL) refers to the trans-visible emission produced as a consequence of X-ray bombardment and provides an alternative detection method for X-ray absorption spectroscopy (XAS). Whereas XAS measured by conventional means (absorption, X-ray fluorescence) generally yields spectra characteristic of the bulk, the shallow escape depth of visible photons provides surface specificity of $\sim 200\,\text{nm}$. Combining this with the relative ease of manipulating the emission using conventional optics gives us the basis for a method of mapping surface chemical states on the micron scale — XEOL microscopy (XEOM).

As part of an ongoing project looking into the use of XEOL to study the chemical systems relevant to the corrosion of heritage artefacts, a portable XEOM instrument, XEOM1, has been constructed. Here, a detailed account of the development process is given, including descriptions of the microscope itself (optics, detectors, auxiliary hardware) and of its support system (control electronics and software). Data processing challenges are also discussed.

Testing of XEOM1 has involved deployment on multiple synchrotron beamlines and data acquired from samples comprising of corroded copper surfaces (coupons, meshes) are presented in order to demonstrate how XEOM1 can be used for surface chemical analysis. XEOL spectra have been obtained by acquiring image 'stacks' — each stack is sequence of images resolved in energy across an absorption edge — and extracting data from regions of interest (ROIs) in each image. Chemical identification is achieved through analysis of the near-edge structure (XANES). Subtraction of pre- and post-edge images also gives a method for fast elemental mapping. Several options for future development of the XEOM1 hardware and related investigations are also proposed.

Abbreviations

EIU	Electronics Interface Unit
ESRF	European Synchrotron Radiation Facility
EXAFS	Extended X-ray absorption fine structure
OPD	Optical path difference
OSLO	Optics Software for Layout and Optimization
PIXE	Particle-induced X-ray emission
SIMS	Secondary ion mass spectrometry
UVFS	UV-grade fused silica
XANES	X-ray absorption near-edge structure
XAS	X-ray absorption spectroscopy
XEOL	X-ray excited optical luminescence
XEOM	X-ray excited optical luminescence microscopy

Chapter 1

Introduction

1.1 Science for Protecting Our Cultural Heritage

Heritage science is no stranger to the use of analytical techniques to further our understanding of historical objects. By studying the composition and structure of the materials in heritage artefacts, information can be gained about their provenance and the techniques used to manufacture them. This in turn can give insights into the lives of those people who produced and used these objects. Such techniques are also used to study corrosion on heritage artefacts in order to develop protective treatments and to preserve them for future generations to appreciate. This thesis concerns the development of instrumentation for a novel surface chemical mapping technique for applications in this and other areas.

The most obvious and crucial requirement for a protective coating is that it is effective at passivating active corrosion and preventing further damage. Beyond this, there some further characteristics which are highly desirable if the coating is to be applied to a heritage artefact.

Removable/re-treatable

Treatment of an artefact can be a multi-stage process so to avoid adverse reactions between subsequent treatment stages, the previous protection system should be completely removed before moving onto the next. Similarly, as development of coatings continues, more effective methods may be found so it may be desirable to remove a less effective system in favour of a new one.

Preserve the aesthetics of the object

The field of cultural heritage is driven by a set of ethical concerns which define the acceptable practice when working with heritage artefacts. Except in very specific cases, it is undesirable for any protective coating to influence the look of an object in any significant way. This is especially true when the artefact is to be put on display.

Ease of application

It would not be unusual for application of a protective coating to be done by persons who do not have expertise in scientific methodology, which rules out the use of complex deposition techniques. An example of an ideal coating would be one which could be applied to smaller artefacts by simple dip coating, or to larger objects by 'painting' it on with a brush.

Cost and ease of manufacture

As funding for conservation is often very limited, cost is a major concern. Unusual, extremely high purity, or difficult to manufacture component compounds can be expensive and should be avoided. The process by which the treatment itself is produced should also be simple and inexpensive.

Safety

The use of highly toxic chemicals is undesirable. Apart from any health concerns, the cost of using such substances is driven up by the need for special containment equipment or extra personal protection equipment (PPE). Again, those without a practical scientific background will not possess the requisite knowledge for safely dealing with hazardous materials.

These requirements rule out the use of many commercially available systems used in modern engineering, where the surface appearance is generally not a concern, such as those which are not transparent or are difficult (if not impossible) to remove without damaging the underlying surface. Consequently, separate work needs to be done to develop protection systems which are not only effective, but also meet the strict demands imposed by their application to heritage artefacts. In order to achieve this, a good understanding of both the corrosion processes themselves, and the interaction between the coating and the corrosion products is needed.

Related to aforementioned ethical concerns, there are some characteristics which are desirable for any analytical technique which is to be applied to a heritage artefact. Highly invasive techniques should be avoided; that is, any method which requires that a large sample be removed from the artefact or requires that the object be placed in a harsh environment e.g. vacuum techniques. The technique should also be non-destructive if it is to be applied directly to an artefact — causing damage or discolouration is equally objectionable. In certain circumstances it can be acceptable to take a very small sample from a discreet location on the object, but the preference would be to avoid this.

Recent work in this area, undertaken by a collaboration between the Analytical Science Projects group at the University of Warwick and the Department of Analytical Chemistry at Ghent University, Belgium, has related to the development of protection systems (chemical coatings) for metallic artefacts. Such objects could be entirely metallic, such as a bronze coin, or have some metallic component, such as a steel knife which has a wooden handle. The latter is referred to as a composite. Specific metals of interest have been lead [1, 2], copper [3–5], and silver [6].

1.2 Analytical Techniques In Conservation Science

Modern scientists have a wide variety of analytical techniques at their disposal for materials analysis. However, the usefulness of any particular technique is highly dependent on both the sample characteristics and the type of information to be determined. As mentioned above, the unique nature of many historical objects places further limitations on the methods which can be applied in order to study them. The following is a brief overview of some of the more commonly used techniques and the characteristics which make them useful in the context of heritage science.

X-ray fluorescence spectroscopy (XRF)

Elemental composition is determined by measuring the spectrum of characteristic X-rays emitted by different elements in the sample when it is illuminated with a primary X-ray source. This is one of the most popular

Figure 1.1: *XRF analysis of a 16th-century salt cellar made of gold, ebony and enamel at the Kunsthistorische Museum, Vienna, Austria. Credit: Dean Calma / IAEA*

analytical techniques used in heritage science research. Several factors contribute to its appeal: (a) it is relatively inexpensive; (b) only a small amount of training is required in order to interpret the results; (c) very little equipment is required so it is suitable for even the smallest laboratories (Figure 1.1) — portable systems can even be taken into the field for in-situ analysis [7, 8].

Particle-induced X-ray emission spectroscopy (PIXE)

The same characteristic X-rays as recorded in an XRF spectrum are also measured in a PIXE spectrum, but the source of excitation is now a beam of high energy particles — typically these are protons with energy on the order of a few MeV. PIXE has several advantages over XRF including greater surface sensitivity due to the limited penetration depth of the particles (typically 10–50 μm), and it is better suited to measurement of elements with relatively higher characteristic X-ray energies due to larger interaction cross-sections and reduced detection limits resulting from lower background emission. For elements with $Z < 20$ the detection limits of PIXE increase rapidly, and the requirement of an accelerated particle source limits its flexibility [9]. PIXE analysis has been successfully applied to a wide variety of cultural heritage materials including metals, where PIXE combined with XRF allowed the authentication of Dacian gold bracelets [10], medieval stained glass [11], tapestries [12], and many more besides.

Secondary ion mass spectrometry (SIMS)

Mono-energetic primary ions (e.g. Ga^+, In^+, O_2^+, Cs^+) incident on the sample deposit kinetic energy in the solid surface. This initiates a collision cascade which leads to the liberation of atomic or molecular species from the surface of the sample. A fraction of these is ionized during the process, collected by an electric field, and focused into a mass spectrometer for analysis [13]. SIMS can provide trace analysis in the ppm–ppb range, and depth and lateral resolution on the nanometre scale (although not usually simultaneously). However, as with all forms of mass spectrometry, SIMS is inherently a destructive technique. In addition, measurements are performed *in vacuo* so the artefact must be vacuum-compatible, and should be no larger than a few millimetres in size or a sample must be taken [14]. Further examples of the use of SIMS in heritage science include the analysis of painting cross-sections [15] and depth profiling of replica Venetian glassware [16].

X-ray absorption spectroscopy (XAS)

Being fundamental to this thesis, X-ray absorption spectroscopy will be covered in much more detail in subsequent chapters. Nevertheless, it is useful to note for now that by monitoring the element-specific absorption of X-rays in a sample, it is possible to determine details about the local bonding environment. In this way it moves beyond determination of elemental composition and allows for chemical and structural properties to be probed. A prominent use of XAS in heritage science was in the preservation of the seventeenth-century warship *Vasa*, where XAS of sulphur led to the discovery of routes for formation of sulphuric acid in the wooden hull [17]. This study has profound impact on procedures and guidelines for marine archaeology.

X-ray diffraction (XRD)

X-ray diffraction is a fundamental tool in solid state research. Its intrinsic sensitivity to long-range order and symmetry in crystals make it useful not only for identification of compounds, but also for structural analysis of the sample. This includes the texture and orientation of crystalline phases, and the microstructure of the material in terms of crystallite size [18]. The complexity of cultural heritage material resulting from degradation, contamination, and alteration can lead to equally complex diffraction patterns making analysis challenging. However, it has been successfully used in the characterization of Romanesque wall paintings [19], and as a tool for in-situ monitoring of conservation coatings for heritage lead [20].

Analytical chemistry

There are several aspects to the application of analytical chemistry techniques to cultural heritage science, and electrochemical techniques are employed in many instances [21]. The first is their use for active investigation of chemical processes whereby corrosion is induced in the sample through application of an electrochemical potential — for example, anodic polarization has been used to identify chloride-induced corrosion mechanisms in quaternary bronze [22]. Another aspect is their use for monitoring of chemical treatments; monitoring of the corrosion potential has been used to evaluate the effectiveness of storage and stabilization methods applied to archaeological copper artefacts [3]. Finally, they can be used as a direct treatment method, as demonstrated through the electrolytic stabilization of iron cannon recovered from an eighteenth-century frigate [23].

Nowadays, in order to extract as much information as possible, it is common for a multi-analytical approach to be taken whereby a number of complementary techniques are applied to a given sample. For a detailed reviews of analytical techniques as applied to cultural heritage materials, including many others not mentioned here, the reader is referred to [24] and [25].

1.3 A Microscope on the Past

As mentioned above, one of the more commonly used analytical techniques to be used for analysis of heritage artefacts is XRF. Spot analysis can be useful in itself, but it is often desirable to know how the composition varies across the surface. By scanning the XRF probe across an area of the sample and recording the spectrum at each point, an elemental map can be produced. While this can be done in a laboratory, the relatively low intensity X-ray sources available require dwell times of typically 5–10 s pixel^{-1}; to scan a 30 cm^2 at 1 mm resolution will take 5 to 10 days (recent developments [26] in this area utilizing multiple detectors reduce this by approximately a factor of 10). However, extremely fast results can be obtained by carrying out the same analysis using a synchrotron X-ray source, which can generate an X-ray flux many orders of magnitude greater than a laboratory source, reducing the scanning time to a matter of hours.

While it is clear that XRF mapping is an extremely useful technique, its characteristics can reduce its suitability in certain situations. The penetration depth of the X-ray probe is difficult to control and highly dependent on the sample composition. The need to use relatively high energy X-rays (up to $\sim$ 50 keV) in order to excite a wide range of elements leads to penetration depths of tens or even hundreds of microns (although this very feature has been used to great effect to reveal hidden artworks by great painting masters such as Van Gogh [27, 28] and Rembrandt [29]). However, for extremely thin corrosion layers, the detected signals will be dominated by those originating from the bulk material and possibly overwhelming the comparatively small surface signal. A further limitation is that no information on the chemical form of the elements is obtained. Corrosion, by its very nature, is formed from compounds of the base materials in an artefact. Inferences can be made from XRF analyses about the existence of specific corrosion products, especially if the environmental factors are known, but without complementary techniques the results cannot be definitive.

In principle, an alternative technique capable of overcoming both of these limitations is a form of X-ray absorption spectroscopy (XAS) known as X-ray excited optical luminescence (XEOL)[1]. This synchrotron-based technique utilizes

---

[1] Strictly speaking, XEOL refers to the emission process itself which can be measured as a function of either excitation energy or emission wavelength, but here a 'XEOL spectrum' always

the optical luminescent emission resulting from X-ray bombardment to probe the chemical structure of a sample. Detection of X-ray absorption in this manner gives enhanced surface specificity for opaque materials as a consequence of the shallow escape depth of visible photons. However, the property of primary interest for this project is the comparative ease with which the optical emission can be manipulated using conventional optics. This naturally leads to the concept of imaging the surface in order to obtain a chemical map of the corrosion products. The process of acquiring chemical data from XEOL microscopy usually requires that a series of images, hereafter referred to as a 'stack', be acquired as the X-ray source energy is swept across an 'absorption edge' — a sharp rise in absorption when the X-ray excitation energy exceeds the binding energy of an atomic shell. It is in spectra extracted from these images stacks that the chemical information is encoded. A difficulty of the technique is that interpretation of these spectra is can be a significant challenge, and a full treatment requires the use of a sophisticated modelling and fitting procedure. However, XAS spectra are far richer in chemical information so there is potential to gain a much deeper insight into the corrosion systems. An additional requirement for XEOL is the use of a tunable X-ray source so analyses must[2] be carried out at synchrotron radiation facility. While this currently precludes the possibility of developing a XEOL microscope for the field until a tunable and portable X-ray source is developed, it still provides an alternative to synchrotron-based XRF analyses.

1.4 Thesis Scope

The work presented in this thesis is part of a project looking into the use of XEOL to study the chemical systems relevant to the corrosion of heritage artefacts. Previously, a portable optically-detected X-ray absorption spectrometer, known as ODXAS1 [30, 31], was constructed and has successfully been used to carry out XEOL spectroscopy analysis. The aim of this project has been to take the next logical step of building a complete XEOL imaging system based on the concept described above.

---

refers to an optically-detected X-ray absorption spectrum.

[2] While it is possible to perform XAS experiments using a laboratory X-ray source, this is very rarely done as the advantages in speed and flexibility provided by a synchrotron source are so considerable.

Contained herein is an account of the development process for the X-ray exited optical luminescence microscope (XEOM), referred to hereafter as XEOM1. This has included the design of a bespoke optical system, integration of a variety of control and measurement systems, including two CCD spectroscopy cameras, and implementation of a software control solution which synchronizes operation of XEOM1 with synchrotron beamline systems. The complete microscope system has been deployed during multiple beam time allocations at which the X-ray absorption data presented here were acquired.

In addition to giving a complete description of the device and its control system, this thesis sets out to answer the following questions:

- Will spectra produced from an image stack be of high enough quality for chemical analysis?
- How does the visible yield compare with fluorescent X-ray yield and what effect do the respective detector characteristics have on the resulting spectra?
- With the potential for generation of hundreds of images and spectra, how can all this data be handled in a practical manner?
- How long will a typical measurement take, i.e. what is the potential for measuring fast chemical processes?
- Is it feasible to perform spectroelectrochemical imaging experiments similar to those previously carried out using ODXAS1, i.e. use in conjunction with an electrochemical cell?

As will be shown, problems with certain aspects of the build — in particular, the CCD sensors and optical filters — have caused considerable setbacks. Many issues have been at least partially solved, but some developments which were originally planned have not yet been implemented. Nevertheless, significant steps towards answering these questions and more have been made, and the instrument in its current state serves a solid foundation for continued development.

1.5 Summary

In this first chapter the use of analytical techniques for heritage science has been introduced, and restrictions on their use imposed by the unique nature of historical objects have been outlined. An overview of some techniques commonly used in this area has also been given. The concept of XEOL microscopy has been introduced and the potential key benefits over the commonly used XRF mapping technique have been highlighted. Finally, an overview of the areas which will be covered in the remainder of the thesis has been given.

References

[1] A Adriaens, et al. Growth and real time corrosion resistance monitoring of lead decanoate coatings. *Appl. Surf. Sci.*, 254(22):7351–7355, 2008.

[2] K De Wael, et al. Electrochemical deposition of dodecanoate on lead in view of an environmentally safe corrosion inhibition. *J. Solid State Electrochem.*, 14(3):407–413, March 2009.

[3] K Leyssens, et al. Study of corrosion potential measurements as a means to monitor the storage and stabilisation processes of archaeological copper artifacts. *Proc. Met. 2004*, pages 332–343, April 2004.

[4] K Leyssens, et al. Simultaneous in situ time resolved SR-XRD and corrosion potential analyses to monitor the corrosion on copper. *Electrochem. Commun.*, 7(12):1265–1270, 2005.

[5] A Adriaens, et al. Insights into electrolytic stabilization with weak polarization as treatment for archaeological copper objects. *Anal. Bioanal. Chem.*, 387(3):861–8, 2007.

[6] M G Dowsett, et al. The use of ultra-low-energy dynamic SIMS in the study of the tarnishing of silver. *Nucl. Instrum. Meth. B*, 239(1-2):51–64, 2005.

[7] R Cesareo, et al. Portable equipment for energy dispersive X-ray fluorescence analysis of Giotto's frescoes in the Chapel of the Scrovegni. *Nucl. Instrum. Meth. B*, 213:703–706, 2004.

[8] C R Appoloni, et al. Study of the pigments elementary chemical composition of a painting in process of attribution to Gainsborough employing a

portable X-rays fluorescence system. *Nucl. Instrum. Meth. A*, 580:710–713, 2007.

[9] H R Verma. *Atomic and Nuclear Analytical Methods*. Springer, 2007.

[10] B Constantinescu, et al. Micro-SR-XRF and micro-PIXE studies for archaeological gold identification - The case of Carpathian (Transylvanian) gold and of Dacian bracelets. *Nucl. Instrum. Meth. B*, 266(10):2325–2328, May 2008.

[11] M Vilarigues and RC da Silva. Ion beam and infrared analysis of medieval stained glass. *Appl. Phys. A Mater. Sci. Process.*, 79(2):373–378, July 2004.

[12] A Manhitaa, et al. Rediscovering the materials of Arraiolos tapestries: fibre and mordant analysis by SEM-EDS and μ-PIXE. *Microsc. Microanal.*, 14: 91–94, 2008.

[13] M G Dowsett and A Adriaens. The role of SIMS in cultural heritage studies. *Nucl. Instrum. Meth. B*, 226(1-2):38–52, 2004.

[14] A Adriaens and M G Dowsett. Applications of SIMS to cultural heritage studies. *Appl. Surf. Sci.*, 252(19):7096–7101, 2006.

[15] K Keune and J J Boon. Imaging secondary ion mass spectrometry of a paint cross section taken from an early Netherlandish painting by Rogier van der Weyden. *Anal. Chem.*, 76(5):1374–85, March 2004.

[16] S Fearn, D S McPhail, and V Oakley. Room temperature corrosion of museum glass: an investigation using low-energy SIMS. *Appl. Surf. Sci.*, 231-232:510–514, June 2004.

[17] M Sandström, et al. Deterioration of the seventeenth-century warship Vasa by internal formation of sulphuric acid. *Nature*, 415(6874):893–7, February 2002.

[18] G Artioli. Science for the cultural heritage: the contribution of X-ray diffraction. *Rend. Fis. Acc. Lincei*, 24(S1):55–62, October 2012.

[19] N Salvadó, et al. The use of combined synchrotron radiation micro FT-IR and XRD for the characterization of Romanesque wall paintings. *Appl. Phys. A*, 90(1):67–73, August 2007.

[20] R Grayburn, et al. Time-lapse synchrotron X-ray diffraction to monitor conservation coatings for heritage lead in atmospheres polluted with oak-emitted volatile organic compounds. *Corros. Sci.*, 82:280–289, 2014.

[21] A Doménech-Carbó, M T Doménech-Carbó, and V Costa. *Electrochemical*

Methods in Archaeometry, Conservation and Restoration. Springer, 2009.

[22] O Papadopoulou, et al. Surface and interface investigation of electrochemically induced corrosion on a quaternary bronze. *Surf. Interf. Anal. (early web access)*, March 2014.

[23] E Guilminot, et al. Electrolytic treatment of archaeological marine chloride impregnated iron objects by remote control. In *Met. '07*, 2007.

[24] K Janssens and R Van Grieken, editors. *Non-destructive micro analysis of cultural heritage materials*, volume 42. Elsevier Science, 2004.

[25] P Dillmann, et al., editors. *Corrosion and Conservation of Cultural Heritage Metallic Artefacts*. Woodhead Publishing, 2013.

[26] M Alfeld, et al. Optimization of mobile scanning macro-XRF systems for the in situ investigation of historical paintings. *J. Anal. At. Spectrom.*, 26 (5):899, 2011.

[27] M Alfeld, et al. Scanning XRF investigation of a Flower Still Life and its underlying composition from the collection of the Kröller-Müller Museum. *Appl. Phys. A*, January 2013.

[28] J Dik, et al. Visualization of a lost painting by Vincent van Gogh using synchrotron radiation based X-ray fluorescence elemental mapping. *Anal. Chem.*, 80(16):6436–42, 2008.

[29] M Alfeld, et al. Visualizing the 17th century underpainting in Portrait of an Old Man by Rembrandt van Rijn using synchrotron-based scanning macro-XRF. *Appl. Phys. A*, December 2012.

[30] M G Dowsett, et al. Optically detected X-ray absorption spectroscopy measurements as a means of monitoring corrosion layers on copper. *Anal. Chem.*, 80(22):8717–24, 2008.

[31] A Adriaens, et al. Real time observation of X-ray induced surface modification using simultaneous XANES and XEOL-XANES. *Anal. Chem.*, 85(20): 9556–9563, 2013.

Chapter 2

Background & Theory

Apart from the microscope itself, the most important piece of equipment used to complete the work in this project was the synchrotron. Without this, most of the techniques described here would be extremely impractical, if not impossible. This chapter begins with a brief description of synchrotron radiation and how it is generated for use as a physical probe. This is followed by a more detailed description of X-ray absorption spectroscopy and X-ray excited optical luminescence, the specific XAS variant which was used during this project. A history of XEOL as an analytical tool is given, including work completed at the University of Warwick on ODXAS1, the precursor instrument to XEOM1. Further information on the topics covered in Sections 2.1 and 2.2 can be found in [1–3].

2.1 Synchrotron Radiation

When a charged particle is accelerated, commonly achieved in practice by application of a magnetic field, it naturally emits electromagnetic (EM) radiation. The most relevant case to this discussion is that of an electron moving through a magnetic field applied perpendicular to the direction of motion of the electron, generating a Lorentz force (hence acceleration) orthogonal to both the field and velocity vectors. At sub-relativistic speeds this leads to emission with a dipole radiation pattern, but in the relativistic regime the profile shifts dramatically to a distribution which is strongly forward-peaked in the direction of the instantaneous velocity of the particle (Figure 2.1). The wavelength of the emission is highly compressed, a consequence of the relativistic Doppler effect. If the emission of a highly energetic electron (> 1 GeV) is observed directly along its axis, the electromagnetic radiation will be in the X-ray regime.

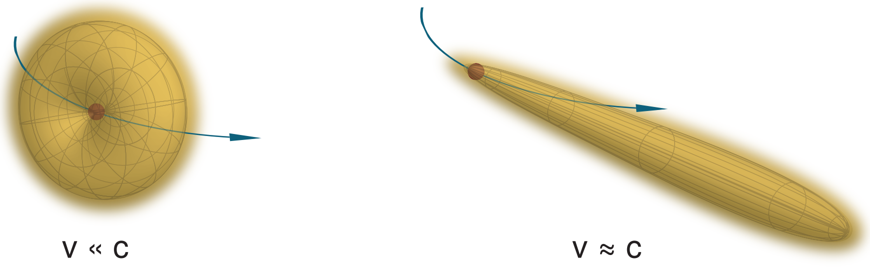

Figure 2.1: *An accelerating charged particle travelling at a sub-relativistic speed emits electromagnetic radiation with a dipole pattern. In contrast, a particle moving at a relativistic velocity, i.e. only a very small amount less than the speed of light, will emit EM radiation in a very narrow cone parallel to its instantaneous velocity vector.*

The first observation of this intense emission was in 1947 from the 70 MeV electron synchrotron (hence *synchrotron radiation*) at the General Electric Research Laboratory, New York, USA. It was initially regarded as a nuisance, an unavoidable energy loss mechanism in particle accelerators. However, an investigation by Tomboulian and Hartman in 1956 [4] showed the potential utility of synchrotron radiation, and in 1961 the Synchrotron Ultraviolet Radiation Facility (SURF I) opened its doors. First-generation synchrotron radiation sources, including SURF I, were built onto accelerators which were still primarily designated for high energy or particle physics, so were often referred to as *parasitic* facilities. It was not until the development of efficient electron storage rings (Figure 2.2) for long-term operation, that facilities designed specifically for the generation of synchrotron radiation were constructed. The first of these so-called second-generation facilities was the 2 GeV Synchrotron Radiation Source (SRS) at Daresbury, UK, completed in 1981 [5]. The *bending magnets* (discussed further below) used to guide the electrons in their orbit also acted as the primary sources of synchrotron radiation. Since then, advances in storage ring magnet technology has led to the development of so-called *insertion devices*. Placed in straight sections between the curved arcs of the storage ring, these manipulate the electron beam to optimize the source *brilliance* (photon flux per unit frequency, surface area, and solid angle). The inclusion of such insertion devices defines the third generation of synchrotron radiation sources, the first of which to be completed was the European Synchrotron Radiation Facility (ESRF) in Grenoble, France in 1994. With an electron storage ring operating energy of 6.04 GeV, it is the most energetic dedicated synchrotron radiation source in Europe. All the synchrotron experiments related to the project which will be discussed here have been carried out at this facility. More recently constructed third-generation facilities continue to improve on the performance of older sources in all areas: brilliance, and both spatial resolution (smaller beam footprint) and energy resolution (high degree of monochromaticity). Beyond these, a new fourth generation of synchrotron sources defined by even greater brilliance and coherence is becoming a reality. Candidates for such sources include energy recovery linacs (ERLs) and free electron lasers (FELs). A further 3 to 10 orders of magnitude in peak brilliance could potentially be gained over a modern third generation source [6].

2.1.1 Synchrotron Radiation Facilities

The discussion of dedicated synchrotron radiation facilities will focus on the characteristics and features common to modern third generation sources. Synchrotron radiation is generated by electrons which are forced to orbit in a closed path by an array of magnets (the ‘magnet lattice’) at energies in the gigaelectronvolt range. The source of electrons is usually a hot filament in an electron gun which generates electrons by thermionic emission. A linear accelerator (linac) accelerates the electrons up to around 100 MeV. Electrons from the linac travel into a booster synchrotron which further accelerates them up to the energy of the storage ring. From here, the electrons are injected into the storage ring to maintain its operating current. This occurs periodically, usually when the current falls below about $1 - \frac{1}{e} \approx 70\%$. During injection, user experiments must usually be suspended because (at the very least) the insertion devices must be opened up, otherwise their magnetic fields would perturb the electrons too much and cause spontaneous ‘beam dump’. Recent advances in this area allow for ‘top-up’ operation at some synchrotron facilities — including the current UK synchrotron, Diamond Light Source [7] — whereby electrons are quasi-continuously injected into the storage ring. Apart from the obvious advantage of allowing for continuous operation, this also reduces the thermal stress on beamline optics resulting from repeated changes in X-ray intensity.

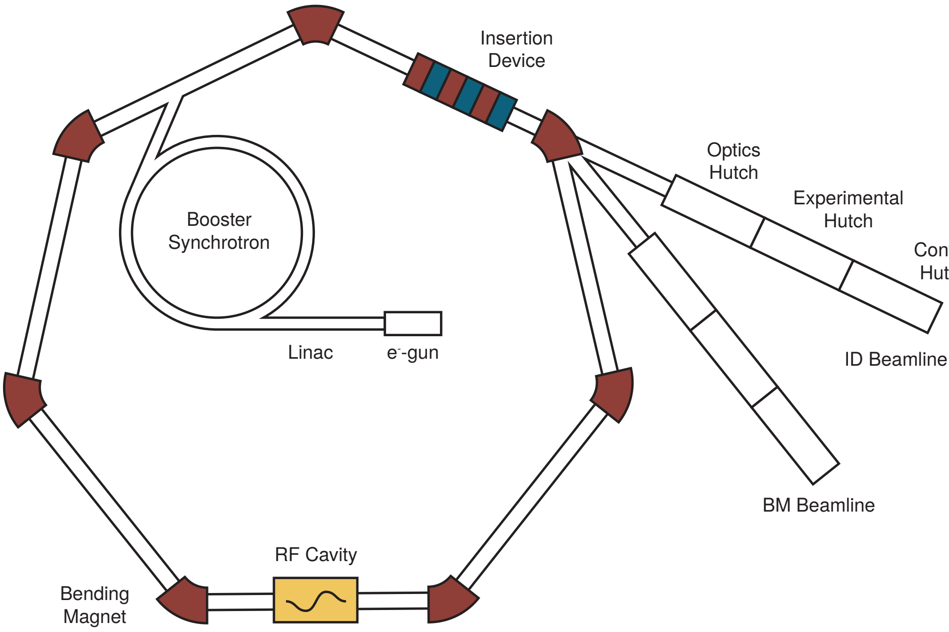

Figure 2.2: *Schematic illustration of the arrangement of the major components of a modern third generation synchrotron radiation facility (not to scale). The total circumference of the storage ring is often hundreds of metres with beamlines typically* 10–30 m *in length. In reality, the number of straight sections is much greater than shown here — the ESRF has 32, for example.*

The storage ring itself maintains the electrons in a closed orbit primarily by the use of dipole or 'bending' magnets to change their direction of travel. Other types of magnet are used to preserve the stability of the electron orbit: quadrupole magnets focus the electrons to counteract Coulomb repulsion, and sextupole magnets correct the chromatic aberration introduced by the focusing quadrupoles. An ultra-high vacuum (UHV) is maintained in the storage ring to minimize loss of electrons from collisions with gas molecules. Synchrotron radiation is emitted when the electrons pass through both the bending magnets and, as previously mentioned, the insertion devices placed between the bending magnets.

Bending magnets

Synchrotron radiation produced at a bending magnet is emitted in a flattened cone as the pencil-like beam sweeps around the curve like a searchlight. The cone angle is determined by the angular change in path of the electrons, plus a small amount due to the natural photon beam divergence given by $\theta \sim 1/\gamma$, where γ is a dimensionless parameter known as the Lorentz factor given by $\gamma = E/mc^2$, with E the storage ring energy, and mc^2 the electron rest mass energy (511 keV). For typical storage ring energies θ is in the range 0.06–0.5 mrad. The narrow beam passes the beamline aperture in a time Δt which, from the general property of Fourier transforms, leads to a characteristic critical frequency ω_c. Therefore, the emitted spectrum of bending magnet radiation is very broad with a sharp cut-off in spectral intensity for photon frequencies greater than $\omega_c \sim \gamma^3\omega$, where ω is the angular frequency of the electron orbit. A photon flux of 10^{12}–$10^{14}\,\mathrm{s}^{-1}$ could be expected from a bending magnet source, some 4–5 orders of magnitude greater than a laboratory source.

Insertion devices

Insertion devices (IDs) are placed in the straight sections of the storage ring and generate the highest photon fluxes at a third-generation facility. The two types of ID both operate by forcing the electron beam to deviate from a straight path in an oscillatory fashion and are distinguished by the amplitude of these oscillations. In a *wiggler* the excursions are larger than the natural opening angle γ^{-1} so the radiation emitted from each 'wiggle' does not overlap and the spectral characteristics are similar to a bending magnet, but with $2N$ greater intensity, where N is the number of periods of oscillation. The oscillations in an *undulator* are smaller than γ^{-1} so the radiation cones overlap and interfere. In this case, the spectrum has extremely intense peaks at frequencies where the interference is constructive. Brown et al. [8] give a more detailed description of both wigglers and undulators.

Synchrotron radiation emission causes the electrons in the storage ring to lose energy. To prevent them from spiralling into the inner wall and being lost, radio frequency (RF) cavities replenish the energy of the electrons each time they pass through. Rather than trying to inject electrons in the correct phase of the RF voltage cycle, one simply relies on the self-equilibrating nature of the system. To maintain a stable path, the electrons must be given a certain boost eV_{ref}. If an electron is travelling too slowly it will arrive late and receive a greater boost, if it is travelling too fast it will arrive early an receive a smaller boost. Any electrons arriving outside this range will not gain the correct boost and be lost. When running 'normally' the electron beam structure consists of evenly spaced bunches, but different bunch structures are often used to suit certain types of experiment. In single bunch mode, as the name implies, only one bunch of electrons circulates the ring. This allows time-resolved experiments to be synchronized with the bunch passing the beamline. Hybrid modes, where some bunches are dropped, produce a reasonable compromise with beam flux for most users, while still allowing for time-resolved experiments to be synchronized with an isolated bunch.

Beamlines, constructed tangentially to the storage ring, are where users carry out their experiments. A single beamline will capture synchrotron radiation from either a bending magnet or an insertion device though its *front end*, the interface with the storage ring. This section of the beamline is heavily shielded (by $\sim$ 1 m of concrete) against radiation which includes X-rays not captured by the primary aperture, and *Bremsstrahlung* (braking radiation) in the gamma regime (up to the storage ring energy) produced as electrons are lost from the orbit and strike the internal walls. It also acts to isolate the storage ring against loss of vacuum in the beamline. This is followed by the X-ray optics which guide the beam to the sample location in the experimental hutch. A monochromator — a Si(111) double crystal monochromator, for example — is used to isolate a very narrow bandwidth of X-rays, as little as 0.1 eV. Apart from the high source brilliance, the ability to tune the X-ray beam over a wide energy range is the other primary advantage synchrotron radiation facilities have over laboratory sources. X-ray mirrors are commonly used to direct and focus the beam. Other X-ray optical components, such as zone plates, compound refractive lenses (CRLs), and capillaries can also be used as focusing elements. The types of experiment the beamline has been designed to carry out determines the precise configuration of X-ray optical components, and also the equipment available to users at each end station. Details of the specific beamlines used during this project are given as part of the experimental setup in Section 4.1. As users cannot enter the experimental hutch while the beam is ‘on’ due to the extreme radiation hazard, all the beamline components are controlled remotely. The high level of computer control allows for sophisticated automation of many types of experiment. In this regard, the components of XEOM1 must be treated like any other beamline system with similar remote control and synchronization requirements.

2.1.2 Natural Sources of Synchrotron Radiation

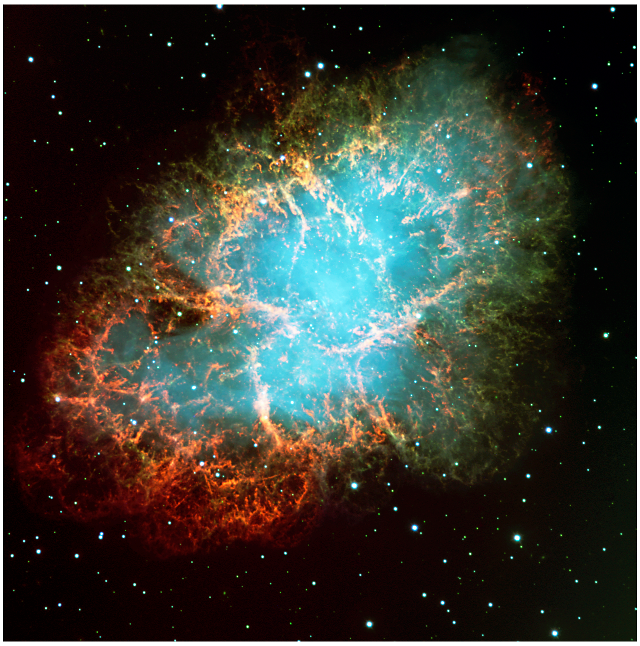

Figure 2.3: *Three colour composite image of the Crab nebula observed with the FORS2 instrument for the Very Large Telescope (VLT) at the European Southern Observatory (ESO). The blue light is primarily a result of synchrotron emission. Credit: ESO*

The generation of synchrotron radiation is not limited to man-made particle accelerators. Some classes of astronomical body emit synchrotron radiation as a consequence of charged particles being accelerated by strong magnetic fields. Perhaps the most observed astronomical body outside our solar system, the Crab nebula (Figure 2.3), was the first confirmed astrophysical source of synchrotron radiation [9]. The Crab pulsar, located inside the remnant of supernova

SN 1054, generates a pulsar wind which accelerates electrons and positrons to energies as high as $\sim 10^4$ TeV. The observed synchrotron radiation is emitted from this relativistic plasma moving through the magnetic field generated by the pulsar. Other astronomical features which can at least partly be attributed to synchrotron radiation are the non-thermal emission from active galaxies, and gamma-ray bursts (GRBs).

2.2 X-ray Absorption Spectroscopy

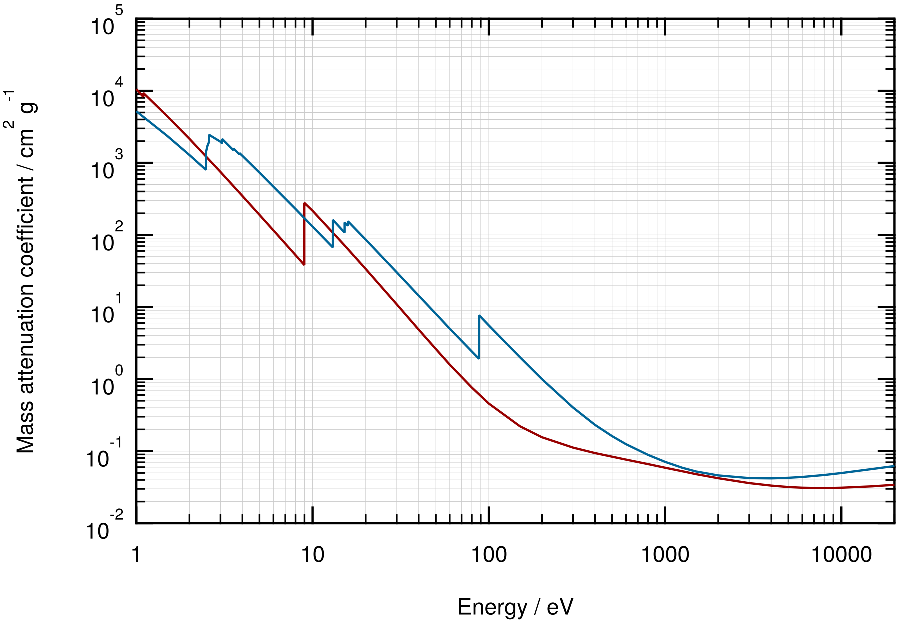

Figure 2.4: *The mass attenuation coefficient μ/ρ for copper (red curve) and lead (blue curve) as a function of photon energy. Data from http://www.nist.gov/pml/data/xraycoef/.*

X-ray absorption spectroscopy (XAS) refers to a set of techniques which can be used to analyse the local environment around an atom of a selected element within a material. XAS measurements of materials which possess little or no long-range order are possible: amorphous systems, glasses, liquids, molecular gases and more. The basic physical quantity measured in XAS is the X-ray attenuation coefficient $\mu(E)$ which describes how strongly X-rays are attenuated as a function of their energy. Two effects contribute to $\mu(E)$: scattering and photoelectric absorption. The scattering part is due to Rayleigh (elastic) and Compton (inelastic) scattering of X-rays, and photoelectric absorption is the ionization of an inner-shell electron. In general, $\mu(E)$ decreases smoothly with increasing X-ray energy, approximately as $1/E^3$. However, at characteristic energies a sharp rise in absorption is observed (illustrated in Figure 2.4). These occur when the X-ray photon has sufficient energy to liberate an electron from a core-level bound state within the atom. Each rise is known as an absorption edge, and it is the spectral features in the vicinity of these edges which provide the structural and chemical information. Importantly, XAS is element specific as the X-ray absorption edge energies of different elements have different energies. The absorption edges are denoted by the core electron state being excited — the K-edge corresponds to excitation of a $1s$ electron, the L_1, L_2, and L_3 edges correspond to excitation of $2s$, $2p_{1/2}$, and $2p_{3/2}$ electrons respectively, and so on. Moreover, the position of the edge is shifted by up to several eV depending on the oxidation state of the atom, in a compound specific manner.

2.2.1 Principles of X-ray Absorption

X-rays interact with matter in numerous ways, but the process which underpins XAS is the photoelectric effect. When an atom absorbs a sufficiently energetic photon a core electron is ejected into a continuum state. The loss of a core electron leaves the absorbing atom in an excited state which can relax via several different mechanisms, the most significant of these being X-ray fluorescence and Auger electron emission (Figure 2.5). The probability of each decay mechanism is dependent on excitation energy; Auger emission is usually dominant at lower energies, but fluorescent X-ray yields approach 1 at higher energies i.e. those appropriate for excitation of K-shell electrons in elements with $Z > 40$. Relaxation times are on the femtosecond scale. Both relaxation mechanisms begin with the transition of an electron from a more weakly bound shell to fill the core hole, but the subsequent process by which the resulting excess in energy is removed from the atom is different in each case.

If the atom relaxes via fluorescence, a photon is emitted with energy equal to the difference between the two electron energy levels involved in the transition. The available transitions are determined by quantum mechanical selection

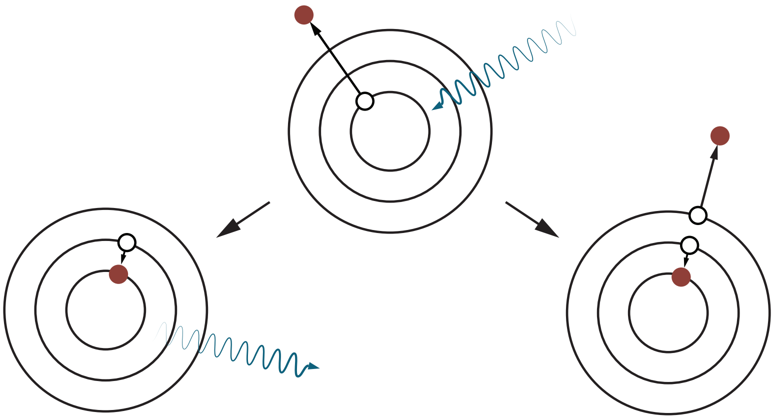

Figure 2.5: *The core hole left behind after ejection of a photoelectron is filled when an electron from a higher shell 'falls down' to the core level. The excess energy from this transition is either converted into a photon (fluorescence) or transferred to another electron causing it too to be ejected from the atom (Auger emission).*

rules for electric dipole radiation, namely $\Delta l = \pm 1$; $\Delta s = 0$; $\Delta j = 0, \pm 1$ (but not $0 \rightarrow 0$), where l and s are the orbital angular momentum and spin quantum numbers respectively, and j is their vector sum i.e. $\mathbf{j} = \mathbf{l} + \mathbf{s}$. Hence, for example, a transition from the 2s to 1s level is *forbidden*. The nomenclature for X-ray fluorescence emission is based on the initial and final states of the electron undergoing a transition. For example, K_α and K_β refer to transitions of the electron to the 1s state ($n = 1$, $l = 0$, $s = \pm 1/2$) from the L and M shells respectively. With sufficiently high energy resolution, these can be further resolved to transitions from different split energy levels resulting from spin-orbit coupling. Since the electron energy levels (and their differences) are specific to each element, the fluorescence emission can be used for compositional analysis, as described in Section 1.3.

Fluorescence can be excited not only by X-rays, but also by energetic charged particles. In fact, the most common types of laboratory X-ray source produce photons by accelerating electrons into a metal anode to excite the core level transitions. The characteristic emission lines are observed, but they sit on a background of Bremsstrahlung (braking) radiation produced as the electrons rapidly decelerate inside the target material. The overall emission intensity is limited by the current which can be passed through the target i.e. by heat generation. Rotating anodes improve this situation, but the brilliance of a laboratory source is still many orders of magnitude lower than a synchrotron, and the photon frequency is restricted by the source material used.

In contrast to fluorescence, Auger emission is a non-radiative process whereby the energy remaining from the initial outer shell electron relaxation is carried away by a second electron which is itself ejected from the atom. The excess energy is given by $|E_c - E_n|$, where E_c and E_n are the core- and outer-shell binding energies respectively. The ejected electron, assuming the excess energy is greater than its binding energy, then has kinetic energy $|E_c - E_n - E'_m|$, where E_m is the binding energy of the Auger electron. The prime denotes that this binding energy is slightly modified as the electron is originating from an already ionized atom [2].

Absorption Spectrum Characteristics

As described above, if the energy of an X-ray beam is swept across an absorption edge (easily achieved at a synchrotron) a sharp rise in absorption is observed. A typical absorption spectrum can be divided into four parts: the pre-edge, rising edge, near-edge and EXAFS (extended X-ray absorption fine structure) regions (illustrated in Figure 2.6). The precise boundaries between these regions are not well-defined in terms of X-ray energy, rather they represent the changing physical processes which occur as the probing X-ray energy passes through an absorption edge. In the pre-edge region, the incoming X-rays do not possess sufficient energy to eject an electron from the shell of interest. However, once the X-ray photons reach the threshold (binding) energy ionization of that shell can occur. After the rising edge, rather than returning to a smoothly decaying function, oscillations are observed which decay in amplitude as the X-ray energy moves further beyond the edge itself. These arise from scattering of the photoelectron, which possesses kinetic energy equal to the difference between the X-ray photon energy and the core-level binding energy, with surrounding atoms. This modifies the photoelectric absorption cross-section of the absorbing atom, and the following details how this behaviour can be used to obtain information about the local atomic structure.

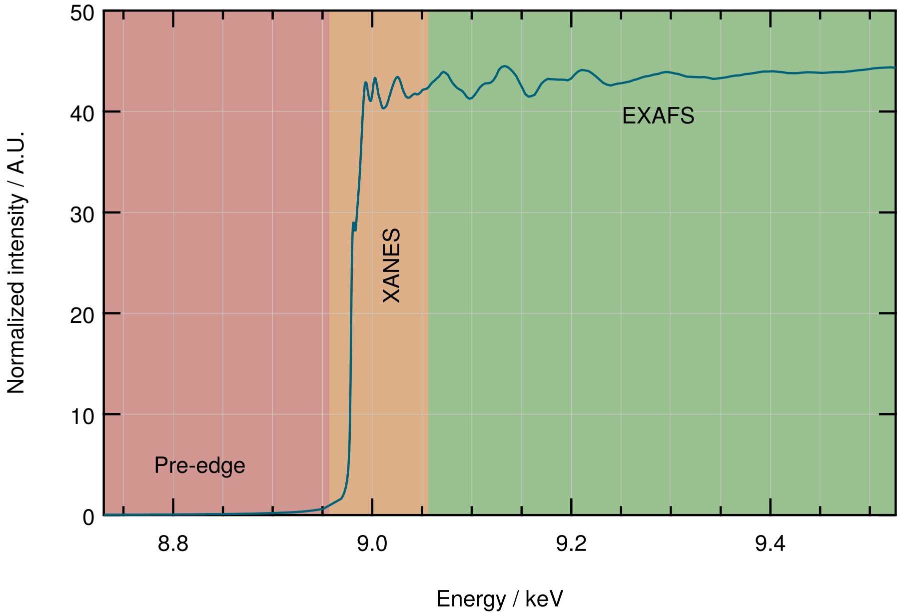

Figure 2.6: *X-ray absorption spectrum of Cu obtained via fluorescence measurement (see Section 2.2.4) indicating the key regions where different physical processes occur.*

2.2.2 Extended X-ray Absorption Fine Structure

Before discussing the near-edge region just beyond the edge, we treat the EXAFS region beginning at 30–50 eV above the rising edge and extending up to several hundred electronvolts. In this energy range the liberated photoelectrons are sufficiently energetic that *single scattering* is dominant i.e. the photoelectron scatters from a single neighbouring atom before returning to the origin. The departing photoelectron can be viewed as a spherically propagating wave with wavevector $k = 2\pi/\lambda$, where λ is the de Broglie wavelength of the electron. The EXAFS oscillations result from the interference between the outgoing wave and the backscattered wave from neighbouring atoms (Figure 2.7).

The general definition for the oscillatory portion of the absorption coefficient $\chi(k)$ is the difference between the observed absorption coefficient $\mu(k)$ and absorption coefficient for an isolated atom $\mu_0(k)$, normalized by the isolated atom contribution, that is

$$\chi(k) = \frac{\mu(k) - \mu_0(k)}{\mu_0(k)} \,. \tag{2.2.1}$$

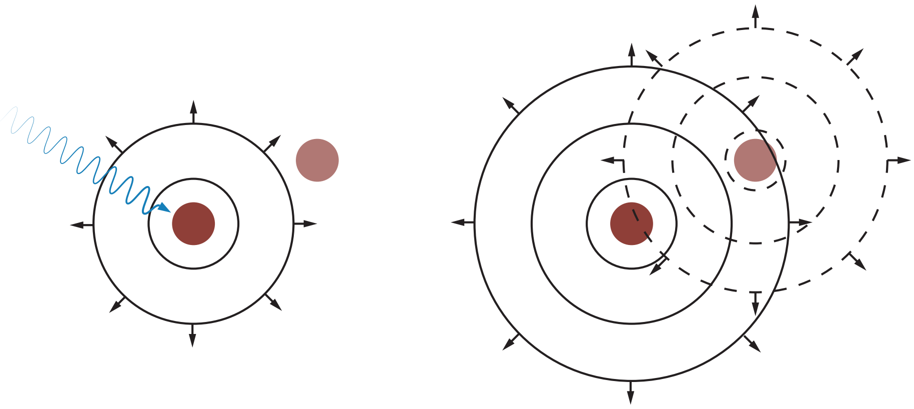

Figure 2.7: *Absorption of an X-ray photon by an atom leads to the promotion of a core-level electron to an unoccupied continuum state. As the photoelectron wave propagates out of the excited atom (solid circles), it can be scattered by neighbouring atoms. Interference between the scattered waves (dashed lines) and the outgoing waves leads to modulation of the X-ray absorption cross-section as a function of X-ray photon energy.*

A heuristic argument can be used to derive a more quantitative, though still relatively simple, description of the post-edge structure in which $\chi(k)$ can be expressed as follows:

$$\chi(k) = \sum_j \frac{N_j}{kR_j^2} |f_j(k,r)| \sin(2kR_j + \delta_j(k,r)) \,, \tag{2.2.2}$$

where N_j is the number of equivalent backscattering atoms j at a distance R from the absorbing atom, $f_j(k,r)$ is the backscattering amplitude which is also a function of the atomic number of the backscattering element j, and $\delta_j(k,r)$ accounts for the phase shifts introduced as the photoelectron traverses the potential of the absorbing atom, the potential of the backscattering atom, and back through the absorbing atom potential. The effects of disorder are approximated by a Debye-Waller factor $e^{-\sigma_j^2 k^2}$, where σ_j is the root-mean-squared deviation of the surrounding atom from their nominal positions. Disorder in real systems is due to the distribution of distances R_j (static) and thermal vibrations (dynamic). Equation 2.2.2 then becomes

$$\chi(k) = \sum_j \frac{N_j}{kR_j^2} |f_j(k,r)| e^{-\sigma_j^2 k^2} \sin(2kR_j + \delta_j(k,r)) \,. \tag{2.2.3}$$

Loss of photoelectrons due to inelastic scattering is accounted for by introducing a term $e^{-2R_j/\lambda_j(k)}$, where $\lambda_j(k)$ is the electron mean free path. So far, the assumption has been made that the scattered photoelectron will find the absorbing atom in its initial state, but due to the lifetime of the core hole there is a certain probability that it will have been filled; this effect is also wrapped up in the mean free path term. An amplitude reduction factor S_0^2 is also introduced to account for shake-up/shake-off processes [10] at the originating atom. This leads to the standard form of the EXAFS equation,

$$\chi(k) = S_0^2 \sum_j \frac{N_j}{kR_j^2} |f_j(k,r)| e^{-2k^2\sigma_j^2} e^{-2R_j/\lambda_j(k)} \sin(2kR_j + \delta_j(k,r)) \, . \qquad (2.2.4)$$

The goal is to determine the radii of the neighbouring shells R_j, and their coordination number N_j, but obtaining values for S_0^2, and σ can also be informative. This is usually achieved by extracting $\chi(E)$ from the raw $\mu(E)$ and converting this to k-space, i.e. $\chi(k)$, using $E = \hbar^2 k^2/2m$. The data, now expressed in terms of frequencies proportional to k, are then Fourier-transformed to give a plot which reveals characteristic lengths[1] associated with interatomic distances R_j. In the full data treatment, the atomic structure of the material under analysis is modelled allowing a theoretical calculation of the EXAFS to be produced. This is fitted to the measured EXAFS spectrum allowing the other parameters of interest to be extracted. Probably the most popular software package for processing and analysis of EXAFS data is the *Horae* suite developed by Bruce Ravel [11]. *Horae* consists of the following:

ATHENA

Graphical processing of EXAFS data, including aligning, de-glitching, merging, background removal, Fourier transforms, and more.

ARTEMIS

Fitting of EXAFS data to theoretical standards calculated using IFEFFIT (a library of EXAFS algorithms) [12] and data modelling allowing extraction of physical parameters based on statistical analysis.

---

[1] The characteristic lengths extracted from the Fourier transform should not be interpreted directly as the R_j as the phase shifts $\delta_j(k,r)$ are not accounted for.

HEPHAESTUS

An advanced periodic table targeted towards X-ray absorption spectroscopists providing lookups and calculators for absorption coefficients, detector gas ratios, absorption lengths and other chemical data.

ATOMS

Generation of input files for FEFF from crystallographic data [13].

Recently, *Horae* has undergone a significant overhaul and the processing capabilities have been pulled out of the main programs to form a new software library, *Demeter*. *Artemis* and *Athena* are now built on the *Demeter* libraries, separating the data processing code from the user interface. This allows users to more easily write their own scripts for batch processing large quantities of XAS spectra, and has enabled the development of a new graphical shell for the *Horae* suite.

2.2.3 X-ray Absorption Near-Edge Structure

Moving back to the region immediately following the absorption edge, photoelectrons in this regime have significantly lower energy than those which have been discussed thus far — only a few eV just after the edge. The mean free path for electrons in this low energy range is comparatively large so they ‘see’ a greater range of absorber-scatterer distances. This results in *multiple scattering* of the electrons i.e. there is a high probability that more than one scattering event will occur before the electron returns to the origin. The increased complexity of the interactions makes *ab initio* calculation a significant challenge so most XANES spectra are interpreted rather than quantitatively analysed, although recent progress in the XANES computation is making quantitative interpretation increasingly feasible [14]. A fundamental difference between photoelectrons in the XANES region and those with higher energy is that they might not be ejected into the continuum, rather they may only gain sufficient energy to be promoted to an unoccupied but *bound* state. The density of such bound states close to the edge can be higher than the density of unbound states which is manifested as a large peak at the edge — for historical reasons, this is known as a *white line*. Absorption peaks may even be observed *before* the X-ray photon energy has reached the ionization threshold which are referred to as *pre-edge transitions*.

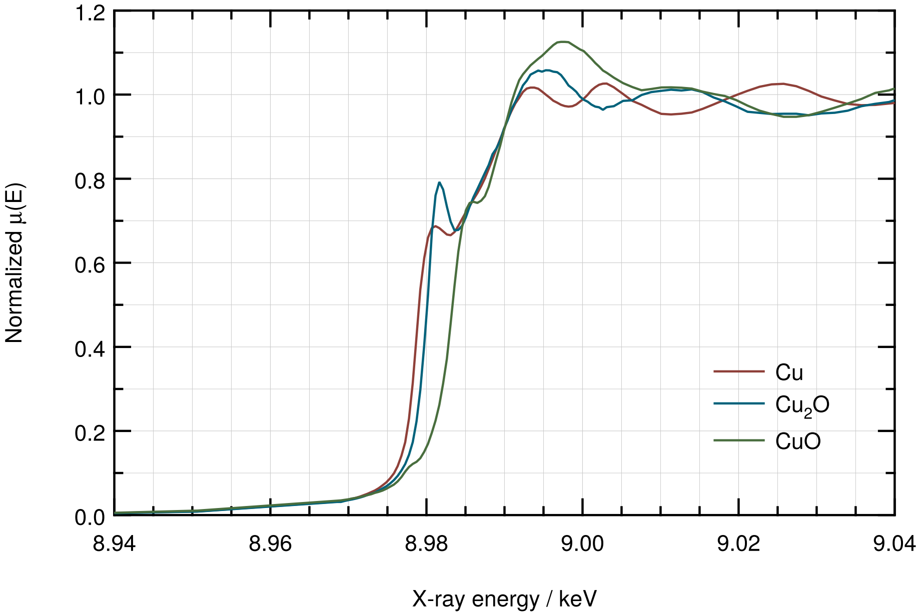

Figure 2.8: *XANES spectra of copper and its oxides*[2]*, cuprite* (Cu_2O) *and tenorite (CuO), demonstrating the positive shift in edge position with increasing oxidation state and the unique nature of the oscillatory structure just past the absorption edge for each compound.*

XANES is very sensitive to the bonding environment of the absorbing atom. The edge position and shape is strongly dependent on formal oxidation state, ligand type and coordination environment so XANES spectra can be used qualitatively as 'fingerprints' for the local bonding environment. For example, in Figure 2.8 it is clear to see that there are distinct differences in the overall shape of the XANES spectra for pure elemental copper and its oxides, in addition to a clear shift in the absorption edge position. This shift is due to the screening of core electrons by valence electrons [15]. In this case, the formation of the bond between the copper and oxygen creates an effective positive (formal) charge on the copper atom (ion). Therefore, the screening is reduced and the core level becomes more tightly bound, increasing the energy required to eject it from its bound state.

In much the same way as for fluorescence transitions, the excitation of the core photoelectron to an unoccupied bound state is controlled by selection rules so for K-shell absorption a p state must be available. For example, transition metal oxides usually have unoccupied 3d states near the Fermi level, but a filled

$2p$ shell. Therefore, transitions to $2p$ level are unavailable unless there is a strong hybridization (mixing) of the unoccupied O $2p$ states with the metal $3d$ levels; XANES spectra are extremely sensitive to such hybridization. Differences in coordination for different oxides result in dramatic alterations in the level of hybridization so pre-edge peaks in the XANES spectra give clear a indication of the local coordination environment of the metal ion.

The polarization state of the X-ray beam can also be utilized to control how the system under investigation is probed. The radiation emitted by bending magnets and wigglers is strongly linear polarized in the plane of the storage ring. Some materials, which are either intrinsically oriented or can be oriented by external forces, exhibit anisotropic absorption of linearly polarized light, a phenomenon known as linear dichroism (LD) [16]. This is particularly useful for probing the molecular orientation of organic materials where sharp core level excitations in carbon, nitrogen, oxygen, and fluorine are often observed. Features in these spectra are typically described in terms of one-electron transitions from core levels to unoccupied π^* and σ^* orbitals. The intensity of these resonances depends on the angle θ between the electric field vector of the X-rays E and the direction of the transition dipole moment μ according to

$$I \propto |E\mu|^2 \propto \cos^2\theta \ . \qquad (2.2.5)$$

For example, in a $1s \rightarrow \pi^*$ transition μ is perpendicular to the plane of the π-bond. As such, the angle dependence of particular spectroscopic features can be used to measure the orientation of specific chemical moieties [17, 18].

Similarly, the properties of circularly polarized X-rays, which may be generated using an undulator such as an APPLE-II type [19], also affects how they are absorbed in certain materials due to the additional selection rules imposed on left- ($\Delta m = -1$) and right-hand ($\Delta m = +1$) polarized light, where m is the magnetic quantum number. This is most commonly used to investigate the magnetic properties of materials via X-ray magnetic circular dichroism (XMCD) [2]. Differences in the absorption spectra obtained using opposite light of opposite helicity can be used to determine the residual magnetic moments via the XMCD sum rules [20].

---

[2] Data from 2007 04 DUBBLE EX01 — *'r36536.dat'*, *'r36541.dat'* & *'r36542.dat'*

Finally, while the dipole approximation for X-ray absorption is generally good, higher order-transitions, e.g. electric quadrupole ($\Delta l = \pm 2; 0$), are not always negligible. They can be readily observed in some situations, such as in the pre-edge region of transition metal complexes [21]. Also, the quadrupole/dipole ratio grows quadratically with Z, so it can also be expected to be substantial for heavier elements [3].

2.2.4 Detection Modes

X-ray absorption spectra are most commonly measured via detection of X-rays, either the transmitted primary beam or fluorescent secondary X-rays. In the former case a typical setup would consist of gas ionization chamber detectors placed before and after the sample. These measure the intensity of the incoming I_0 and transmitted I_t beams respectively. The thickness of the sample must be accounted for so absorption is calculated using $\mu \propto \ln(I_t/I_0)$. In fluorescence geometry, the second detector measuring I_f is ideally placed at 90° w.r.t. the sample surface to minimize detection of backscattered X-rays. This also serves to increase the fraction of detected X-rays which originated from near the surface, reducing self-absorption effects which dampen the EXAFS and XANES modulation. An energy-dispersive detector is often used to isolate the signal from a single fluorescence line, say K_α. As fluorescence is simply proportional to absorption, the relationship $\mu \propto I_t/I_0$ is used.

Alternative detection routes are available via the measurement of other secondary emission products. Non-radiative decay processes which occur following each absorption event produce an abundance of electrons — primarily photoelectrons and Auger electrons. As with X-ray fluorescence, total electron yield (TEY) is proportional to X-ray absorption. TEY is particularly useful for measurement of low Z elements using soft X-rays, requiring that the sample be held under ultra-high vacuum, due to the increased probability of Auger emission. The emitted electrons are collected by electrodes within the vacuum chamber, or very close to the sample if measurements are carried out in air. Energy discrimination of the electrons allows the photoelectrons or electrons generated by specific Auger processes to be isolated. An important feature of this detection method is its extreme surface sensitivity making it particularly useful for the study of thin films and surface adsorbate structures. Thus, it is usually referred to as surface extended X-ray absorption fine structure (SEXAFS) [22].

The photon emission resulting from X-ray absorption is not only limited to X-rays resulting from core level electron transitions. Subsequent processes lead to radiative transitions between energy levels in the ultra-violet, visible and infra-red regimes. Photon-in, photon-out processes are usually termed photoluminescence, but since X-ray photons are the primary excitation source here it is normal to the phenomenon as X-ray excited optical luminescence (XEOL). As the title of this thesis suggests, XEOL is key to the work presented here, and will be discussed in more detail shortly. As described in the next section, XEOL emission has some useful characteristics and, importantly, allows for detection modes which are simply not possible using other XAS variants.

2.3 X-ray Excited Optical Luminescence

The X-ray stimulated emission of trans-visible photons results from complex electron cascade processes initiated by core-hole decay. The specific nature of these processes is highly dependent on the material properties: composition, structure, morphology, size, crystallinity, and defects. Owing to the multiple parameters controlling these numerous processes, a detailed theory of XEOL has not yet been established. In the following section, an overview of the primary physical processes which occur as part of a XEOL emission event is given.

2.3.1 XEOL Processes

The general process may be split into three subsequent, essentially independent steps [23]:

1. X-ray absorption and conversion of the primary excitation into thermalized secondary electronic excitations (e.g. electron hole pairs).
2. Energy transfer via these secondary electronic excitations toward the luminescent centres promoted into excited states.
3. De-excitations of the luminescence centres with emission of optical photons.

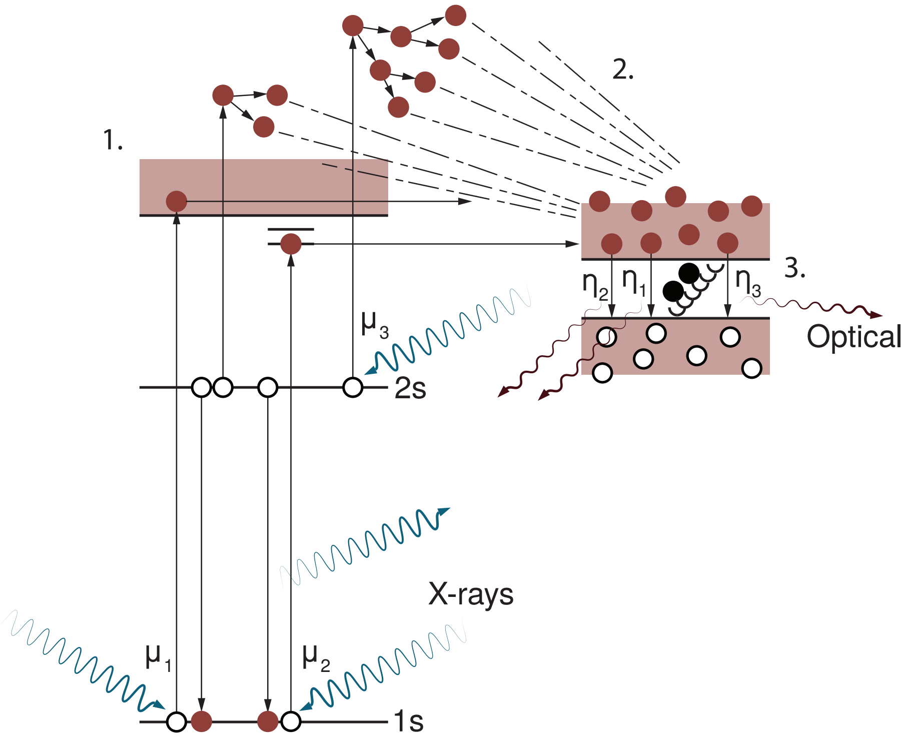

Figure 2.9: *Schematic energy level diagram of excitation-luminescence processes. Illustrated here are an excitation from a 1s state (absorption coefficient μ_1) to a continuum state, a 1s (μ_2) to a bound state, and a 2s μ_3 to a continuum state. These give rise to a single luminescence with the respective yields η_1, η_2, and η_3. Additionally, the events of an X-ray fluorescence, a KLL Auger process, electron multiple scattering, a non-radiative decay due to electron-phonon scattering, and radiative transitions are shown.*

These steps are illustrated in the schematic energy level diagram given in Figure 2.9. As such, the XEOL quantum yield η_{XEOL} can be written as the product of three factors

$$\eta_{XEOL} = N_{ee} S Q \,, \tag{2.3.1}$$

where N_{ee} is the number of secondary excitations (this characterises the efficiency of the conversion process), S is the efficiency of the transfer process, and Q denotes the quantum efficiency of the luminescent centres. The total number of secondary excitations is dependent on the absorbed X-ray energy E and is given by

$$N_{ee} = \frac{E}{E_{ee}} \,, \tag{2.3.2}$$

where E_{ee} is the average energy required to create a single secondary excitation. Each of the three steps is now examined in more detail.

Secondary Electronic Excitations

Secondary electronic excitations in a crystal can be of many types: electron-hole pairs i.e. one electron in the conduction band and one hole in the valence bond or core band, excitons produced by Coloumb interactions between electrons and holes, and even more complicated excitations like biexcitons, or excitations related to lattice or radiation-induced defects [24].

It is important to note that there is a spatial range associated with the de-excitation step. An effective mean radius R_{ee} can be calculated from

$$R_{ee} \approx l_{ee}\sqrt{N_{ee}} \,, \tag{2.3.3}$$

where l_{ee} is the electron-electron scattering mean free path. It is important to note that this is dependent on the absorbed X-ray energy from Equation 2.3.2. Take, for example, an ionic crystal with a band gap energy $E_g \approx$ 5eV: excitation by soft X-ray photons ($E \approx 1000\,\text{eV}$; $l_{ee} \approx 10\,\text{Å}$) would give $N_{ee} \approx 100$ and $R_{ee} \approx 100\,\text{Å}$. In contrast, excitation by harder X-rays ($E \approx 10\,\text{keV}$; $l_{ee} \leq 50\,\text{Å}$) yields $N_{ee} \approx 1000$ and $R_{ee} \approx 1500\,\text{Å}$. These results are verified by Monte Carlo simulations which have been performed to estimate R_{ee} in various samples [25, 26].

There is also a time scale for the de-excitation step; electron-electron relaxation occurs within 10^{-14}–10^{-12} s [27], while thermalization via electron-phonon interactions takes 10^{-12}–10^{-10} s [28]. There is a possibility of monitoring XEOL emission to gain site-specific information either via very fast time-resolved measurements using short X-ray pulses [29–31], or by examination of specific emission bands in the luminescence spectrum [32–34]. However, it should be noted that this can only be done under the condition that the sites which one would like to discriminate are not separated by a shorter distance than R_{ee}.

Energy Transfer

Following relaxation of the numerous electronic excitations their energy is transferred to luminescence centres, the efficiency of which is accounted for by the parameter S in Equation 2.3.1. The specific nature of the electrons and holes created in the previous step affects the distance over which energy can be transferred. Secondary electrons or holes may maintain their mobility, but they can also become trapped, either separately or in pairs. They can also migrate towards the surface where they may re-combine radiatively, or non-radiatively at surface defects.

In photoconductivity, the charge carriers become trapped by an *activator*, a luminescence centre with significant excess charge with respect to the lattice. For example, in Y_2O_2S:Tb (a scintillator material) the emission of optical photons occurs via the following sequence

$$\mathrm{Tb}^{3+} + h^+ + e^- \rightarrow \mathrm{Tb}^{4+} + e^- \rightarrow \mathrm{Tb}^{3+,*} \rightarrow \mathrm{Tb}^{3+} + \hbar\nu \qquad (2.3.4)$$

where $h^+ + e^-$ are a hole in the valence band and an electron in the conduction band [35].

Semiconductors are also good candidates for such mechanisms. In this case it is expected that the luminescent photon energy will be close to that of the band gap with short (nanosecond) lifetimes, but defect states can result in emission at energies significantly less than the band gap energy with longer lifetime (hundreds of nanoseconds to microseconds) [29].In this sense, XEOL provides an attractive alternative to photoluminescence (PL) as a means for investigating luminescent centres in that it does not depend on resonant absorption, and can excite states not accessible by UV or visible excitation [36].

If there is an overlap between the optical absorption spectrum of the absorption sites in the crystal and the emission spectrum of luminescent centres then there is radiative transfer of energy from the latter to the former. This re-absorption of XEOL luminescence distorts the observed XEOL excitation spectrum; this effect has been observed in measurements of powdered $EuCl_2$ [37] and GeO_2 (Tb) nanowires [38]. However, no systematic investigation into the angular dependence of XEOL emission has yet been reported.

A further interesting example of re-absorption is in alkali halide crystals, where the radiative re-combination of electron-hole pairs may result in the formation of lattice defects, so-called *F-centres* (or colour centres) [39]; these are strongly absorbing in the visible range. The efficiency of formation of such defects was shown to depend on the absorption coefficient of the sample [40]. Whenever the emission spectrum of the luminescence centres overlaps with the absorption spectrum of the colour centres the XEOL emission spectrum is distorted by the energy dependence of the formation of the defects. In the case where the lifetime of the radiation defects is long, the efficiency of the XEOL will also depend on the irradiation time.

An additional energy transfer mechanism is via excitons, coupled electron-hole pairs, which can migrate through the lattice. Depending on the strength of the coupling, a distinction is made between two different types of exciton: *Wannier* or *Mott* (weakly-coupled) where the wavefunction is spread over many lattice sites, and *Frenkel* (strongly-coupled) where the wavefunction is tightly localised on a single lattice site [41]. It has been shown that in molecular crystals the diffusion length of a large radius exciton can be up to 100 μm, whereas a small radius exction may only migrate over 50 nm [42]. Excitons may recombine during their lifetime yielding optical emission, or they may be capture by the local Coulomb potential of an activator resulting in direct excitation of the luminescent centre.

Luminescence Quantum Yield

The quantum efficiency, Q in Equation 2.3.1, of luminescence can often be measured independently, e.g. by visible, UV, or VUV excitation. Two subclasses of luminescence centre exist:

Activators

Dopants deliberately introduced in a host lattice, e.g. rare earths or transition metals, at very low concentrations. The luminescence in such centres is due to radiative transition between well-defined levels in the impurity ion. The theory for calculating the quantum efficiency Q for these centres is well-established [43] and predictions can be made with good accuracy.

Intrinsic

Such luminescence centres are associated with the lattice itself, e.g. excitons [44] or cross-luminescence [45], or with consituents such as molecular ions.

The luminescence yield is usually proportional to the excitation density. However, there are situations where the yield is non-linear such as in the luminescence of biexcitons often observed in semiconductors [46].

2.3.2 XEOL-XAS

The first reported observation of an X-ray absorption spectrum detected via optical luminescence was by Bianconi et al. [47]. The UV emission from a single crystal of CaF_2 was measured under X-irradiation over a 300 eV range about the Ca K-edge. The resulting spectrum clearly showed the absorption edge step with post-edge oscillations. Moreover, they also immediately demonstrated a phenomenon unique to XEOL-XAS spectra: an inverted edge. This occurs when the total photoluminescence yield actually drops at the absorption edge and the post-edge features appear as a ‘mirror’ image of the absorption spectrum i.e. maxima in absorption appear as minima in the XEOL structure, and vice-versa. The optical emission from CaF_2 is attributed to the recombination of self-trapped excitons (STEs) so the emission intensity increases with the integrated energy of excited photoelectrons and Auger electrons generated by X-ray absorption by higher shells. It is important to note that the thickness of the crystal under bombardment was sufficient for total absorption of the incoming photons. Therefore, it was argued that the reduction in yield at the K-edge can be explained by the onset of radiative recombination (X-ray fluorescence) of the $1s$ hole reducing the integrated electron energy. In addition, by plotting the inverse of the oscillatory portion of the XEOL spectrum with the corresponding region in the transmission absorption spectrum the potential for EXAFS data to be acquired in this manner was also recognized. Investigations by Goulon et al. [32, 48] found that a thin powder sample of the same material exhibited a positive edge with EXAFS oscillations comparable to a conventional X-ray absorption spectrum, and discussed a criterion for the appearance of positive and negative steps.

Emura et al. [49] expanded on these findings to develop a phenomenological model for predicting the sign of the edge step in XEOL spectra. If $\mu(E)$ and $\mu'(E)$ are the absorption coefficients for the L- and K-shell excitations, and

$\eta(E)$ and $\eta'(E)$ are the corresponding optical yields, then the ratio R of the total measured intensity to the intensity below the absorption edge is given by

$$R = \frac{1-\exp[-(\mu+\mu')t]}{1-\exp(-\mu t)}\frac{\mu+\mu' B}{\mu+\mu'} , \tag{2.3.5}$$

where $B \equiv \eta'/\eta > 0$ and t is the sample thickness. It is then informative to examine the limiting values of R as a function of the parameters t and B such as

$$R_{t\to\infty} = \frac{\mu+\mu' B}{\mu+\mu'} , \tag{2.3.6}$$

$$R_{t\to 0} = 1 + \frac{\mu'}{\mu}B > 1 , \tag{2.3.7}$$

and

$$R_{B\to 0} = \frac{1-\exp[-(\mu+\mu')t]}{1-\exp(-\mu t)}\frac{\mu}{\mu+\mu'} . \tag{2.3.8}$$

If $B > 1$, the edge step will always be positive, regardless of the sample thickness. For a sufficiently thick sample, Equation 2.3.6 reveals that the edge will be negative if $B < 1$, whereas if $B > 1$ a normal spectrum will be observed. However, a very thin sample will exhibit a positive edge as demonstrated in Figure 2.10. In Equation 2.3.8, $B \to 0 \implies \eta' \to 0$ means that there is no contribution to the optical emission from the K-shell excitation so the spectrum will be negative for arbitrary sample thickness. In the intermediate cases, the sign of the edge is determined by the interplay between the factor $1-\exp[-(\mu+\mu')t]/1-\exp(-\mu t)$ which contributes to the positive edge, and the factor $\mu+\mu' B/\mu+\mu'$ which can lead to a negative edge under the condition $B < 1$. Where additional components (other absorbing atoms) in the system contribute further sources of luminescence yield the behaviour is the same except when the extra contribution is much greater than both $\mu(E)$ and $\mu'(E)$. In this case, the value of R is be very close to 1 and edge step is all but non-existent.

Whereas the X-ray fluorescence yield can reliably be used to extract $\chi(k)$, the preceding arguments indicate that the same cannot always be said for the optical emission. Even when an edge step (positive or negative) is observed, the pre-edge background is usually a significant fraction of the post-edge signal —

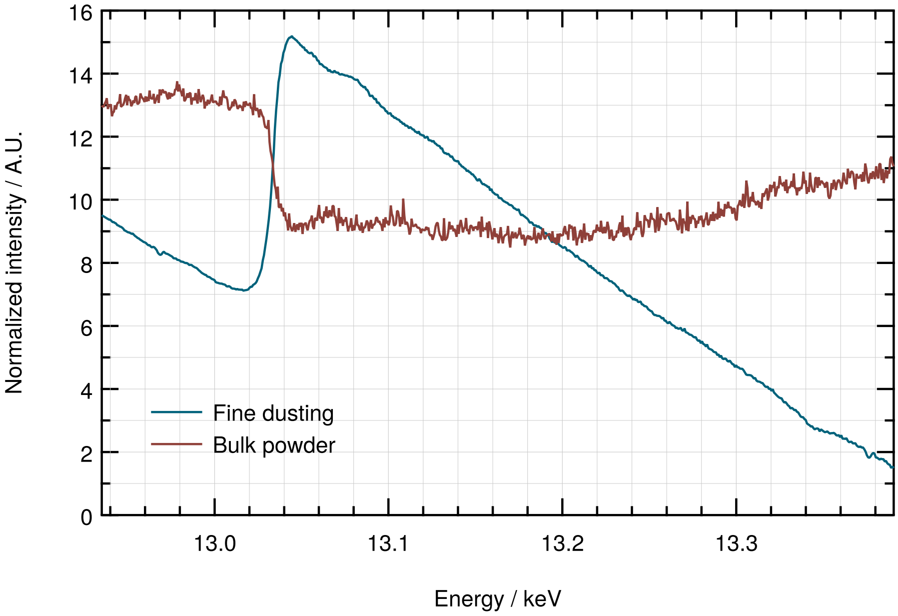

Figure 2.10: *XEOL spectra of PbCl powder acquired at the Pb L_3 edge using ODXAS1*[3]*. Measurement of the bulk powder clearly shows inversion of the absorption edge, whereas a light dusting of the powder on an acetal disc gives a normal edge. Despite the noise in the former spectrum, mirroring of the post-edge structure is observed.*

edge heights of only 1.5–3× are typical c.f. several orders of magnitude for fluorescence measurements. Caution must also taken when attempting to extract structural parameters from XEOL-EXAFS data as expressed by Soderholm et al. [50]. EXAFS spectra were acquired for $4f$ rare-earth ions in a variety of host materials. A one-to-one correspondence was found for XEOL and transmission scans of Eu_2O_3 over the Eu L_3 edge. In contrast, a comparison of spectra from $TbCl_3 \cdot 6\,H_2O$ acquired over the Tb L_3 edge showed significant anomalies. The XEOL data were significantly weighted towards higher values of k (not seen in the transmission data), and the phase showed complicated behaviour as a function of k — the XEOL and transmission data were in phase at low k, but high-k oscillations above $10\,\text{Å}^{-1}$ were 180° out of phase. This is a further indication of the energy dependence of some decay pathways discussed in the previous section.

---

[3] Data from 2009 12 DUBBLE — *'r70624.dat'* & *'r70645.dat'*

2.3.3 Imaging with XEOL

There are two methods by which an image of the sample can be formed using XEOL. The first approach is identical to the primary method for imaging using X-ray fluorescence — by using the X-ray beam as a scanning probe. The sample is moved underneath the X-ray beam footprint in a raster fashion. By dwelling on each point to acquire a total XEOL signal before moving onto the next point, pixel-by-pixel an image can be produced. Repeating this process while incrementing the X-ray energy for each image allows spatially-resolved XAFS spectra to be acquired. Alternatively, the XEOL emission from each pixel can be wavelength-resolved in order to map the intensity of specific emission lines [51, 52]. Performing both of these measurements in parallel will give an extremely comprehensive (if rather large) data set. The lateral resolution of images produced in this manner is set by the dimensions of the X-ray beam footprint; this is commonly on the order of microns, but nano-resolution maps of semiconductor structures have also been reported [53, 54].

Extreme lateral resolution can be achieved through the use of a scanning near-field optical microscope for XEOL detection (XAS-SNOM) [55, 56]. Here, the scanning probe is the microscope itself — the probe tip is moved across the surface which is illuminated by a micron-scale X-ray beam. The probe remains at a distance much less than the optical wavelength from the surface so it is the evanescent waves — such waves only exist very close to the surface and do not propagate into the far-field — which are measured allowing the optical resolution limit to be beaten; lateral resolution of 100–200 nm has been reported [56]. An additional benefit of this method is that the feedback mechanism controlling the scanning tip also produces a topographical map of the surface, allowing the physical size of surface features to be measured with vertical resolution of a few nanometres. In order to produce reasonable X-ray absorption spectra using this method a very high X-ray flux is required in order that the tiny probe tip collects sufficient optical photons.

The alternative to a scanning probe approach is to use full-field optics to directly image a large area of the sample surface. At the inception of this project the only previous instrumentation to be constructed for this type of measurement using a synchrotron X-rays as an excitation source was CLASSIX1 (Chemistry, Luminescence And Structure of Surfaces by micro-Imaging X-ray absorption) by Poolton et al. [57]. CLASSIX1 was developed at SRS, Daresbury as a progression from MoLES (mobile luminescence end station) [58–60] and consisted of a UHV-compatible sample chamber containing a cryostat cold-finger for low temperature measurements. Microscopy was performed using a set of interchangeable (for different magnifications), long-working distance optics focused on the sample through a window in the vacuum chamber. Its ability to couple to different beamlines enabled the potential for measurements to be carried out in both the UV/soft X-ray and hard X-ray regimes. Of course, with the SRS not longer operational, neither is CLASSIX1. Nevertheless, it was able to demonstrate the power of XEOL imaging for structural mapping using XEOL-XANES of boron nitride (BN), a wide band gap semiconductor found in a number of phases, commonly with cubic and hexagonal structures. XEOL images of BN micro-crystals pressed into an aluminium substrate were acquired. Through analysis of the XANES spectra, a characteristic dip caused by a distinct π^*-resonance in the sp^2-bonded hexagonal phase was identified. Therefore, by comparing images on and off the resonance a phase distribution map could be obtained, showing that the resonance was isolated to individual crystallites. Very recently, Rosenberg et al. [61] have explored the use of full-field XEOL imaging for spatially-resolved XMCD measurements of NiFe using commercially available optical components.

2.4 Previous work — ODXAS1

ODXAS1 was a precursor instrument built by the group to establish proof-of-principle of a portable XEOL detection system [62]. XEOM1 has taken several design cues from ODXAS1, particularly with regard to its mechanical design and construction. ODXAS1 was designed simply to transport as many XEOL-emitted photons as possible to the detector, a Hamamatsu H8259-01 photomultiplier (PM) tube (Hamamatsu Photonics K.K., Japan). Consequently, a simple two-lens optical system was used; the objective serves to capture a reasonable flux of visible photons from the sample, and the condenser lens projects the collected light onto the PM tube sensor. Within this simple concept also lies the primary limitation of ODXAS1; the light collection system provides no lateral resolution, so any the only way to produce a spatial map is to use the X-ray beam as a scanning probe as described above. In addition, the control system has become rather fragmented over the course of its development and several components are now obsolete, particularly those related to the computer interface (see Section 3.2.4). As such, there is a danger that failure of these components will cripple the system due the lack of availability of replacement parts.

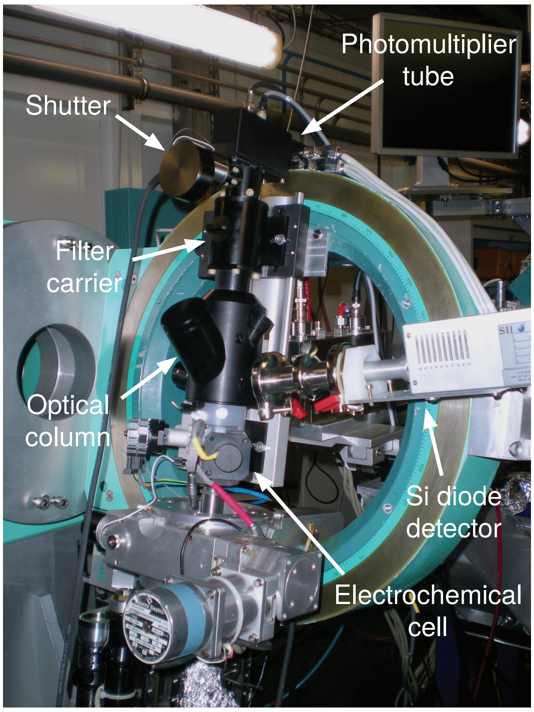

Figure 2.11: *Deployment of ODXAS1 on beamline BM28 XMaS at the ESRF. Here measurements are being carried out in conjunction with the eCell, and fluorescence data is collected using a Vortex® Si drift diode detector. During data acquisition, the entire assembly is covered with a thick black sheet in order to minimize the background signal from stray ambient light.*

Many ODXAS1 experiments were carried out in conjunction with electrochemical measurements using a novel electrochemical cell (eCell), the setup for which is shown in Figure 2.11; details of the latest eCell have not yet been published, but description of an earlier iteration can be found in [63]. The body of the eCell constructed from PCTFE (a thermoplastic polymer), its high chemical resistance making it ideally suited for carrying out experiments requiring containment of a corrosive environment. The disadvantage of using the cell for XEOL measurements is that the translucent PCTFE allows light to easily enter the optical system. Several strategies have been employed to keep stray light out of the optics. Experiments are carried out with the experimental hutch in complete darkness (or as close as possible). All external windows are covered with aluminium foil, as are any other sources of light within the hutch. Additionally, the whole experiment was shrouded in a blackout sheet. While being moderately effective, using blackout curtain was not particularly practical as it often required many adjustments to make it completely light-tight, a time-consuming process which ate into the time for carrying out experiments. When using ODXAS1, samples were always mounted in the cell, either in the usual working electrode configuration or by some alternative means — for example, powders were packed into plastic caps and held in with Ultralene, and irregularly-shaped flat samples were simply affixed to the top of a dummy working electrode.

2.5 Summary

This chapter has covered the background information relevant to the areas explored during this project. The phenomenon of synchrotron radiation has been introduced and the key features of a modern synchrotron radiation facility have been described. Next, a summary of the basic theory describing the X-ray absorption process has been given, followed by a more detailed exploration of the specific processes which result in the generation of XEOL emission. Some different techniques for measuring XEOL have been described and the key information gained from each has been highlighted. Finally, the previously developed XEOL instrument ODXAS1 has been described along its limitations which have motivated the development of XEOM1.

References

[1] P Wilmott. *An Introduction to Synchrotron Radiation: Techniques and Applications*. Wiley, 2011.

[2] J Als-Nielsen and D McMorrow. *Elements of Modern X-ray Physics*. Wiley, Chichester, 2nd ed. edition, 2011.

[3] G Bunker. *Introduction to XAFS: A Practical Guide to X-ray Absorption Fine Structure Spectroscopy*. CUP, 2010.

[4] D H Tomboulian and P L Hartman. Spectral and angular distribution of ultraviolet radiation from the 300-MeV Cornell synchrotron. *Phys. Rev.*, 102(6):1423–1447, 1956.

[5] L Robinson. Experiments Begin at Daresbury's SRS. *Science*, 213(4510): 852–856, 1981.

[6] P Schmüser, M Dohlus, and J Rossbach. *Ultraviolet and Soft X-Ray Free-Electron Lasers: Introduction to Physical Principles, Experimental Results, Technological Challenges*. Springer, 2008.

[7] C Christou and J A Dobbing. The First Eighteen Months of Top-up at Diamond Light Source. In *Proc. IPAC'10*, pages 2636–2638, 2010.

[8] G Brown, et al. Wiggler and Undulator Magnets - A Review. *Nucl. Instrum. Methods*, 208:65–77, 1983.

[9] J J Hester. The Crab Nebula: An Astrophysical Chimera. *Annu. Rev. Astron. Astrophys.*, 46(1):127–155, September 2008.

[10] P Persson, et al. Shake-up and shake-off excitations with associated electron losses in X-ray studies of proteins. *Protein Sci.*, 10:2480–2484, 2001.

[11] B Ravel and M Newville. ATHENA, ARTEMIS, HEPHAESTUS: data analysis for X-ray absorption spectroscopy using IFEFFIT. *J. Synchrotron Radiat.*, 12 (Pt 4):537–41, July 2005.

[12] M Newville. IFEFFIT: interactive XAFS analysis and FEFF fitting. *J. Synchrotron Radiat.*, pages 322–324, 2001.

[13] B Ravel. ATOMS : crystallography for the X-ray absorption spectroscopist. *J. Synchrotron Radiat.*, 8(2):314–316, March 2001.

[14] J J Rehr, et al. Parameter-free calculations of X-ray spectra with FEFF9. *Phys. Chem. Chem. Phys.*, 12(21):5503–13, June 2010.

[15] Jun Kawai. Absorption Techniques in X-Ray Spectrometry. In R A Meyers, editor, *Encycl. Anal. Chem.*, pages 13288–13315. Wiley, Chichester, 2000.

[16] A Rodger and B Norden. *Circular Dichroism and Linear Cichroism*. OUP, New York, 1997.

[17] J Stöhr and D A Outka. Determination of molecular orientations on surfaces from the angular dependence of near-edge x-ray-absorption fine-structure spectra. *Phys. Rev. B*, 36:7891, 1987.

[18] Juxia Fu and Stephen G Urquhart. Linear dichroism in the X-ray absorption spectra of linear n-alkanes. *J. Phys. Chem. A*, 109(51):11724–32, Decem-

ber 2005.

[19] Shigemi Sasaki. Analyses for a planar variably-polarizing undulator. *Nucl. Instruments Methods Phys. Res. A*, 347(1-3):83–86, August 1994.

[20] C T Chen, et al. Experimental Confirmation of the X-Ray Magnetic Circular Dichroism Sum Rules for Iron and Cobalt. *Phys. Rev. Lett.*, 75:152, 1995.

[21] J E Hahn, R A Scott, and K O Hodgson. Observation of an electric quadrupole transition in the X-ray absorption spectrum of a Cu (II) complex. *Chem. Phys. Lett.*, 88(6):595–598, 1982.

[22] D C Koningsberger and R Prins. *X-ray absorption : principles, applications, techniques of EXAFS, SEXAFS, and XANES*. Wiley, New York, 1988.

[23] D J Robbins. On Predicting the Maximum Efficiency of Phosphor Systems Excited by Ionizing Radiation. *J. Electrochem. Soc.*, 127(12):2694–2702, 1980.

[24] A Rogalev and J Goulon. X-ray Excited Optical Luminescence Spectroscopies. In *Chemical Applications of Synchrotron Radiation Part II: X-ray Applications*, chapter 15, pages 707–760. World Scientific, Singapore, 2002.

[25] D A Hill. *X-ray Excited Optical Luminescence (XEOL) and Its Application to Porous Silicon*. Ph.d., University of Warwick, 1998.

[26] A Kikas and M Elango. Monte Carlo Simulation of the Production of Charge Carriers in NaCl Crystals by XUV Irradiation. *Phys. Status Solidi B*, 130(1): 211–218, 1985.

[27] M Costato, S Fontanesi, and L Reggiani. Electron energy relaxation time in Si and Ge. *J. Phys. Chem. Solids*, 34(3):547–564, 1973.

[28] G D Mahan. Relaxation time of electron-phonon systems. *J. Phys. Chem. Solids*, 31(7):1477–1484, 1970.

[29] T-K Sham and R A Rosenberg. Time-resolved synchrotron radiation excited optical luminescence: light-emission properties of silicon-based nanostructures. *ChemPhysChem*, 8(18):2557–67, 2007.

[30] T Z Regier, et al. Advances in Time Resolved X-ray Excited Optical Luminescence Instrumentation at the Canadian Light Source. In *AIP Conf. Proc.*, volume 1234, pages 838–841, 2010.

[31] R P Taylor, et al. The development of a XEOL and TR XEOL detection system for the I18 microfocus beamline Diamond light source. *J. Lumin.*, 134:49–58, February 2013.

[32] J Goulon, et al. On a site-selective exafs experiment using optical emission. *J. Chem. Phys.*, 78:347–356, 1983.

[33] R F Pettifer and A J Bourdillon. Site-selective EXAFS via optical de-excitation. *J. Phys. C*, 20:329–335, October 1987.

[34] S J Naftel, et al. Soft x-ray excited optical luminescence from poly(N-vinylcarbazole). *J. Appl. Phys.*, 93(9):5191, 2003.

[35] A M Gurvich. *Introduction to Physical Chemistry of Luminescent Crystals*. Vysch. Shloka, Moscow, 1982.

[36] P-S G Kim, et al. X-ray-excited optical luminescence (XEOL) and X-ray absorption fine structures (XAFS) studies of gold(I) complexes with diphosphine and bipyridine ligands. *Inorg. Chem.*, 46(3):949–57, 2007.

[37] C Gauthier, H Emerich, and J Goulon. Distortion of XAFS Spectra Recorded with X-ray Excited Optical Luminescence. *Jpn. J. Appl. Phys.*, 32:226–228, 1993.

[38] F Heigl, et al. XANES and photoluminescence studies of crystalline GeO2 (Tb) nanowires. *J. Phys. Conf. Ser.*, 190:1–6, 2009.

[39] Noriaki Itoh and Katsumi Tanimura. Formation of interstitial-vacancy pairs by electronic excitation in pure ionic crystals. *J. Phys. Chem. Solids*, 51(7): 717–735, 1990.

[40] Mihiro Yanagihara, Shoichi Hirota, and Yasuhiro Kondo. F-center formation by Br K-hole Auger decay in KBr. *Phys. Rev. B*, 53:13386, 1996.

[41] R S Knox. *Theory of Excitons*. Academic Press Inc., 1963.

[42] V M Agranovich and M D Galanin. *Electronic Excitation Energy Transfer in Condensed Matter*. North-Holland Publishing Company, 1982.

[43] B Henderson and G F Imbusch. *Optical Spectroscopy of Inorganic Solids*. Clarendon Press, 1989.

[44] K S Song. *Self-Trapped Excitons*. Springer, second edition, 1996.

[45] G Blasse and B C Grabmaier. *Luminescent Materials*. Springer-Verlag, 1994.

[46] C Klingshirn. Optical properties of highly excited direct gap semiconductors. *Phys. Rep.*, 70(5):315–398, 1981.

[47] A Bianconi, D Jackson, and K Monahan. Intrinsic luminescence excitation spectrum and extended X-ray absorption fine structure above the K edge in CaF2. *Phys. Rev. B*, 17(4):2021, 1978.

[48] J Goulon, et al. On experimental attenuation factors of the amplitude of

the EXAFS oscillations in absorption, reflectivity and luminescence measurements. *J. Phys. (Paris)*, 43(3):539, 1982.

[49] S Emura, T Moriga, and J Takizawa. Optical-luminescence yield spectra produced by x-ray excitation. *Phys. Rev. B*, 47(12):6918–6930, 1993.

[50] L Soderholm, et al. X-ray excited optical luminescence (XEOL) detection of x-ray absorption fine structure (XAFS). *J. Chem. Phys.*, 109(16):6745–6752, 1998.

[51] G Martínez-Criado, et al. Scanning X-ray excited optical luminescence microscopy in GaN. *Appl. Phys. Lett.*, 89(22):221913, 2006.

[52] O Vyvenko, et al. Scanning X-ray excited optical luminescence microscopy of multi-crystalline silicon. *Phys. Status Solidi A*, 207(8):1940–1943, August 2010.

[53] G Martínez-Criado, et al. Spatially resolved X-ray excited optical luminescence. *Nucl. Instrum. Meth. B*, 284:36–39, August 2012.

[54] G Martínez-Criado, et al. X-ray excited optical luminescence imaging of InGaN nano-LEDs. *Phys. Status Solidi C*, 9(3-4):628–630, March 2012.

[55] D Pailharey, et al. Nanoscale x-ray absorption spectroscopy using XEOL-SNOM detection mode. *J. Phys. Conf. Ser.*, 93:1–5, December 2007.

[56] S Larcheri, et al. X-ray excited optical luminescence detection by scanning near-field optical microscope: a new tool for nanoscience. *Rev. Sci. Instrum.*, 79(1):013702, January 2008.

[57] N Poolton, et al. New instrumentation for micro-imaging X-ray absorption spectroscopy using optical detection methods. *Nucl. Instrum. Methods*, 246 (2):445–451, May 2006.

[58] F Quinn, et al. The Mobile Luminescence End-Station, MoLES: a new public facility at Daresbury Synchrotron. *J. Synchrotron Radiat.*, 10(6):461–466, October 2003.

[59] N R J Poolton, et al. High-sensitivity instrumentation for spectrally-resolved optically detected X-ray absorption spectroscopy. *Nucl. Instrum. Meth. B*, 225(4):590–598, 2004.

[60] N R J Poolton, B Hamilton, and D a Evans. Synchrotron-laser pump-probe luminescence spectroscopy: correlation of electronic defect states with x-ray absorption in wide-gap solids. *J. Phys. D*, 38(9):1478–1484, May 2005.

[61] R A Rosenberg, et al. Elemental and magnetic sensitive imaging using x-

ray excited luminescence microscopy. *Rev. Sci. Instrum.*, 83(7):073701, July 2012.

[62] A Adriaens, et al. Real time observation of X-ray induced surface modification using simultaneous XANES and XEOL-XANES. *Anal. Chem.*, 85(20): 9556–9563, 2013.

[63] A Adriaens, et al. Insights into electrolytic stabilization with weak polarization as treatment for archaeological copper objects. *Anal. Bioanal. Chem.*, 387(3):861–8, 2007.

Chapter 3

XEOM Design & Construction

In this section, XEOM1 will be considered in its current state of development. Some features discussed here were not part of the initial design and building phase of XEOM1; rather, they were introduced or modified based on discoveries made during testing done both in the laboratory and at synchrotron beamlines. Where applicable, such features are explicitly pointed out and further details about relevant experiments can be found in Chapter 4.

3.1 Optics

As mentioned in Section 2.4, information learned from the design and use of ODXAS1 heavily influenced the approach taken to the design of XEOM1. While the relative crudeness of the optics could be afforded in a simple photon collection system with no lateral resolution, considerable care must be taken over the design of an imaging system. In particular, optical aberrations which degrade the final image quality must be reduced to an absolute minimum. The optical design described here was the work of the author and the lenses themselves were figured by Knight Optical (UK) Ltd., Harrietsham, UK.

3.1.1 Design Considerations

A primary design goal for XEOM1, as with ODXAS1, was to maximize the total collected light intensity. The Poissonian noise introduced by the random nature of XEOL emission ensures that the maximum signal-to-noise ratio is $S/N = 1/\sqrt{n}$, where n is the total measured signal, although instrumental and other effects will reduce this (see Section 3.3.5). Nevertheless, significant gains in data quality can be made through maximising the potential for light collection. Additionally, a greater visible photon flux will lead to reduced exposure times for the same statistical precision and consequently enhances the potential for time-lapse studies of chemical processes over shorter timescales.

The primary factor which determines the light collection efficiency of a microscope system is the cone of acceptance of the objective which is described by the object-side numerical aperture $\mathrm{NA} = n \sin \alpha$, where n is the refractive index of the medium in which the lens is working (in this case air, so $n = 1$). Light emitted from the sample at an angle greater than α will not be collected by the optical system. In order to allow for a reasonable range of X-ray beam incidence angles — providing adaptability when mounting on different beamlines — sufficient space must be left around the sample. This imposes a limit on the minimum distance between the sample and the first lens, and the diameter of the objective, which in turn sets a practical limit on the maximum numerical aperture which can be achieved.

Signal intensity is also affected by the transmission profile of the glass(es) used in the optical system. XEOL emission can occur across the whole trans-visible region, depending on the sample, so it is advantageous to try and capture the widest emission bandwidth as possible. A requirement of the glass which is particular to the optics of XEOM1 (and ODXAS1) is that it exhibits little (or no) XEOL emission itself. It is likely that a significant flux of scattered X-rays will strike the first surface of the objective lens in particular, and any light emitted as a result will contribute to the background signal level. For these reasons, UV-grade fused silica (UVFS), with its transmission of $> 90\,\%$ from 200 nm to over 1 micron (also used for the optical elements in ODXAS1), is an obvious choice.

Further to this, there will be an accumulation of losses caused by reflection of light at the air-glass interfaces of each lens. The reflectance R, defined to be the ratio of reflected flux to incident flux, is described by the following Fresnel equation:

$$R = \left(\frac{n_t - n_i}{n_t + n_i} \right)^2 \tag{3.1.1}$$

where n_i and n_t are the refractive indices of the incidence and transmitting materials respectively [1]. Equation 3.1.1 is valid for light at normal incidence to the surface, a suitable approximation for the majority of lens systems since the angles of incidence w.r.t. the surface normals are usually small. It should be noted that reflection occurs from both surfaces of a lens, so a single UVFS lens will exhibit $\sim 7\,\%$ losses (wavelength $\lambda = 588\,\text{nm} \implies n = 1.46$) [2] due to reflection alone. Therefore, keeping the number of optical elements to a minimum is clearly advantageous.

3.1.2 Lens Design and Simulation

The lens system of XEOM1 has been designed using OSLO (Optics Software for Layout and Optimization) [3], a ray-tracing software package. Specification of the lens elements is done in a spreadsheet and the user can also control the source (object) characteristics (Figure 3.1). Each row represents a surface in the optical system which is defined by its aperture radius, radius of curvature, and the distance and material (air, or type of glass) between it and the next surface. Each surface also has a range of special parameters which can be assigned. Lens surfaces are most commonly spherical i.e. they have constant radius of curvature R. Lenses of this type are susceptible to *spherical aberration* where, for a convergent lens, the focal point moves closer to the lens for rays incident further from the optical axis. This is a particular problem for high numerical aperture lenses, but can be corrected through the use of *aspherical* surfaces. Such surfaces are defined by setting non-zero values for the conic constant k and the n^{th}-order aspheric deformation coefficients A_n, such that the sag (deviation) Z of the surface parallel to the optical axis is given by

$$Z(r) = \frac{Cr^2}{1 + \sqrt{1 - (1+k)C^2 r^2}} + A_4 r^4 + A_6 r^6 + A_8 r^8 + \cdots \,, \qquad (3.1.2)$$

where r is the radial distance from the optical axis, and C is the curvature (here defined as the inverse of the lens surface radius $C = 1/R$) [4]. Although conventional lens figuring methods naturally produce a spherical surface, with modern techniques it is not significantly more difficult to produce aspheres.

One surface in the system (not necessarily a lens surface) must be defined as the *aperture stop*; this is the aperture which limits the amount of light which can reach the image plane i.e. it determines the brightness of the image. Any surface may also be set as reflective for modelling mirror-based systems. A host of reports (both text and graphic) can be generated about various aspects of the system which enable the user to evaluate the performance of the optics.

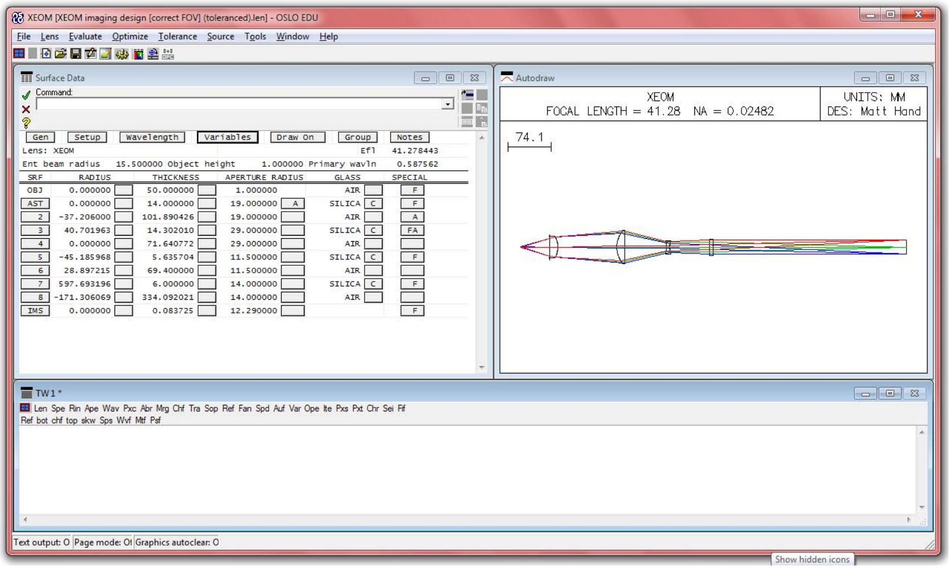

Lens: XEOM Efl 41.278443

Ent beam radius 15.500000 Object height 1.000000 Primary wavln 0.587562

SRF	RADIUS		THICKNESS		APERTURE RADIUS		GLASS		SPECIAL
OBJ	0.000000	☐	50.000000	☐	1.000000		AIR	☐	F
AST	0.000000	☐	14.000000	☐	19.000000	A	SILICA	C	F
2	-37.206000	☐	101.890426	☐	19.000000	☐	AIR	☐	A
3	40.701963	☐	14.302010	☐	29.000000	☐	SILICA	C	FA
4	0.000000	☐	71.640772	☐	29.000000	☐	AIR	☐	☐
5	-45.185968	☐	5.635704	☐	11.500000	☐	SILICA	C	F
6	28.897215	☐	69.400000	☐	11.500000	☐	AIR	☐	☐
7	597.693196	☐	6.000000	☐	14.000000	☐	SILICA	C	F
8	-171.306069	☐	334.092021	☐	14.000000	☐	AIR	☐	☐
IMS	0.000000	☐	0.083725	☐	12.290000	☐			F

XEOM
FOCAL LENGTH = 41.28 NA = 0.02482
UNITS: MM
DES: Matt Hand

Figure 3.1: *Main user interface of OSLO. Visible are the 'Surface Data Spreadsheet' where the basic lens parameters are specified, the Autodraw graphics window which displays an automatically updating 2D plan of the optical system, and a text window where report data are displayed.*

Optimization of the lens design is achieved by nominating a subset of the design parameters as variables, and these are then adjusted to minimize some error function. OSLO incorporates the GENII error function [5] which uses 10 rays to a define a 31-term merit function utilizing the relationships between classical aberrations (spherical, coma, astigmatism, Petzval curvature, chromatic, etc.) and the exact ray data. The error function ϕ is constructed from *targets* representing these aberrations and is defined by

$$\phi = \sum_{j=1}^{N} \left(\frac{A_j - D_j}{T_j} \right)^2 , \tag{3.1.3}$$

where A_j and D_j are respectively the actual value (for the existing lens system) and the desired value of the j^{th} target. T_j is the tolerance of the j^{th} target i.e. it is the acceptable amount that the j^{th} target is permitted to deviate from the desired value in either direction. Therefore, $1/T_j$ is a weighting factor on the error $A_j - D_j$ and ϕ is the weighted sum of each error squared. This error function is minimized using the *downhill simplex* method of Nelder and Mead [6], the implementation of which in OSLO is described in *Numerical Recipes in C* [7].

The evolution of the XEOM1 optical design is illustrated in Figure 3.2. The final design comprises four lens elements, all figured from UV-grade fused silica (Figure 3.3). The first two lenses form the objective of the system with the first lens also acting as the aperture stop. The second and third lenses act together to reduce the diameter of the image ray bundle so that it may pass through a 25 mm diameter optical filter placed between lenses 3 and 4, allowing re-use of those which have previously been used with ODXAS1. The final lens corrects the magnification to a fixed value of 11.93×. This has been chosen so that the image fills the largest dimension of the initial CCD camera to be used (Section 3.2.2), and so that a subsequent large-area square sensor with comparable dimensions will also be filled. The numerical aperture of the optical system is 0.29. When compared with a modern high-resolution microscope — these can achieve NA upwards of 1.0 — it seems relatively small, but these have very short working distances. Considering the 50 mm working distance of XEOM1 this is actually very reasonable.

A consequence of using a single glass type is that the system is naturally chromatic so, for a given configuration, the focus is optimal only for a single wavelength of light. A further function of lens three is to select the wavelength for which the optics will be best focused. This is done by translating the lens along the optical axis in the space between the elements either side. By introducing a filter with a single pass band around this wavelength, an optimally focused image can be obtained. If this is not done, a significant flux of photons at unfocused wavelengths will be distributed across the image surface, reducing the contrast and spatial resolution.

Manufacturing tolerances were set by utilizing the user-defined tolerancing function in OSLO. Here, an error function is defined and the values to be toleranced are set as variables. Limits on these values are then calculated such

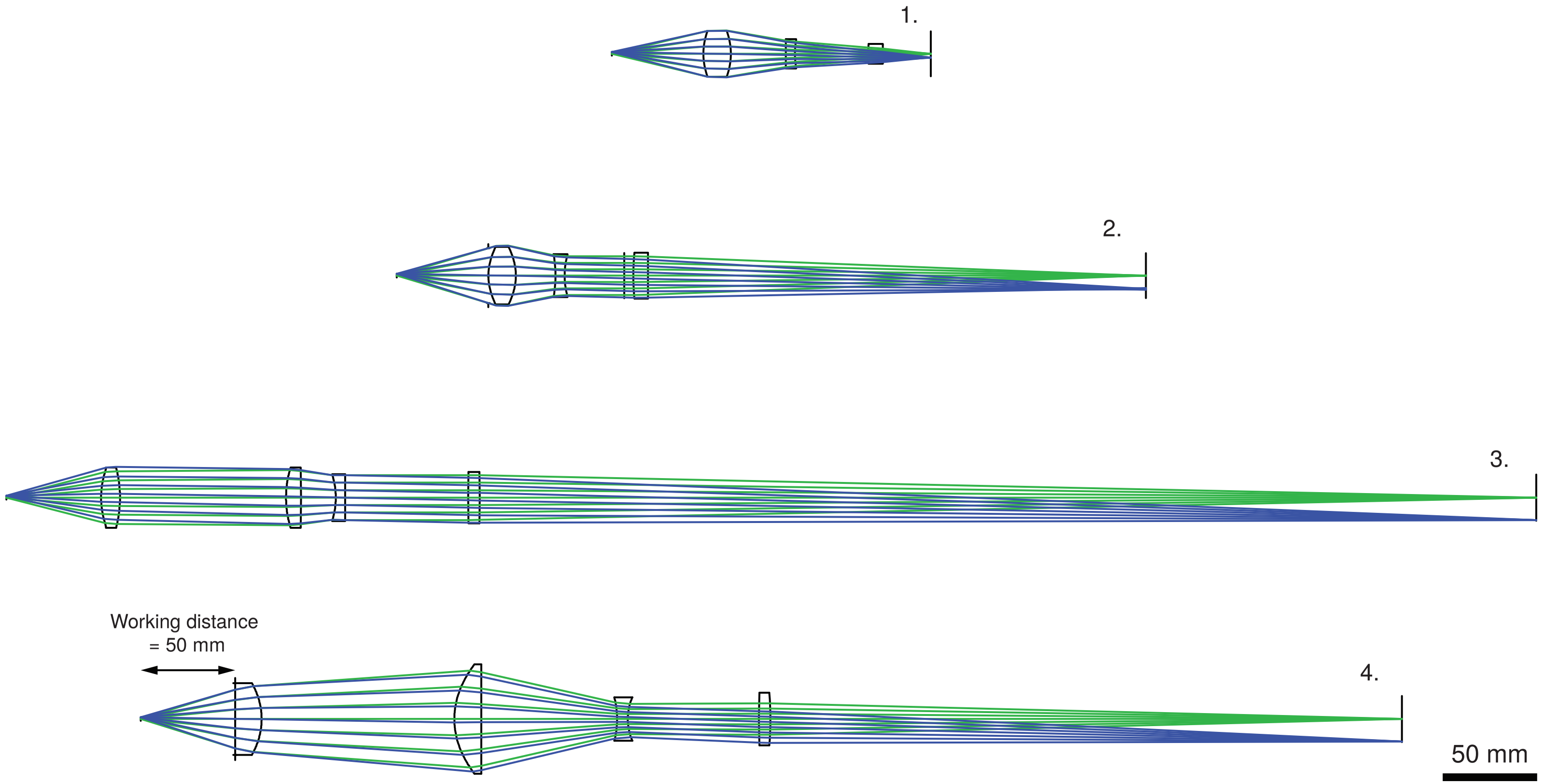

Figure 3.2: *Evolution of the lens system design (from top to bottom). The designs are to scale and the diameter of the image plane is fixed at* 24.6 mm *which corresponds to the largest sensor dimension. Ray bundles emanating from the centre (green) and edge (blue) of the field of view of each system are shown. Early designs utilized three lenses, but later iterations split the objective into two lenses in order to provide greater control over aberration correction. Designs* 1–3 *show the changes made to increase in magnification from* 4 × *to* 8 ×*, and finally to* 12 ×*. Initially set at* 30 mm *diameter, the first objective was increased to* 40 mm *diameter enabling greater light-collection capacity. Design* 4 *is the final XEOM1 layout.*

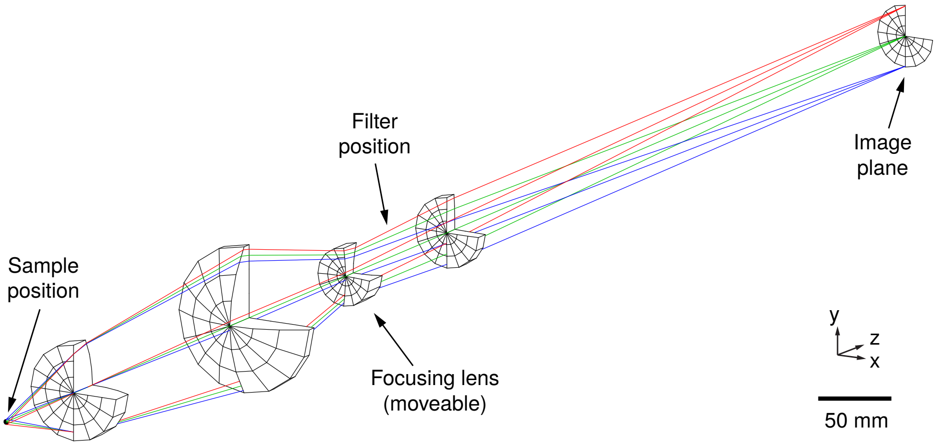

Figure 3.3: *Projection of the final XEOM1 lens layout. The red, green and blue ray bundles are traced from the fractional coordinates 1.0, 0.0, and -1.0 respectively of the object radius.*

that the error function does not increase by more than a specified amount. The GENII error function was again used for this purpose and was restricted to increase by no more than 1 %. Due to manufacturing limitations, the element thickness tolerance initially specified was relaxed, and no guarantee could be made on the exact refractive index of the glass.

3.1.3 Evaluation of Optics

Given that the lens system has been designed by tracing rays representing light of a particular (design) wavelength, it is natural to expect that the best imaging performance will be obtained at this wavelength with the focusing lens in its nominal position. A ray intercept diagram can be used to indicate the residual aberrations remaining in the system which might degrade image quality. This plots the intercept position of rays in a bundle originating from a particular object position as a function of fractional entrance pupil coordinate. Since the aperture stop is at the first lens surface this is also the entrance pupil. The intercept positions are given relative to the intercept of the *principal ray*, that is, the ray from a given bundle which passes through the center of the aperture stop. Given in Figure 3.4, the top-to-bottom extent of the ray intercept diagram indicates the size of the image blur. Off-axis i.e. in the worst case, this has an RMS value of 5.78 µm which is much less than the 12 µm pixel size of the imaging sensor. However, this does not take diffraction effects into account. The finite aperture of an optical system leads to a point source being imaged as an Airy disc [1]. When two such sources are sufficiently close together the diffraction rings will overlap, so the maximum resolution which can be achieved is then given by the minimum separation required in order to determine that the two points are distinct. This is most commonly determined using *Lord Rayleigh's criterion* which states that this occurs when the maximum of one Airy pattern is coincident with the first minimum of the other, a distance that is given by

$$Z = \frac{0.61\lambda}{\mathrm{NA}} \, . \tag{3.1.4}$$

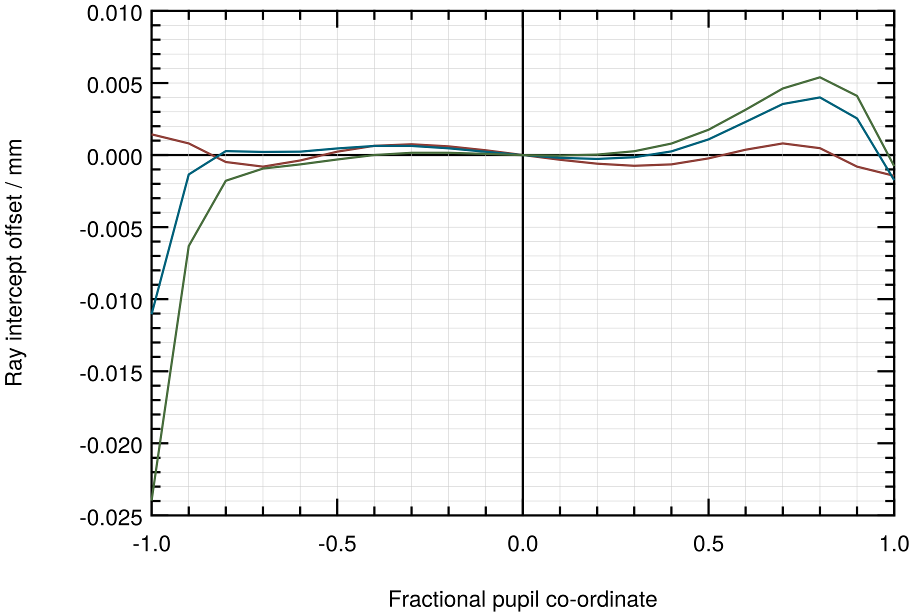

Figure 3.4: *Ray intercept plot of the XEOM1 optics at the design wavelength. The ray intercept offset values are given relative to the principal ray in the y-direction (see Figure 3.3 for co-ordinate convention). The green, blue, and red curves correspond to the fractional object radii* 0.0 *(on-axis),* 0.7*, and* 1.0.

The minimum separations Z_O and Z_I of object and image points are determined using the object- and image-side numerical aperture respectively. It is clear from Equation 3.1.4 that the maximum theoretical resolution increases with numerical aperture. In the case of XEOM1, this is limited by the image-side

NA of 0.02482 which gives $Z_I = 14.43\,\mu\text{m}$, corresponding to a lateral resolution of $14.43/11.93 = 1.21\,\mu\text{m}$. As the resolution is limited by diffraction effects rather than optical aberrations the optical system is said to be *diffraction-limited*. Note also that Z_I is larger than the pixel size so this is not a limiting factor, and there are no gains in resolution to be made by using a sensor with smaller pixel dimensions.

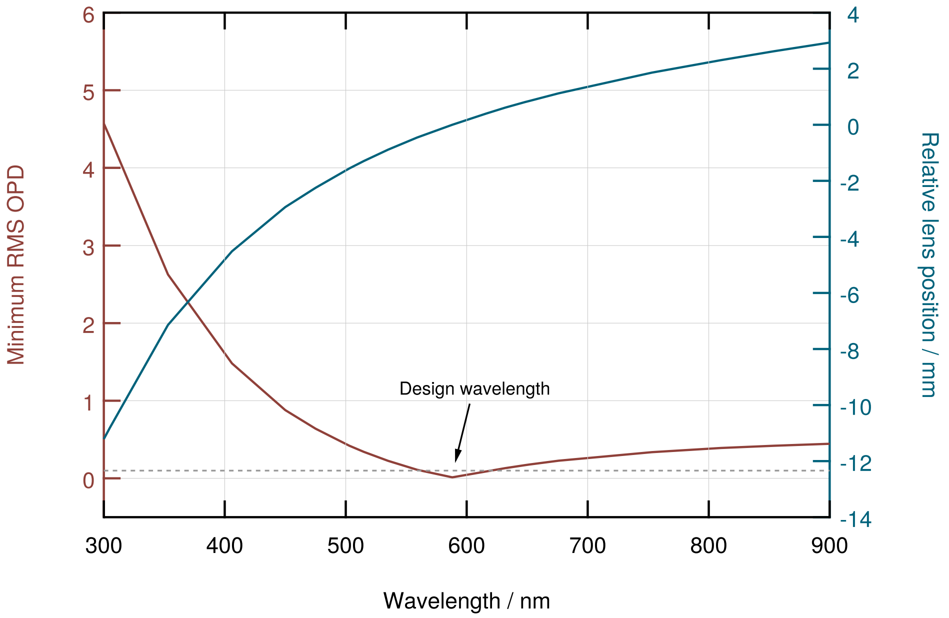

Figure 3.5: *The best focus at any given wavelength is found at the lens position which gives the smallest overall wavefront distortion, or optical path difference (OPD). The RMS OPD at the lens position (blue curve) which minimizes its value at a particular wavelength is given by the red curve. The dashed line indicates the Raleigh limit for RMS OPD (1/10 wavelength). The lens positions are given relative to the position of lens 3 in the design configuration.*

In order to obtain a focus over a range of wavelengths using monochromatic optics the lens configuration must change to compensate for the change in refractive index (dispersion). The power of lens 2 required to sufficiently reduce the ray bundle diameter for it to pass through the filter without vignetting introduces the largest focal shift with wavelength. Therefore, the function of lens 3 is to maintain its position relative to the changing focal point of lens 2, guiding the selected wavelength through the remaining optical elements. When ray-tracing, the optical aberration is thought of as the deviation of a given ray from its optimal path, but this is equivalent to the distortion of the optical wavefront from the ideal spherical (planar for parallel rays) surface. Thus, the required position of lens 3 for a given wavelength is found by minimizing the wavefront error at the image plane (Figure 3.5).

In a perfect optical system the peak-to-valley (P-V) wavefront distortion is less than 1/4 wavelength, the *Rayleigh limit*. However, this measure is susceptible to a large error in only a small wavefront region which has a comparatively small effect on the overall image quality. A more realistic figure of merit is the RMS wavefront error; the Rayleigh Limit then becomes 1/10 wavelength. In Figure 3.5 we can see that this condition is met only for a narrow range of wavelengths about the design wavelength. For longer wavelengths than the design wavelength the OPD wavefront error increases but then plateaus, indicating that the highest quality images should be obtained in this range. At wavelengths shorter than the design wavelength the image quality degradation is more significant. However, accessing the UV range is only possible because of the glass choice so the trade-off is unavoidable.

3.2 Hardware

A microscope system consists of much more than its optics. Apart from the optical column itself, there are variety of supplementary components and control systems. What follows is a complete description of the XEOM1 hardware, including both the permanent components which form the core of the system, and the interchangeable and optional components which enhance its adaptability. The modular nature of the system also enables it to be efficiently packed for transport to and from synchrotron facilities. The mechanical design and construction of the optical column and the auxiliary components was the work of my supervisor, Prof. Mark Dowsett.

3.2.1 Optical Column

As with ODXAS1 — and for the same reasons, *viz.* its effectiveness at blocking visible light and low XEOL emission — the optical column (Figure 3.6) has primarily been constructed from black acetal copolymer. Additionally, plastic construction gives a considerable weight reduction in comparison with metal components. The column components are mounted on an optical rail which allows for consistent and precise alignment of the optics, and serves as a robust and stable component for mounting the system on a beamline.

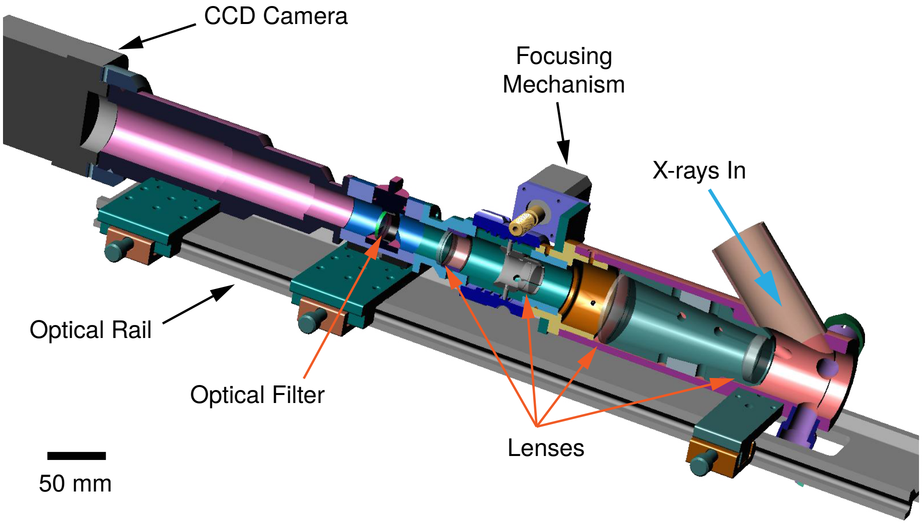

Figure 3.6: *3D section view of the XEOM1 optical column exported from Alibre Design (now Geomagic Design 2013), 3D Systems Inc. The final stage of the column differs when mounting the Andor camera: due to its additional weight, the camera is affixed to an aluminium extension plate which is itself screwed onto the underside optical rail. The sample stub is omitted from this figure.*

The first section of the column contains the first two lenses which form the optics objective. These are clipped into each end of a 'cartridge' which slides into the outer housing. The length of the cartridge precisely sets the lens spacing and the absolute position of each lens is set by complete insertion of the cartridge. A number of angle ports protrude from the base of the column at 10°, 30°, 45°, and 60° w.r.t the plane orthogonal to the optical axis. These are all directed towards the sample position at the base of the column and allow for a variety of accessories to be used for illumination, monitoring, modification and signal detection. The angle ports also serve as entry points for the X-ray beam so no matter how a beamline end station is configured it should be possible to get the beam onto the sample. A set of plugs has been produced to block the entrance of any angle ports not being used for a given experiment. A hole in the plug for the (largest) 45° port allows it to also accept components designed to mate with the 10° ports.

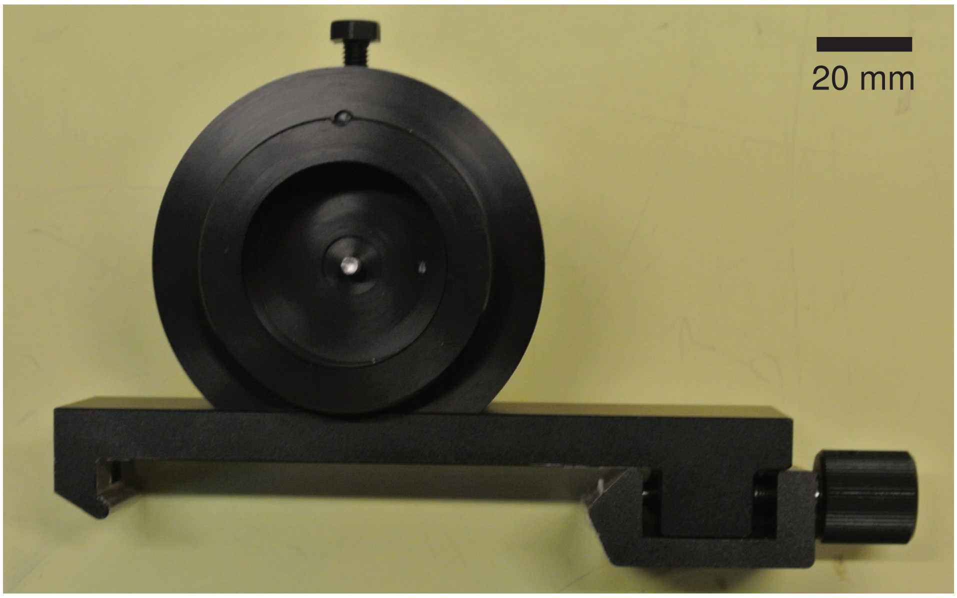

Figure 3.7: *The XEOM1 end cap prevents external light from entering the optical column. The mount point at the centre of the stub accommodates a variety of specially designed sample holders (Figure 3.8) and ensures that the sample itself is always centred within the field of view of the optics.*

The central section of the column incorporates the mechanism used to translate the third lens for focusing of the optics, and also contains the final stationary lens. The third lens is held within its own cartridge from which a metal pin protrudes from either side. The pins engage with a pair of large pitch spiral grooves on the inside of a freely-rotating outer sleeve. Forced rotation of the outer sleeve in one direction or the other then drives the lens up and down the column. This is done using a worm drive mechanism — the teeth of the worm gear are machined into the outer sleeve which is driven by a worm mounted on the spindle of a NEMA-17 frame stepper motor. If the mechanism is driven too far the lens pins disengage at the end of the groove, so spring-loaded wires at each end of the mechanism push on one of the pins, forcing it to re-engage when driven in the opposite direction. A later enhancement to the focusing mechanism was the addition of a position sensor (not pictured). This takes the form of a linear potentiometer which engages with a spiral groove on the outside of the rotating sleeve. Importantly, this groove has the same pitch as the inner groove so when the sleeve rotates there is a 1:1 correspondence between the position of the lens and the value of the potentiometer. Therefore, by measuring the voltage across the potentiometer, the position of the lens can be unambiguously determined; this forms the basis for the feedback system used to move the lens to a pre-determined position for focusing a particular wavelength (Section 3.3.3). The precision of the drive mechanism is sufficient to position the focusing lens such that the actual focused wavelength is within $\sim 2\,\mathrm{nm}$ of the desired wavelength in the worst case (in the infra-red regime). This is much smaller than the narrowest bandwidth filter which has been used with XEOM1 (see Section 4.5.3), so is not a limiting factor in the image quality.

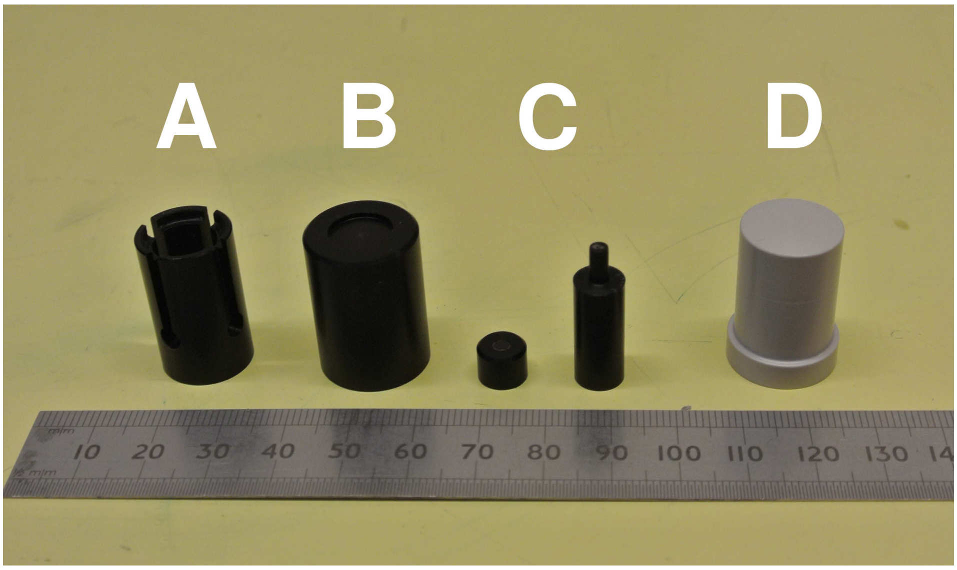

Figure 3.8: *Different sample holders for (A) coupons (B) powder, and (C) grids which fit into the XEOM1 sample stub. The final grey sample holder (D) is a dummy working electrode, originally used with the eCell, which can be used to mount thin samples by simply sticking them to the flat surface.*

In order to avoid the previously mentioned problem of light entering the optical system through the translucent eCell walls, a dedicated black acetal sample stub was developed which fits into the bottom of XEOM1 in place of the cell (Figure 3.7). A variety of specialized holders accompany the stub for mounting different types of sample (Figure 3.8). The first holds the regular 12.5 mm diameter coupons (see Section 4.2.1) which are used as substrates for artificial corrosion layers. The second is a powder holder with a 2 mm well depth. The final sample holder is designed to hold 3.05 mm diameter TEM grids which are artificially corroded to produce a corrosion distribution in a well-defined geometrical pattern (see Section 4.2.2 for further details). The stub can also accommodate the working electrodes used in the eCell. The height of each sample holder is identical and has been chosen such that the surface of the sample is reliably positioned in the focal plane of the optical system (50 mm from the surface of the first lens). The sample holders simply screw into the bottom of the sample stub, so changing samples only takes a few minutes which is short compared with current data acquisition times of up to several hours (see Section 4.5). For this reason, automation has not yet been considered for sample changing as this is done much less often than changing of the optical filter; a filter changing wheel is currently under development as discussed in Section 5.3.

3.2.2 Detectors

Data obtained via different methods can provide additional insight into the system being studied. With this in mind, XEOM1 has been designed to operate using a number of different detectors. Clearly the primary detector should be an imaging device and two different CCD cameras have been used with XEOM1. The array of angle ports around the base of the optical column allow for many other secondary detectors to be mounted for parallel measurement of other signals.

FLI CCD Camera

The first camera purchased for XEOM1 was a Microline ML1109 spectroscopy CCD camera manufactured by Finger Lakes Instrumentation (FLI) LLC, Lima, USA [8]. The basic specifications of the camera as advertised by the manufacturer are outlined here. As will be seen in Section 4.4, the camera — particularly the sensor — has fallen short of expectations.

One of the most appealing aspects of this camera, in terms of integrating it into the XEOM1 system, is its size. In order to keep XEOM1 as portable as possible, it has been important to use relatively compact components. In the case of the camera, weight is also of critical concern as it must be supported by the rail onto which the optical column is mounted. A 25 mm diameter shutter

Sensor Specifications

Sensor	Hamamatsu S10140-1009
Array size	1024 × 506
Pixel size	12 µm
Full well capacity	$75\,000\,\mathrm{e}^-$
Sensor dimensions	24.58 × 6.072 mm

Electronics Specifications

Digitization speed	500 kHz
Typical system noise	$10\,\mathrm{e}^-$ RMS @ 500 kHz
Typical maximum cooling	65 °C below ambient
Typical dark current	$< 0.04\,\mathrm{e}^-\,\mathrm{pixel}^{-1}\,\mathrm{s}^{-1}$ @ −40 °C
Linearity	$> 99\,\%$

Table 3.1: *FLI Microline ML1109 spectroscopy CCD camera specifications.*

with a 40 ms open/close time is integrated into the camera. The compactness of the FLI camera compromises its cooling capability which is provided by a single-stage thermoelectric cooler. However, the inherently low thermal noise level of the back-thinned S10140-1009 CCD sensor (Hamamatsu Photonics K.K., Japan) fitted in the camera more than makes up for the modest cooling level.

Andor CCD Camera

While it was intended that a second CCD camera be purchased to replace the FLI camera, freeing it up to be integrated into the planned spectroscopy arm, it was the difficulties we had with the first camera which eventually prompted the decision. The quantum efficiency curves for the sensors in both the Andor and FLI cameras are given in Figure 3.9. The UV-enhanced coating applied to the e2v sensor provides reasonable efficiency in the UV region, although it reduces the efficiency somewhat for visible wavelengths when compared with the standard broadband coating ($\sim 60\,\%$ rather than $\sim 90\,\%$). Further details about the Andor camera and continued comparison with the FLI Microline can be found in Section 4.4.3.

Sensor Specifications

Sensor	e2v CCD42-40 NIMO Back Illuminated
Array size	2048 × 2048
Pixel size	13.5 µm
Full well capacity	$100\,000\,\mathrm{e}^-$ (minimum)
Sensor dimensions	27.6 × 27.6 mm

Electronics Specifications

Digitization speed	5 MHz (maximum)
Typical system noise	$31.5\,\mathrm{e}^-$ RMS @ 5 MHz
Typical maximum cooling	70 °C below ambient
Typical dark current	$0.4\,\mathrm{e}^-\,\mathrm{pixel}^{-1}\,\mathrm{s}^{-1}$ @ −70 °C
Linearity	$> 99\,\%$

Table 3.2: *Andor iKon-L large area sensor CCD camera specifications. The readout speed may be adjusted; reducing this lowers the read noise in the final image.*

Hamamatsu Photomultiplier Tube

The main detector on ODXAS1, the Hamamatsu H8259-01 PM tube, is now being used as a secondary detector on XEOM1. The flange on the shutter has been fitted with a hollow plug which is designed to engage with the 10° angle ports. Adapters have also been made so that the PM tube can be fitted to the 45° port, and also in place of the CCD camera at the end of the optical column. In the latter configuration, the PM sensor lies in the image plane of the optics. Utilizing the PM tube in this manner allows for total XEOL spectra to be acquired in situations where lateral resolution is not required, while still taking advantage of the greater light collection capability of the optical column. Experiments in this configuration have been carried out in order to compare the total XEOL intensity measured using the FLI CCD camera and the PM tube.

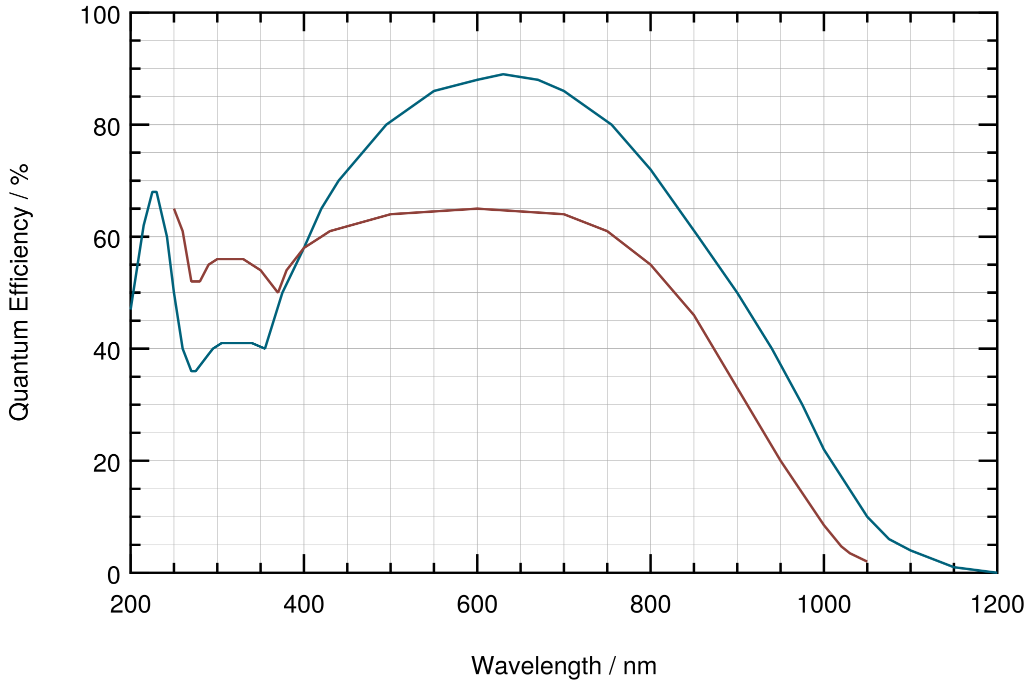

Figure 3.9: *Quantum efficiency curves for the Hamamatsu S10140-1009 and e2v CCD42-40 NIMO CCD sensors fitted in the FLI and Andor cameras respectively. Data taken from the manufacturer-supplied data sheets.*

Avalanche Photodiode

For parallel measurement of fluorescence X-ray absorption spectra an avalanche photodiode (APD) detector has been used (supplied by the XMaS beamline). This consists of a silicon avalanche photodiode chip (PerkinElmer Inc., Hopkinton, USA) and integrated preamplifier. The chip active area is 5 × 5 mm and is protected by an 80 μm thick beryllium window mounted onto a KF-16 vacuum flange. To minimize the detection of backscattered X-rays the fluorescence detector should ideally be positioned close to 90° from the X-ray beam axis. Since the minimum angle between sample surface normal and the beam axis is 30° (imposed by the angle ports), the maximum angle of the APD w.r.t. the beam is 50° (see Section 4.1.1).

3.2.3 Auxiliary Components

Two types of sample illuminator can be used with XEOM1; a small filament lamp, and a more sophisticated LED illuminator (designed by Prof. Mark Dowsett) built especially to fit into the angle ports. These have been used during alignment of XEOM1 on the beamlines; they provide a low-level of illumination so it is possible to tell when the X-ray beam is roughly centred on the sample (see Section 4.4.1). It is desirable to use LEDs for illumination since, when compared with the filament lamp, their luminous intensity is far more linear with current, and they do not exhibit any color shift as the input current changes. However, phosphorescence of the LED after it has been switched off is a problem as this contributes a decaying background signal to any subsequent XEOL measurement. This is countered by incorporating a shutter into the illuminator which operates in conjunction with the LED itself, opening and closing when the LED is switched on and off.

USB webcams may also be fitted to the angle ports in order to provide additional color images of the sample surface, although their usefulness is a little limited as they can be difficult to focus. Nevertheless, they have previously been used on ODXAS1 to provide a visual record of time-lapse experiments (in conjunction with the illuminator), so this will also be done with XEOM1 in the future. A small red laser can also be controlled as part of the XEOM1 system, providing a source of optical excitation if required (not used as part of this project).

3.2.4 Control and Data Acquisition

The portable nature of the XEOM1 system requires that the control interface be as self-contained as possible; an interface with the host beamline system should be provided only where absolutely necessary. Like the precursor system, experiments are controlled via a laptop computer. Here we discuss the data acquisition system (DAQ), which also provides the interface for controlling the XEOM1 hardware. The associated software is discussed in Section 3.3.

The computer interface for ODXAS1 was provided by two Exacq Technologies CM Series DAQs — a CM-2120 and a CM-2151. The CM-2120 DAQ is equipped with 16 analog inputs, 2 analog outputs, and 16 digital I/O channels. The maximum sampling rate on the analog channels is 250 kHz and input gain is switchable between 1x, 2x, 4x or 8x. The higher specification CM-2151 doubles the number of analog input and digital channels to 32. It also offers higher gain settings — 1x, 10x, 100x, and 1000x — which are used for measurement of electrochemical parameters when using the eCell in conjunction with a custom-built potentiostat. While the Exacq interfaces would be perfectly suitable for controlling the new system, the major issue going forward is that the PCI cards need to be adapted to connect to a laptop. This is done via a Magma PCI-to-PCMCIA chassis; however, PCMCIA cardbus interfaces are now obsolete so hooking these DAQs up to a current generation laptop is not possible. Additionally, driver support has ended for both the Exacq boards and the Magma chassis so running the setup from a modern OS would likely be problematic.

A new set of DAQ interfaces — two Agilent U2353A multifunction cards — had been purchased before this project even began with the intention of directly replacing the Exacq boards to control the old hardware. Consequently, they provide comparable functionality to the previous hardware (Table 3.3). However, the system was never implemented so the interfaces have now been integrated into the new design. The Aglilent DAQs are mounted in a U2781A modular chassis so only a single USB interface is required. The additional module capacity provides for the possibility of further expansion in the future.

3.2.5 Electronics Interface Unit

The electronics interface unit (EIU) contains an assortment of electrical hardware required for operation of the auxiliary hardware not under direct control of either the laptop via USB (CCD cameras, webcams), or the beamline system (secondary detectors). It was conceived out of the desire to consolidate the switching and stepper motor control hardware from the legacy system, and to expand its capacity — in particular, to allow for control of more stepper motors. Figure 3.10 shows a functional block diagram of the EIU components and their connectivity to the other hardware. Design and construction of the new control system has been carried out by the author, with assistance from Adrian Lovejoy (Electronics Workshop, University of Warwick).

Internally, the EIU components are arranged on two layers (upper and lower). Connection to the Agilent DAQ modules is via two SCSI 68-way connec-

Analog I/O	
Analog inputs	16 single-ended (or 8 differential)
Maximum sampling rate	500 kHz
Analog outputs	2
Analog resolution	16-bit
Bipolar input ranges	±10 V, ±5 V, ±2.5 V, ±1.25 V
Unipolar input ranges	0–10 V, 0–5 V, 0–2.5 V, 0–1.25 V
Digital I/O	
Number of bits	24 (2 × 8-bit + 2 × 4-bit)
Analog Trigger	
Trigger source	All analog input channels; external analog trigger
Trigger level resolution	8 bits
Digital Trigger	
Minimum pulse width	20 ns
Compatibility	TTL/CMOS

Table 3.3: *Agilent U2353A technical specifications.*

tions — high-density (SCSI-3) on the EIU and ultra-high-density (SCSI-4) on the DAQs. These map to a termination board on each layer from which the internal wiring is distributed to the various components. Photographs of the internal layout of each layer can be seen in Figure 3.11.

The inclusion of two McLennan MSE422 quad-axis stepper motor driver boards allows for control of up to eight stepper motors. This particular model was chosen to in order to match the current requirements of the Portescap 17H218D05B-D motor (only 500 mA per phase) used to drive the working electrode in the eCell. The Saia-Burgess UBL23 stepper motor used to change the eCell volume and manipulate the conformation of the window is of the unipolar type so a third driver board, a Saia-Burgess Samotronic 101, was recovered from

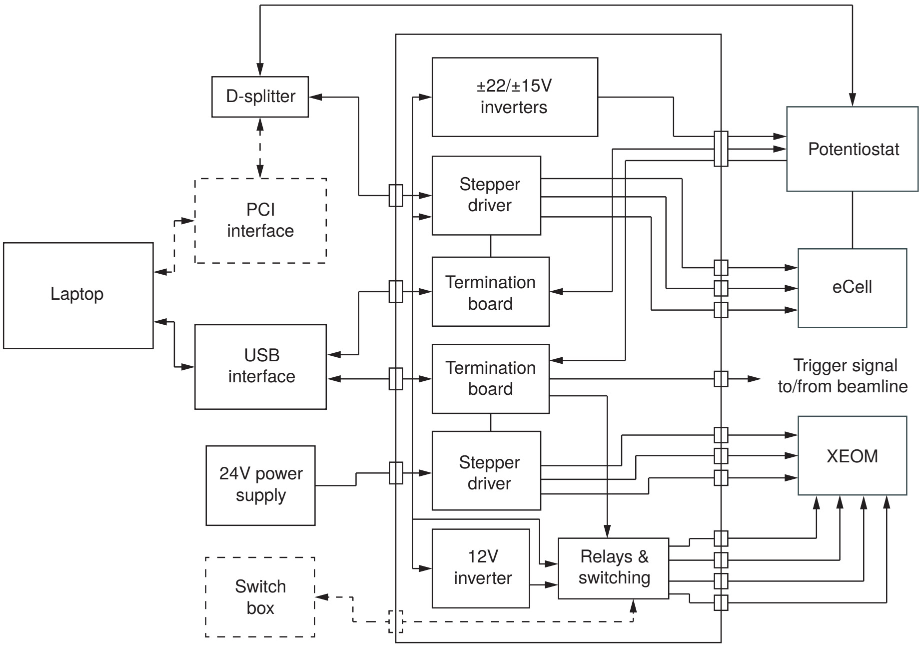

Figure 3.10: *Functional block diagram illustrating the major components in the XEOM1 control system. The original system included a separate remote switch box for operation of the PM shutter and illumination sources. In the new implementation, these components are now operated via a software interface.*

the old system to drive it.

A switching board incorporating transistor and relay circuitry provides control over the state of various hardware components: shutters for both the PM tube and LED illuminator, illuminator intensity, and relays within the potentiostat which set its measurement mode. A 1 kHz pulse train generator is wired to the stepping input for the focusing lens stepper motor as the toggle speed of the DAQ digital outputs is far too slow. The digital output used to trigger the beamline systems (Section 4.1.3) is sent to one input of a four-way TTL logic inverter chip. The output is sent back to the remaining inputs in order to provide three output pulses identical to the original. One of these travels to the output socket and another is sent to the gate input of the counter built into the DAQs. This provides the potential for triggering of, and signal detection from, detectors connected directly to one of the DAQ inputs, but this has not been implemented

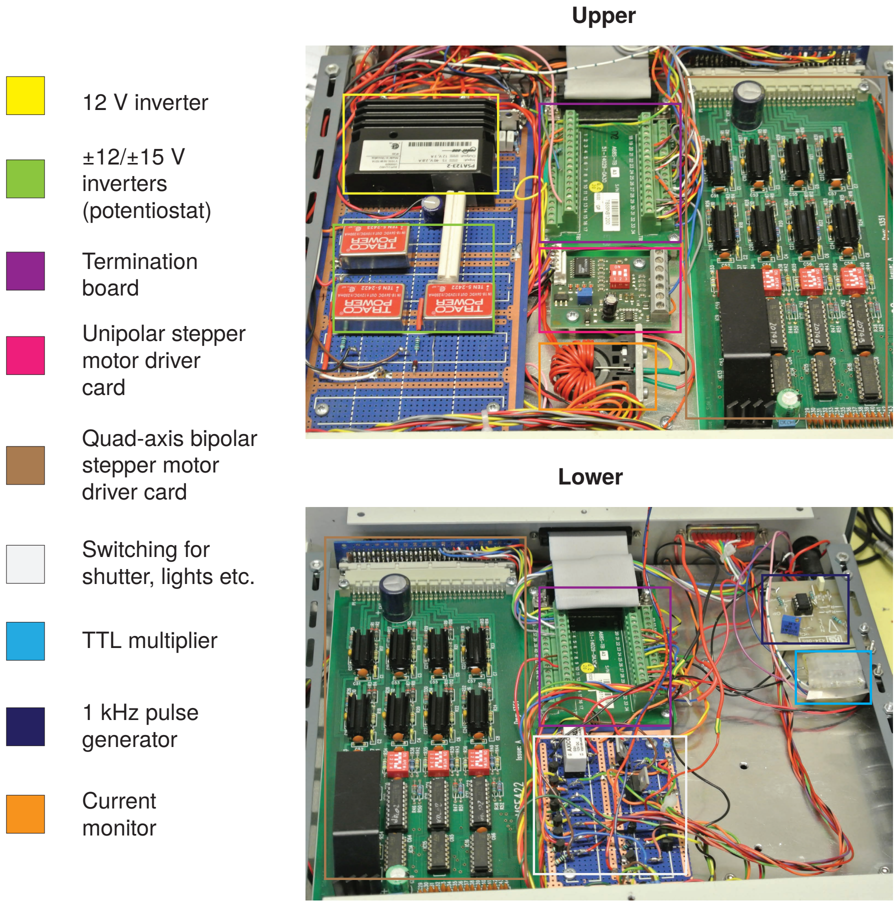

Figure 3.11: *Photos of the components in the (a) top, and (b) bottom of the electronics interface unit. The coloured pads correlate with the colour of the rectangle used to highlight the circuit modules.*

to date.

All components in the EIU are powered by a single 24 V PSU. Some components are powered directly, such as the stepper motor driver. Others require the input voltage to be stepped down; a 12 V inverter provides a supply for many auxiliary components (filament lamp/LEDs/laser), and ±12/ ± 15 V inverters power rails in the potentiostat. For testing purposes, a Hall effect current sensor has been included. This allows the total current draw of all the EIU components to be monitored in order to ensure this does not exceed the capacity of the PSU.

3.3 Control Software

Gathering useful data using XEOM1 requires that images be captured in a very specific way — namely, in synchronization with the stepping of the X-ray beam energy. This is most easily achieved using control software written specifically for the purpose. Creating such software requires that the hardware manufacturer supplies a software development kit (SDK), a software library which allows the user to access and control the low-level functionality of the hardware. It is not unusual for end users of scientific equipment to create their own software solutions so SDKs are typically available.

3.3.1 eCell Controller Overview

eCell Controller, as the name suggests, is a program which was originally developed for operation of the eCell [9]. Its core functionality was aimed at carrying out open circuit potential (OCP) experiments with simultaneous acquisition of 2D XRD data [10]. It has also been used to carry out similar time-resolved experiments measuring X-ray absorption spectra in fluorescence geometry [11]. Now, eCell Controller has been used as a foundation for the XEOM1 control software. Development of all the software features described below has been carried out by the author.

To accommodate the almost complete replacement of the supporting electronics, some portions of the legacy eCell Controller source code have been rewritten for compatibility with the new hardware. However, the bulk of development has gone into implementation of a wide range of new functionality relating to control of XEOM1. The brief for the continued development of eCell Controller was as follows:

1. Re-implement any portions of the existing source code which rely upon legacy hardware for control of the eCell, taking advantage of additional features of the new hardware where possible.
2. Develop a completely new section of the program for control of XEOM1.

eCell Controller has been written using Visual Basic .NET and runs on the Microsoft® Windows operating system. Using such a high-level language streamlines the development process, but it is not without its drawbacks. When eCell Controller was originally written, single-core CPUs were still the norm and multi-threaded applications were only just starting to reach the mainstream. Consequently, critical timing operations were difficult to implement and keeping the UI responsive was a challenge. Nowadays even the lowest specification CPUs have multiple cores and new features which have been introduced into recent versions of the .NET framework make multi-threading a far less daunting prospect. For example, processing image data for display during an experiment can be moved onto a background thread, allowing priority to be given to the timing operations which keep the experiment running on schedule. The laptop which has been used for the experiments described here is a Dell XPS M1330 which is equipped with Intel® Core™ 2 Duo running at 2.4 GHz with 4 GB of memory and a 250 GB hard drive. This model is several years old so the specifications are modest in comparison with the very latest hardware. Nevertheless, running both eCell Controller for operation of XEOM1 and esaProject for data processing (see Section 4.3.1) are well within its capacity.

3.3.2 Imaging Functionality

Scientific CCD cameras generally ship with their own software for capturing images, but when using the supplied software the user is limited to using the camera in the manner intended by the original manufacturer. There is scope for capturing image sequences for XEOL spectrum extraction (to be discussed further in the subsequent chapter) using both the FLI and Andor software (more so using the latter) and both cameras have the capability to send trigger pulses for synchronization. However, given the multi-component nature of the rest of the XEOM1 system this solution is unsatisfactory, hence the need to incorporate image capture functionality directly into eCell Controller.

The Capture Control window is designed to guide the user through the setup and operation of the camera in a logical manner (Figure 3.12). The user must first select which camera they will be using and then set the desired cooling temperature; multiple cameras may be connected simultaneously, although currently only a single camera can be operated at any one time. Before setting the image capture parameters the sensor must stabilize at the temperature to which

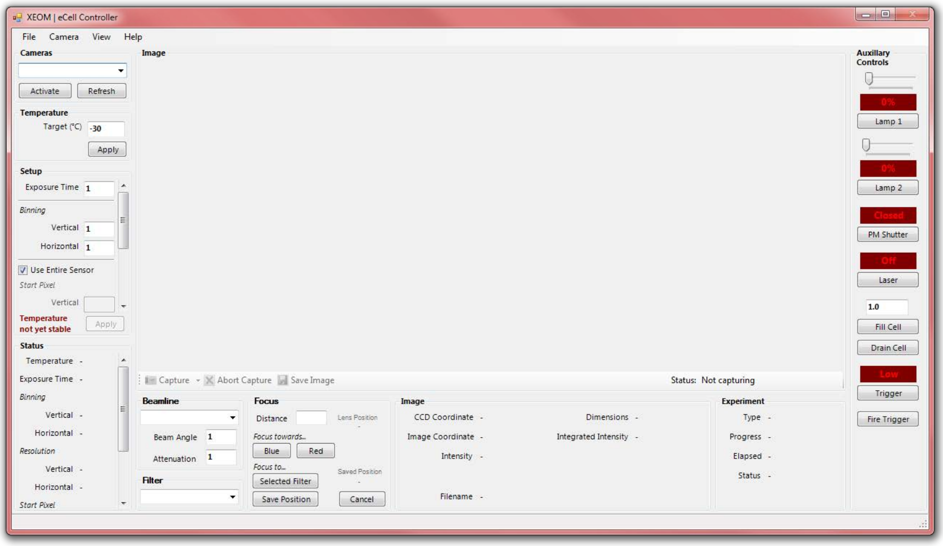

Target (°C) -30

Exposure Time 1

Vertical 1

Horizontal 1

☑ Use Entire Sensor

Vertical

Temperature not yet stable

Temperature -

Exposure Time -

Vertical -

Horizontal -

Resolution

Vertical -

Horizontal -

Start Pixel

Status: Not capturing

Beam Angle 1

Attenuation 1

Distance

Lens Position -

Saved Position -

CCD Coordinate -

Image Coordinate -

Intensity -

Filename -

Dimensions -

Integrated Intensity -

Type -

Progress -

Elapsed -

Status -

0%

0%

Closed

Off

1.0

Low

Figure 3.12: *Screenshot of the eCell Controller 'Capture Control' window. The layout of this window is designed to guide the user through the setup and operation of the XEOM1 system with camera setup at the top left, operation of the camera itself across the middle, and control of auxiliary hardware to the right.*

the cooler has been sent. In fact, the user is prevented from setting values 'out of order' so that it is impossible to incorrectly configure the camera or attempt to acquire images before the required parameters have been set. All fields are validated before being sent to the camera to avoid invalid values being assigned. The following image acquisition settings are available:

Exposure time

Total time for which the shutter is open and the sensor accumulates charge.

Binning

Pixels can be grouped together to form 'superpixels' where the signal acquired by each individual pixel contributes to the total signal in the superpixel. While this reduces the resolution of the image, it is advantageous when the overall signal is low as it reduces the need for very long exposures which will increase the thermal noise. Up to 16 pixels can be binned independently in both the vertical and horizontal directions.

Sensor area

By default the entire sensor area is used, but it is possible to acquire images using only a sub-region within the sensor defined by the upper-left and lower-right pixel coordinates. Since the software package which has been developed for analysis of XEOM data, *esaProject*, has the capability to define regions of interest for extraction of spectra (to be discussed in Section 4.3.1), this feature is somewhat redundant, although it can occasionally still have a use. For example, if one side of the field of view contains an excess of unwanted signal this region can be discarded to avoid compromising the dynamic range of the remaining portion of the image frame.

Frame type

When 'dark' is selected for this parameter, the shutter is forced to remain closed for the duration of the acquisition. This prevents any external light from falling on the sensor, so the only charge build-up which occurs is due to internal processes. This allows for the acquisition of 'thermal' and 'bias' frames (see Section 3.3.5).

Only after values have been assigned to each of these parameters can image acquisition begin. Acquired images are displayed to the user in the center of the capture window. The progress of each individual image acquisition is reported to the lower-right of the displayed image, and the overall experiment progress is presented below this. The different acquisition modes available are described in Section 3.3.4.

Original FLI Camera Implementation

FLI supply an SDK for their products, but it is written in C and so is not directly usable from a .NET project. The SDK file *flicam.dll* is an unmanaged library so method arguments and return values must be carefully marshaled between the managed (VB.NET) and unmanaged (C) code. To make this a little easier, a C++ wrapper library *camera.dll* was written to handle some of the unmanaged memory allocation and error checking. Methods within this wrapper are then exposed by a VB.NET module. The library interface was originally developed by Philip Brondeel (Department of Analytical Chemistry, Gent University) and has later been modified by the author.

Andor Camera Updates

Introduction of the Andor camera required that a significant portion of the camera control functionality be redesigned. The common functionality between the two cameras was abstracted out to an interface `ICamera` so the basic operation of either camera is handled in the same way regardless of which is connected.

Andor also makes available some additional functionality in their SDK when compared with the FLI offering. The speed of the cooling fan can be configured, or even turned off completely, which is of use when carrying out measurements which are particularly sensitive to vibration. Advanced configuration of the CCD sensor electronics is also possible. The horizontal/vertical clock frequencies may be adjusted, affecting the readout speed and read noise. The internal amplifier gain can also be increased in order to increase the resolution of analog-to-digital conversion for small signals. This was also the point at which the requirement for temperature stabilization was included — this is a feature of the Andor SDK, so an equivalent condition was included for the FLI camera.

3.3.3 Hardware Control

A compositional approach has been taken to the hardware control implementation. Classes representing the DAQs and their control channels (digital/analog IO) wrap the Agilent SDK operations. These are assigned to classes which represent the subcomponents of the XEOM1 system: stepper motors, lights, shutters etc. At the highest level, the inter-operation of these lower-level components is handled by classes representing XEOM1 and the eCell. A singleton[1] `HardwareManager()` class handles the hardware class instantiation and assignment, so the virtual system is representative of the real hardware. On startup, all hardware components (except cameras) are initialized so that they begin in a sensible, well-defined state.

---

[1] Singleton is a software design pattern implementation whereby only one instance of the class will ever be instantiated.

Focusing

To manipulate the focusing lens, the user enters the desired translation distance and selects the direction in which it should move (towards shorter/longer wavelength). Since the lens movement speed is fixed by the frequency of the pulse train generator in the EIU, the distance is converted internally to a time period, at the end of which the pulse train is terminated. Movement can be aborted at any time. By omitting the translation distance, the lens can be forced to move indefinitely until either the user manually aborts or a preset software limit is reached. The ability to save the current position of the lens as a preset aids the reproducibility of experiments. Each filter can be associated with a lens position (as determined by the sensor described in Section 3.2.1) which can be recalled at any time.

Auxiliary Hardware

Operation of much of the supporting hardware remains available to the user in each of the main setup windows via a persistent control bar. Each of the lights can be switched on and off, and their respective intensities set. The power to the laser can be toggled, as can the PM shutter state. Manual controls for the remote filling hardware allow the user to remotely fill/drain the eCell by a specified amount. Finally, the trigger output can be toggled between its high and low states, and a pulse can also be sent for manual triggering of the beamline system (if supported by the particular beamline system).

3.3.4 Operational Modes

Three image capture modes are currently available to the user for experiments utilizing the XEOM1 hardware: single image, continuous, and trigger. These have been found to be sufficient for all experiments where only XEOM imaging has been done. However, there is potential for more configuration options to be made available for the existing modes, or for entirely new modes to be created. The most obvious extension to the existing capabilities would be to combine the operation of XEOM1 with the electrochemical cell for spectroelectrochemistry experiments, similar in manner to those carried out using ODXAS1.

Single Image Capture

Acquisition of a single image is the most basic functionality of the camera system. Setup of the exposure is done in the main Capture Control window using the parameters described in Section 3.3.2. When saving the acquired image, the user is given the opportunity to associate some further metadata with the image. The 'title' and 'subtitle' text fields allow a short note about the experiment to be saved with the images. The X-ray beam energy and the beam monitor signal must be entered manually as there is no way to automatically extract this information from the beamline system.

Continuous Capture

When setting up an experiment it can be useful to monitor the effects of changes to the setup on the acquired images e.g. when focusing the optics or aligning the X-ray beam. To aid with this, a capture mode is available whereby images will be continuously acquired until the user aborts. The maximum frame rate is limited by the exposure and image download times, particularly when signal intensity is low. This can be mitigated somewhat by on-chip binning of the pixels, leading to increased signal per pixel and reduced download times, so a frame rate of $\sim 1\ \mathrm{s}^{-1}$ is achievable for very short exposures. A typical focusing strategy would be to use continuous capture with short exposure, binned images to find the best focus, followed by a single image capture using experimental parameters to verify the final quality of the image. Images acquired by continuous capture are not saved automatically as it is intended that this mode be used only for experiment setup purposes.

Trigger Capture

This mode allows for an image sequence of fixed length (a stack) to be captured, primarily for the purpose of extracting XEOL spectra. In order for the stack to be suitable for spectrum extraction each image must be captured in synchronization with the stepping of the beamline monochromator. This is achieved by either 1. sending a signal to tell the monochromator when to step (between images) or 2. receiving a signal from the beamline indicating that a step has occurred and the next acquisition can begin. Here we discuss how these situations are handled by the software; more detail about the beamline hardware interfaces is given in Section 4.1.3.

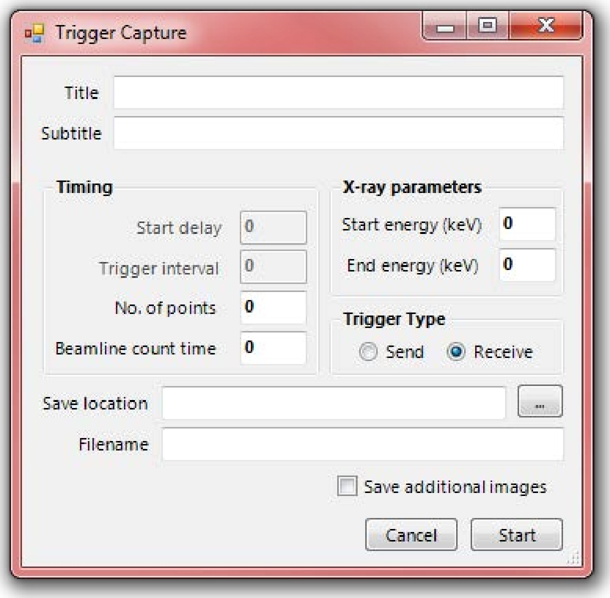
Trigger Capture

Title

Subtitle

Timing

Start delay 0

Trigger interval 0

No. of points 0

Beamline count time 0

X-ray parameters

Start energy (keV) 0

End energy (keV) 0

Trigger Type

○ Send ● Receive

Save location

Filename

☐ Save additional images

Figure 3.13: *Screenshot of eCell Controller trigger capture dialog. If the 'Save Additional Images' option is checked, an extra TIFF format image is saved alongside the ECCD files (Section 3.4.1) which contain the actual data.*

As for a single image capture, the configuration of the XEOM1 hardware and image acquisition parameters for a triggered capture experiment is still done in the main Capture Control window. An additional dialog (Figure 3.13) is presented to the user for configuration of parameters related specifically to trigger capture. The experiment timing parameters differ depending on whether the trigger signal is being sent or received.

Number of points

The value specified represents the exact number of trigger pulses to be sent, or are expected to be received. It is also used in the calculation of the X-ray beam energy for each image.

Start/end X-ray energy

As the XEOM1 system does not control the monochromator directly, the user must enter the range of X-ray energies over which the scan is being taken. These are identical to the scan parameters specified on the beamline system.

Start delay (sending mode only)

When sending the trigger, the user can specific a delay between starting the experiment and the first image being acquired. This functionality has not been used in any experiments to date, but could be useful if, for example, the user wishes to wait until a certain stage in some dynamic chemical process before beginning acquisition to avoid accumulating unwanted data.

Trigger interval (sending mode only)

The time interval between the start of each image acquisition. Since the camera system needs several seconds at least to download each acquired image, the trigger interval must be large enough to accommodate both the image capture and the download time.

Beamline count time (receiving mode only)

There is usually no delay between acquisition of each data point apart from the time allowed for the monochromator to increment. Entry of this parameter is not strictly necessary and is only used to correctly calculate the experiment progress and estimated completion time displayed to the user.

Upon completion of each acquisition in the stack, the image is saved to a user-specified directory with filename consisting of a prefix plus an integer increment. The most recently captured image is also displayed on-screen.

3.3.5 Image Pre-processing

A number of sources within any CCD system introduce background signals and noise into each image. It is not always necessary to apply all corrections (depending on other noise sources), but the following are those which are most commonly applied.

Bias Correction

An unexposed pixel i.e. with no collected photoelectrons, will have associated with it an output level with a mean level and a small distribution about zero. To avoid any negative signal levels generated in the analog stages entering the analog-to-digital converter (ADC), a bias voltage is applied. This is also a countermeasure against temporal drifts due to age, temperature, and stability of the electronics. Bias manifests as offset in the measured signal which must be subtracted from all captured images. The exact bias value varies a small amount from pixel-to-pixel so there are two strategies for dealing with this:

1. A bias frame — a ‘zero’-length dark frame — can be acquired and subtracted pixel-by-pixel from all other image frames. While this is the most accurate method of bias correction, the bias value itself can vary over time so the bias frame should be captured in close proximity to the image frame i.e. a bias frame should be captured just before each image or each sequence of images.

2. If the capability exists within the camera electronics, a more convenient correction method is to ‘overscan’ each captured image. Overscanning is a process whereby the CCD register continues to clock in order to generate additional columns or rows at the border of the image. The values contained in these overscan pixels are representative of the overall bias so can be averaged together to obtain a single value which can be subtracted from all the real image values. This provides a significant advantage over the bias frame method since the value is obtained at exactly the same time as the image, and no additional frames are required. Clearly, this does not account for any pixel-to-pixel variations, but these are usually small enough that aforementioned benefits far outweigh this disadvantage.

Unfortunately, the Andor camera electronics are not capable of overscan. Also, when only using part of the sensor with the FLI camera overscan is not accessible. In both cases the bias frame method must be used. If the user selects the option to perform bias correction (enabled by default), overscan will be used where possible, but if a bias frame is required this will be obtained before each single capture, or at the start of each trigger capture. Bias correction is not applied when using continuous capture as the visual appearance of the image is usually not significantly affected.

Thermal Noise Correction

Thermal excitation of electrons into the conduction band is indistinguishable from excitation caused by photon absorption. The effect is a background signal which accumulates over the duration of an exposure. Deep cooling of the sensor is used to counter this effect, but it cannot be completely eliminated with a practical cooling system. To correct for this the accumulation of thermal signal must be measured for a given exposure time by acquiring a dark frame for the same period. This can be subtracted directly from image frames of the same exposure time (simultaneously correcting for bias and thermal noise). Alternatively, a bias frame can be subtracted to produce a pure thermal frame which can be scaled to any exposure time. The latter assumes that the magnitude of the accumulated thermal noise is proportional to the acquisition time, which is true in most cases[2]. By acquiring thermal frames for regularly used sensor areas and binning settings a library of thermal correction images can be built up and applied to real image frames. Thermal frame subtraction is not done automatically in eCell Controller as the thermal accumulation for shorter exposures is usually insignificant in comparison with other noise sources, but can easily be done after the fact.

Flat-field Correction

In general, when a CCD is exposed to a signal which is absolutely constant – this is the flat-field – across its surface the actual output image is not totally flat. This is a result of non-uniformity in the pixel response to light. Correction of this requires that a flat-field frame be acquired, viz. an image where the optical system is illuminated with a completely uniform source. This is used to divide each image frame, thereby normalizing the pixel response. A satisfactory flat-field source has not yet been established.

---

[2] Scientific CCD sensor quality control usually allows for a handful of 'hot spots' — pixels where the thermal build-up is non-linear. The maximum allowed number of hot spots is always included in the specifications.

3.4 Data Handling

As a result of building custom software for control of XEOM1 (including the camera), we were free to choose how the data were to be stored. A standard scientific image format, namely FITS (Flexible Image Transport System), was considered. However, extending the capabilities of *esaProject* to handle the data generated by the XEOM1, rather than relying on third-party software, was already planned so limiting the data output to an existing format seemed unnecessarily restrictive; creating a new file format provides extra freedom to manage the data in the most sensible manner, rather than forcing it to conform to an existing specification. Hence, the ECCD[3] image format was developed. Should the need arise later on, adding the capability to output in FITS format would be a relatively simple task using a library such as *CSharpFits* [12].

3.4.1 ECCD Image Format

ECCD files have a very simple internal structure designed to be easy to use and flexible. Each file consists of two sections:

- A human-readable text header
- A binary data block

The text (ASCII) header consists of a series of keyword-value pairs which are used to associate metadata with the file. Each pair begins on a new line starting with a # character, followed by the keyword and an =, and then the corresponding value. The keywords themselves are always capitalized, and contain no spaces or special characters i.e. alpha A-Z. The values can be composed of any valid ASCII (non-control) character. A complete header line takes the form

```
# KEYWORD = value\r\n,
```

where `\r\n` is the Windows-style end-of-line (EOL) marker — carriage return followed by line feed, or `CR+LF`. Only three keywords are mandatory:

---

[3] The name ‘ECCD’ is a homage to the file extension of images produced by MarCCD X-ray cameras (Marresearch GmbH, Norderstedt, Germany), ‘MCCD’, which is used extensively for 2D-XRD in other work.

`WIDTH`, `HEIGHT`, and `PRECISION`; these indicate the width, height, and format of the data which are necessary for the binary data to be read correctly. An advantage of using a text header is that opening the ECCD file in a simple text editor allows the user to see all the metadata associated with the image without the need for a special reader.

A single null character always terminates the header block and serves to indicate that only binary data exist beyond this point. The binary image data are stored continuously with data from one row immediately followed by the next. There is no specific character to indicate the end of the file; the header data (`WIDTH` × `HEIGHT`) should be used to calculate how many data points exist. The `PRECISION` keyword can take the following values: `UINT16` (unsigned 16-bit integer); `INT32` (signed 32-bit integer); `BINARY64` (64-bit double precision floating-point). Only `UINT16` are `BINARY64` currently used for raw and processed data respectively.

3.4.2 Data Storage Considerations

The numerical output from both cameras is in the form of 16-bit unsigned integers (0–65 536). At 2048 × 506 (a full frame image from the Microline ML1109) this gives a minimum uncompressed file size of $\sim 2\,\text{MB}$. For a full frame image from the iKon-L at 2048 × 2048 this value quadruples to $\sim 8\,\text{MB}$. If the raw output is processed in any way then the numerical data need to be converted to 64-bit double precision values so that negative and decimal values are handled correctly. This again quadruples the file sizes to 8 MB and 32 MB for the two frame sizes respectively.

A data set typically consists of over 100 images so upwards of several gigabytes of data can be produced by a single experiment. With modern disk storage capacities this is not as major a concern as it would once have been. Nevertheless, when one considers the possibility of producing multiple copies of each data set when processing, hard drive space can quickly be consumed.

Compression of each image will give some file size gains, but also requires additional processing which is time-consuming for large data sets. A compression ratio of $\sim 20\,\%$ is easily achieved using a basic archiving package such as *WinRAR*, but for a typical ECCD stack this operation takes several minutes. There is the possibility of including a compression scheme in the file format itself, but, considering that most data processing operations will involve the entire stack, there is not any significant benefit to this. The additional overhead becomes less of a concern when archiving the data for long-term storage where access of the data will be less frequent so is worth considering in this scenario.

3.5 Summary

In this chapter the design and development of all aspects of the XEOM1 system has been detailed. The key considerations for the microscope design have been summarised along with the simulation and evaluation of the optical system. A detailed description of all the XEOM1 components has been given, including the auxiliary control and measurement hardware. The software which has been developed for control of the instrument has been described, and the operational modes which it enables have been summarised. Finally, the data acquisition and storage challenges have been addressed.

References

[1] E Hecht. *Optics*. Addison-Wesley, 4th ed. edition, 2003.

[2] G W C Kaye and TH Laby. *Tables of Physical and Chemical Constants*. Longman, 16th edition, 1995.

[3] Lambda Research Corporation. OSLO (Optics Software for Layout and Optimization). URL http://www.lambdares.com/additional-software/oslo.

[4] W J Smith. *Modern Optical Engineering: The Design of Optical Systems*. McGraw-Hill, New York, 3rd ed. edition, 2000.

[5] Lambda Research Corporation. *OSLO Optics Reference*. Lambda Research Corporation, 2005.

[6] J A Nelder and R Mead. A simplex method for function minimization. *Comput. J.*, 1965.

[7] W Press, et al. *Numerical Recipes in C: The Art of Scientific Computing*. CUP, Cambridge, second edi edition, November 1987.

[8] Finger Lakes Instrumentation (FLI). URL http://www.flicamera.com/.

[9] A Adriaens, et al. Insights into electrolytic stabilization with weak polarization as treatment for archaeological copper objects. *Anal. Bioanal. Chem.*, 387(3):861–8, 2007.

[10] G K C Jones. *Secondary Ion Mass Spectrometry and Spectroelectrochemistry for the Study and Conservation of Ancient Metals*. Masters thesis, University of Warwick, 2007.

[11] A Adriaens, et al. An in-situ X-ray absorption spectroelectrochemistry study of the response of artificial chloride corrosion layers on copper to remedial treatment. *J. Anal. At. Spectrom.*, 24(1):62, 2009.

[12] Virtual Observatory India (VO-I). CSharpFITS Package. URL http://vo.iucaa.ernet.in/~voi/CSharpFITS.html.

Chapter 4

Experimental Testing & Development

The development of a new piece of scientific equipment is an evolutionary process. No matter how comprehensive the design brief, it is almost inevitable that there will be unforeseen difficulties or desirable features which are not discovered until the system is deployed for the first time. Consequently, the initial build is often only the first step towards the end goal of producing an instrument which meets the performance requirements and incorporates all the features necessary to carry out useful experiments. In the particular case of an imaging system, the primary figure of merit when assessing instrument performance is the quality of the images produced. There is an interplay between effects contributed by different aspects of the microscope operation which affect the overall imaging performance. Attributing these effects to the correct component in order to improve the system has been one of the most challenging aspects of this project. Of course, with a multi-component system such as XEOM1, imaging performance is only part of the story. Evolution of both the non-optics hardware and the control software continued throughout testing.

This chapter begins with an overview of the general details related to experimental setup and sample preparation. The subsequent sections detail the major avenues for development of XEOM1. While these are presented separately, much of the work on these different aspects was carried out in parallel. As a consequence, many of the experiments which were performed gave us information about more than one of these aspects. When presenting data here I try to make it clear which features are relevant to the point under discussion. Any modifications to the basic setup that were made are noted in the relevant section.

4.1 XEOM1 Setup

During its development, XEOM1 has been deployed on two different beamlines at the European Synchrotron Radiation Facility (ESRF) in Grenoble, France. In this section the characteristics of each beamline are described. The geometry of the XEOM1 setup on each beamline is also outlined along with specific hardware interface details. The choice of beamlines which have been used for this project is not arbitrary. There are specific features about each which make them suitable for this type of experiment. Both beamlines utilize a bending magnet as the X-ray source which provides some desirable characteristics: the beam footprint is relatively large (mm-scale) with a reasonably uniform flux distribution, a wide energy range can be accessed allowing a broad range of absorption edges to be excited, and the position of the beam footprint position is stable over the energy range of a typical XAFS scan. The end stations also provide suitable platforms for deploying XEOM1 (see below). Despite this, unless a beamline were to be built specifically for this type of experiment, there are always going to be compromises. It is for this reason that XEOM1 has been built with adaptability in mind.

	BM28 XMaS	**BM26A DUBBLE**
Energy range	2.5–15 keV	5–40 keV
Energy resolution $\Delta E/E$	1.7×10^{-4}	2×10^{-4}
Beam size at sample (FWHM)	0.5 × 0.5 mm	0.5 × 0.5 mm

Table 4.1: *Specifications for the beamlines at which XEOM1 has been deployed: BM28 XMaS, and BM26A DUBBLE.*

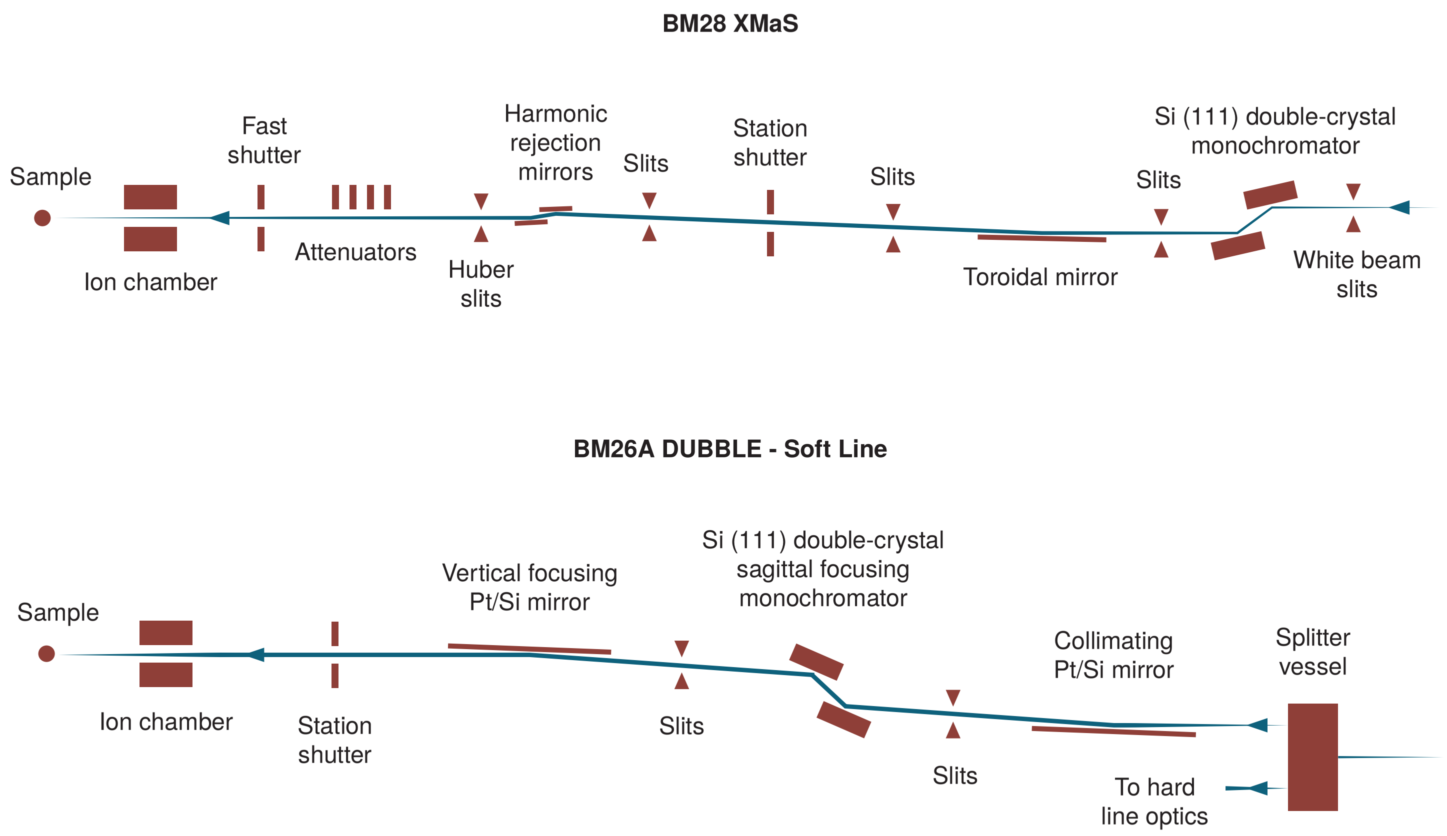

Figure 4.1: *X-ray optics on BM28 XMaS and BM26A DUBBLE. When performing scattering experiments on XMaS, the toroidal mirror is usually bent to provide lateral focusing of the beam. In order to make better use of the field of view of XEOM1 (particularly when using the larger sensor in the iKon camera), the mirror is unbent in order to defocus the beam, increasing the width of the beam footprint. Conversely, the monochromator crystal in the DUBBLE optics can be bent sagitally in order to provide lateral focusing of the normally wide (approx.* 10 mm*) spot into an area comparable with the field of view, increasing the flux density.*

4.1.1 Setup on BM28 XMaS

XMaS[1] is the UK-CRG (collaborating research groups) beamline at the ESRF. Situated on a bending magnet (BM28), XMaS is designed to perform single crystal diffraction over an energy range of 2.5 keV to 15 keV [1, 2] (Figure 4.1). This is perfect for accessing the copper K-edge energy at 8.979 keV. The experimental hutch on XMaS is equipped with an 11-axis Huber four-circle diffractometer. While it is designed for sophisticated automation of X-ray scattering experiments, it serves as an excellent mounting stage for XEOM1 (Figure 4.2). A custom bracket allows for the optical rail on which the optical column is mounted to be bolted to the top of the 'χ'[2] circle. This is rotated to the horizontal position (i.e. $\theta = 90°$)[3] in order to provide a stable platform. Rotation of the whole setup about the vertical axis (i.e. $\chi = 30°$) allows access for the X-ray beam through one of the 60° angle ports. The beamline vacuum is extended to within a few centimetres of the port entrance with Al foil being used to cover the gap.

When measuring XEOL spectra (using the CCD camera or the PM tube) it is crucial that background light is kept to an absolute minimum. While the light tightness of the optical column is a considerable improvement over that of ODXAS1, the lights in the experimental hutch were always switched off when acquiring data. In addition, the observation windows in the control hutch and the on the interlocked door were covered, as were any particularly bright sources of light inside the hutch itself, notably the computer monitors.

4.1.2 Setup on BM26A DUBBLE

The Dutch-Belgian beamline (DUBBLE) is another CRG beamline at the ESRF. Also utilizing the photons generated at a bending magnet (BM26), DUBBLE is divided into two separate branches [3] (Figure 4.1). XEOM experiments have only been carried out on the soft branch (BM26A), so this part of the beamline is described in detail. However, for the sake of completeness, a summary of the hard branch (BM26B) is also given.

---

[1] X-ray Magnetic Scattering

[2] In X-ray scattering geometry notation, χ refers to the rotation angle about the X-ray beam axis.

[3] θ is the angle between the X-ray beam and the sample surface.

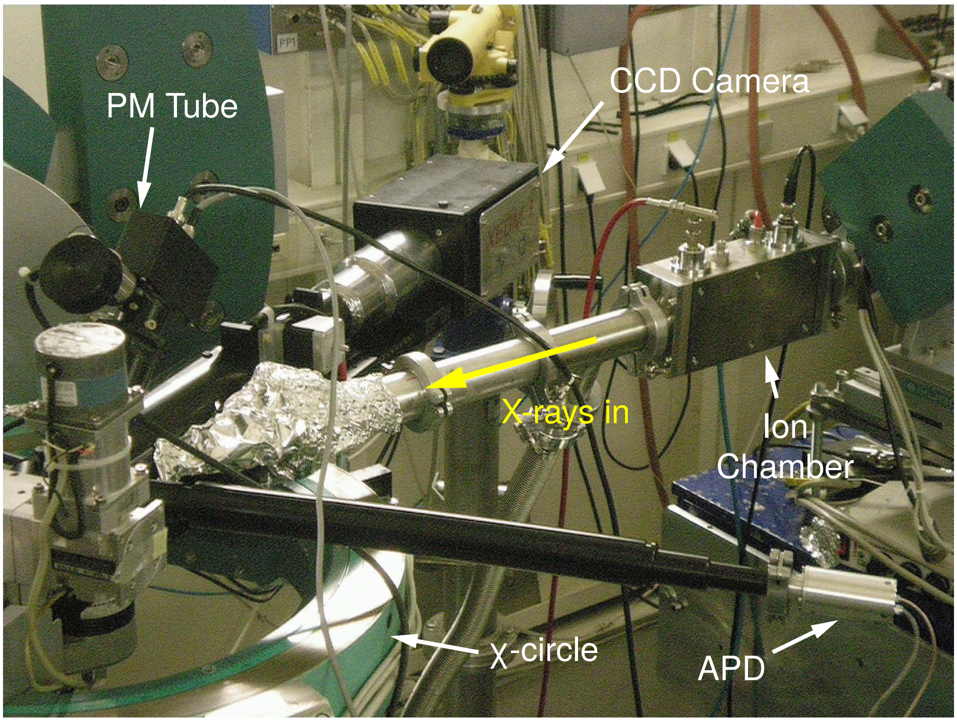

Figure 4.2: *When deployed at XMaS, XEOM1 is mounted directly to the χ-circle of the Huber diffractometer. The sample position is coincident with the eucentric point (center of rotation) of the goniometer in order that the beam remains incident on the sample if rotation is required.*

BM26A – Soft Branch

The soft branch — so called because it accepts 2 mrad from the soft side of the bending magnet ray fan — is designed primarily for XAS measurements. The natural width of the X-ray beam is several centimetres and for conventional EXAFS experiments slits are used to simply cut out the edges of the beam falling off a sample; the width of the beam is relatively unimportant, it is the height of the beam which is more critical as this affects the energy resolution. This is an unsatisfactory waste of beam flux for imaging experiments so we use the sagittal focusing capability of the monochromator to focus the beam somewhat, maximizing intensity in the field of view of XEOM1. The experimental hutch on the soft branch is equipped with an optical table so equipment can be securely positioned exactly where desired. The availability of particular pieces of mounting equipment can be variable so the exact setup of XEOM1 has changed from one beam time allocation to the next, but the description given here is of a typical arrangement.

A combination of X-Y and Z stages (one atop the other) is used for precise adjustment of the microscope position in 3 axes. A section of optical rail is mounted vertically on this stage setup. XEOM1 is affixed to the rail such that it is rotated by 90° about its optical axis (Figure 4.3). This give access for the X-ray beam through the large diameter 45° angle port. To maintain light tightness, a black PVC extension tube is fitted, via an adapter, to bring the port aperture directly against the first ion chamber exit slit. Similar measures to those taken on XMaS regarding background light suppression were also taken on DUBBLE.

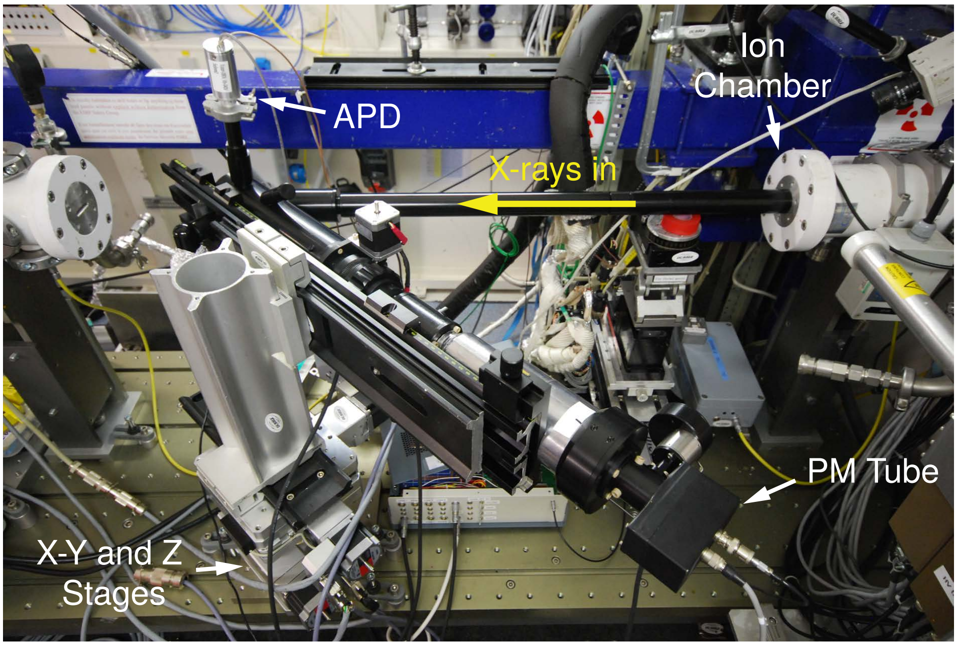

Figure 4.3: *When deployed at DUBBLE, an optical table is used to mount XEOM1. Here the PM tube is pictured in place of the CCD camera, but it is normally mounted to the* 10° *angle port protruding from below the optical column.*

BM26B – Hard Branch

The hard branch also has a 2 mrad acceptance range, but from the hard side of the bending magnet ray fan. The X-ray optics and equipment on BM26B are aimed at carrying out small-angle X-ray scattering (SAXS) [4] and wide-angle X-ray scattering (WAXS) experiments. Where XRD/WAXS is capable of giving high-resolution information about the atomic structure of materials, SAXS is aimed at revealing the shape and size of structures with typical dimensions between a few nanometres and the micron scale. A wide variety of non-crystalline objects can be probed making it extremely valuable in disciplines such as biochemistry [5], cell biology, and liquid crystal technology. In order to gain sufficient resolution, large-area detectors placed at a distance several meters from the sample, so a significant portion of the total beamline length is allocated to the experimental hutch of the hard branch.

4.1.3 Synchronization of Data Acquisition

When scanning the energy of the X-ray beam to acquire an image stack (or indeed any X-ray absorption spectrum) it is essential that the recording of detected signals is synchronized with the motion of the monochromator. If the monochromator moves while signal is being acquired the value of that data point results from a combination of signals at different energies, reducing the effective energy resolution. The notable exception to this is quick scanning EXAFS (QEXAFS) [6, 7] where the monochromator is moved quasi-continuously, but acquisition times are extremely short — typically 0.002–0.05 s.

Detectors under the control of the beamline system are usually operated via a time frame generator [8], a high-speed electronic timing module for both the control of external equipment and the synchronization of triggers. Such devices are highly configurable and allow for repetitive patterns of data acquisition. Their time resolution ($\sim 10\,\text{ns}$) even allows for synchronization to the X-ray beam characteristics arising from the electron bunch structure in the storage ring.

The ease of integrating user-supplied equipment with the beamline varies a great deal. Single-channel counting detectors, such as the PM tube, are generally the easiest to deal with as most beamlines will already use detectors of this type. All that is required is to simply plug the detector into one of the counting channels. However, integration of XEOM1 has relied on sending/receiving a trigger signal in order to synchronize its own operation with that of the beamline. On XMaS it is possible to trigger the monochromator step and counter set from the EIU, on DUBBLE it is not, so the configurations differ. Below, the specific implementations on XMaS and DUBBLE are described.

Interfacing with XMaS

Synchronizing experiments on XMaS, while conceptually simple, was initially unreliable. The basic idea is to intercept the signal from the time frame generator, which triggers the next point in a scan to begin, and replace it with our own. This is achieved by chaining an additional macro to the *spec*[4] call that initiates measurement of the counting channels i.e. acquisition of a data point. The extra macro[5] is a simple loop which forces the system to wait for an additional signal to be received from a WAGO Ethernet TCP/IP Programmable Fieldbus Controller 750-842 (WAGO Kontakttechnik GmbH & Co. KG., Minden, Germany). The ethernet signal sent from the WAGO box to initiate acquisition of the next data point is triggered by a TTL pulse from the EIU. Triggering in this manner has previously been used to synchronize acquisition of XRD images with movement of the working electrode in the eCell. The unreliability of the triggering arose from the WAGO box occasionally not detecting the trigger pulses from the EIU. A systematic investigation revealed that this was a result of the short pulse duration (< 20 ms); increasing this to 50 ms seems to have largely resolved the issue, although there is still the potential for missed triggers if the network becomes congested.

A significant advantage of this setup is that it allows for most of the scan types built into *spec* to be carried out in conjunction with XEOM1. The most common type of scan which has been used is the `Escan`, which scans the monochromator between two energies in the specified number of steps (thus defining the step size). Another useful scan type is `ascan` (`dscan`) which allows absolute (relative) scanning of an arbitrary motor. Variants of this are `a2scan`/`d2scan` and `a3scan`/`d3scan` which scan two or three motors simultaneously. Finally, `timescan`, which simply triggers the detectors has been useful for testing.

Interfacing with DUBBLE

On DUBBLE, the synchronization is more straightforward. Rather than sending a triggering pulse to the beamline system, it is the EIU which receives a signal. Specifically, it interfaces directly with the time frame generator output so that

---

[4] *spec* is a Unix-based software package widely used at synchrotron radiation facilities for instrument control and data acquisition.

[5] The wait loop macro and the commands used to chain it can be found in Appendix A.

it receives the same signal used to gate the other beamline detectors. When an experiment is started in eCell Controller, this input is continuously polled until a high signal is detected, at which time the next data point is acquired and processed. Our own detection of the triggering signal has been far more reliable than the network-based system on XMaS. There is no intermediate processing or translation of the signal and, consequently, no chance for the signal to be routed incorrectly or missed. A minor drawback to this method is that the scan modes on DUBBLE have no provision for setting a wait period between each point i.e. there is no way to allow for the readout/download overhead in each image acquisition. To compensate, the counting time on the beamline must be extended to cover this period so data from the secondary detectors are acquired over a slightly longer interval than the primary images. However, normalisation of the secondary data points to the primary image data simply requires multiplying each point by a constant of proportionality.

4.2 Samples

When developing protection systems for cultural heritage it is not usually possible to carry out testing on real artefacts. Such objects are often unique and can be extremely valuable so great care is taken when handling them to prevent any damage. Clearly, any chemical coatings should not be applied to an artefact until the interactions between the coating and the corrosion products are well understood, and one should be confident that it will have a positive impact.

Therefore, instead of using real artefacts for testing, artificially corroded analogues are used. Producing these analogues presents a significant challenge in itself. In order to gain an understanding of the chemistry it is often beneficial to deal with a simple system, limiting the number of possible interactions. In reality though, corrosion layers on heritage artefacts are often extremely complex as chemical processes have been occurring over tens, hundreds, or even thousands of years. Therefore, it is also important to ensure that the protocols which are used to produce artificial corrosion layers give results which are representative of real corrosion.

4.2.1 Copper Coupons

The Warwick/Ghent collaboration has recently been been using 12.5 mm circular metallic coupons as its standard substrate for artificial corrosion. The coupons are designed to fit into the Mk IV detachable working electrode for the eCell. The coupons which have been used for testing XEOM1 are made from commercially available copper (Advent, purity 99.9 %) with the top-facing surface of the coupon prepared using conventional metallurgical techniques. The surface is ground using 1200-grit SiC paper and then polished on cloth covered with 1 μm alumina powder. Any adherent Al_2O_3 particles are removed from the coupons by rinsing with deionized water, immersing them in a propan-2-ol ultrasonic bath for 15 min followed by a final rinse with propan-2-ol. Corrosion protocols [9, 10] (see Section 4.2.3 below) are then applied to obtain an artificially patinated or corroded[6] surface.

4.2.2 TEM Meshes

Inspecting the performance of an optical system is most easily achieved by imaging a well-defined geometrical shape or pattern. This required the production of XEOL emitting regions of known shape and dimensions within the field of view of XEOM1. To this end, copper transmission electron microscopy (TEM) grids were used as substrates for the application of corrosion protocols. Conventionally used to support samples being imaged by TEM, the grids are a standard shape and size (circular, 3.05 mm diameter) with an inner meshed area of ~ 2.5 mm diameter. The grids used with XEOM1 are 200 mesh (200 lines/inch) with 100 μm^2 holes and 27 μm wide bars. When studying a single TEM mesh the grid holder (Section 3.2.1) was sometimes used, but in order to provide additional chemical contrast many grids have been mounted at the centre of a copper coupon (bare or corroded). A dab of silver conductive paint (RS) — normally used for mounting scanning electron microscopy (SEM) specimens onto a stub — is used as an adhesive and is applied to two points around the edge of the

---

[6] A patina (like malachite - basically a copper hydroxycarbonate) is passivating and protects the surface, whilst imparting an aesthetically desirable appearance. Corrosion (like nantokite) does not protect; indeed, it creates surface conditions (e.g. pitting) and chemical reactions (release of HCl) which can promote further corrosion.

grid.

4.2.3 Corrosion Protocols

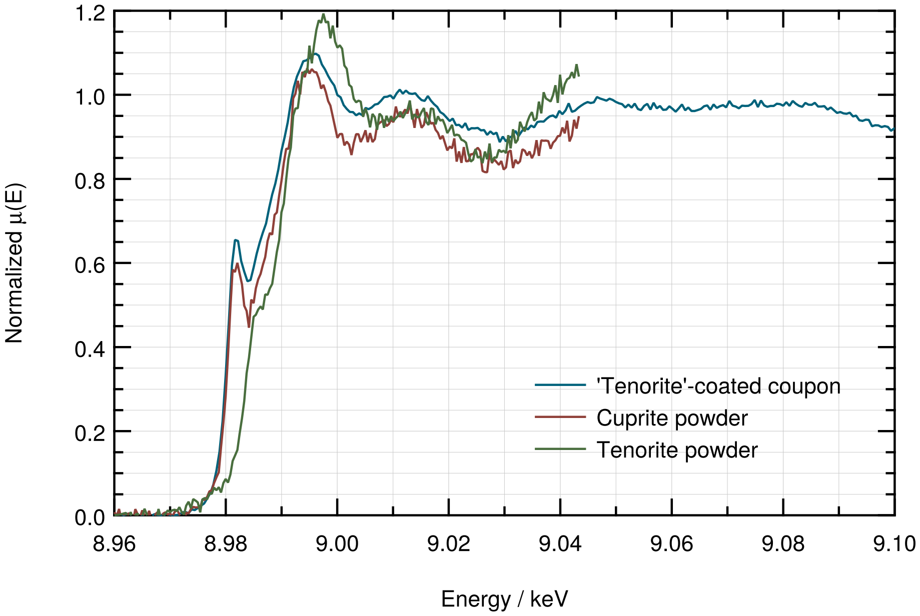

Figure 4.4: *XEOL-XANES spectra of 'tenorite'-coated copper coupon, cuprite powder and tenorite powder.*[7] *The pre-edge resonance and edge shift observed in the coupon spectrum match those of the cuprite spectrum, confirming the true identity of the corrosion product.*

Cuprite (Cu_2O) is commonly found on copper artefacts and is a stable corrosion product. A cuprite layer is produced on a coupon by anodic polarization to 320 mV (vs. a normal hydrogen electrode) for 16 h in a 0.1 M Na_2SO_4 solution (Fluka, $> 99\,\%$). However, this protocol has been found to be impractical when attempting to apply it to a grid. The major difficulty is in making an electrical connection to the grid itself, primarily a result of its fragility; the grid thickness is only $\sim 20\,\mu$m so must be handled with extreme care. Attempts to attach a thin wire resulted in a poor connection and XAS measurements have shown that no significant corrosion occurs. A more successful approach has been to produce cuprite by heating in an oxidizing flame. The grid is placed on a copper coupon and both are then held the flame until they become red hot (a few seconds). The grid and coupon are removed from the flame whereupon the grid turns black.

By contrast, the electrochemically deposited layer on the coupons is a dull red colour. Based on the coloration, it was initially assumed that the black layer was *tenorite* (CuO), but the literature [11, 12] has shown that cuprite patination can appear black depending on impurities or non-stoichiometry, and XAS analysis (Figure 4.4) again confirms that both corrosion products are unmistakably cuprite. Spectra of the 'tenorite'-coated copper coupon, cuprite powder (Fluka) and tenorite powder (Prolabo) were acquired using XEOM1 with the PM tube in the primary detector position. The distinctive pre-edge resonance which is characteristic of cuprite is observed in the coupon spectrum. Additionally, the tenorite powder reference exhibits a larger edge shift — a result of its higher oxidation state (Section 2.2.3) — when compared with the coupon; by contrast, the edge shift of the cuprite powder reference matches exactly.

Nantokite (CuCl) is one of the primary active corrosion agents on copper and its presence can compromise the long-term stability of an object. 'Bronze disease' is usually attributed to nantokite [13]. To produce a layer of nantokite on copper, the coupon is immersed for 24 h in a 1 M solution of CuCl (Aldrich, $> 99\,\%$) in deionized water, followed by further rinses with deionized water and ethanol. Finally, the sample is heated to 105 °C for 1 h. Previous measurements [14] of the average corrosion layer thickness have found them to be 0.6–1.5 μm for cuprite and nantokite produced using these protocols. With an X-ray attenuation length of at least several microns at energies close to the Cu K-edge, XAS measured by fluorescence is dominated by the bulk copper signal, but XEOL-XANES spectra are characteristic of the surface corrosion layers.

4.3 Synchrotron Data Analysis

Synchrotron data acquired using XEOM1 are a mix of images and spectra so a set of tools for analysing both of these is required. The primary software package which has been used for this task is *esaProject*, a multi-purpose image and spectrum processing tool developed by Dowsett [15]. Initially developed for analysis of XRD data with specialized tools for handling patterns acquired using an area detector, the functionality has gradually been extended to include features for reading and processing X-ray absorption spectra. For the XEOM1 project, *esaPro-*

---

[7] Data from 2010 12 DUBBLE — *'r85463.dat', 'r85465.dat' & 'r85466.dat'*

ject has been further enhanced by the addition of image processing capabilities. The data system for XEOM control and the ECCD image file format developed by the author of this thesis are designed to be complementary to *esaProject*.

4.3.1 esaProject

Images acquired by XEOM1 stored in the pre-processed state described in Section 3.3.5. Whether preparing XEOM images for visual presentation or performing more detailed quantitative analysis, almost all further processing continues by importing the data into *esaProject*. The ECCD file handling capability of *esaProject* (Figure 4.5) was developed alongside XEOM1 itself, with additional capabilities being incorporated as the data processing needs became more clearly defined.

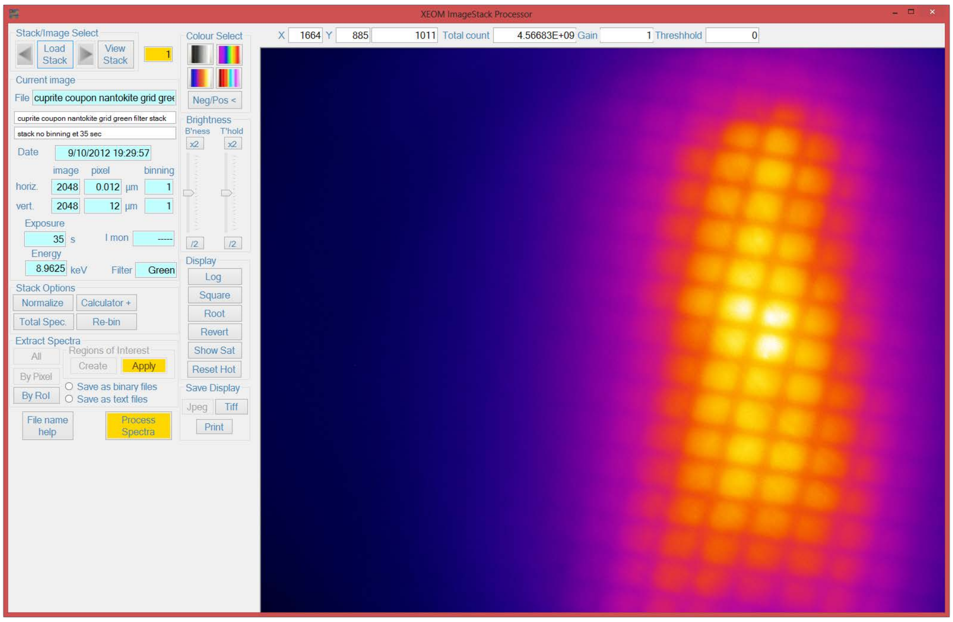
XEOM ImageStack Processor

X 1664 Y 885 1011 Total count 4.56683E+09 Gain 1 Threshhold 0

File cuprite coupon nantokite grid gree

cuprite coupon nantokite grid green filter stack

stack no binning et 35 sec

Date 9/10/2012 19:29:57

	image	pixel		binning
horiz.	2048	0.012	µm	1
vert.	2048	12	µm	1

Exposure 35 s

I mon -----

Energy 8.9625 keV

Filter Green

Figure 4.5: *Screenshot of the* esaProject *XEOM Image Stack Processor window. Controls for loading and manipulating image data, in addition to the image metadata, are displayed on the left. The ECCD image loaded in the right portion of the window is being displayed with an 'ironbow' colour palette applied.*

In its current state of development, images can be imported individually or as part of a complete stack and are displayed in the main window one at a time. Metadata stored in the header of each ECCD file is displayed, and it is possible to cycle through the images sequentially or skip to a particular image in the currently loaded stack. A number of false colour palettes can be applied which map to the intensity values stored in each pixel. In order to enhance the visual appearance of the images and to highlight particular features to aid interpretation, the colour display can be manipulated in a variety of ways. The *brightness* and *threshold* controls modify the mapping of the colour spectra by changing the range of intensity values over which the map applies or by shifting it up and down the intensity scale. Additionally, a number of mathematical operations — raising to a power, taking a root, taking the log — can be applied to the underlying data in order to modify the image appearance for a particular colour map. When used for display purposes, these operations do not permanently affect the underlying data, but an ‘image calculator’ is also provided to allow for permanent modification of the data. Simple operations such as addition and multiplication by a constant are applied on a pixel-by-pixel basis, and the display operations mentioned above are also available. Operations involving multiple images are also possible: addition of several images, subtraction of one image from another, multiplication and division of images etc. These allow for image processing such as those discussed in Section 3.3.5 to be performed, and the automatic application of common pre-processing tasks is built into the calculator.

Other common tasks include normalization and pixel-by-pixel integration of the intensity over an entire image in order to extract the total XEOL spectrum from an image set i.e. a 1D spectrum with no spatial resolution. In XAFS measurements, the measured signal is conventionally normalized via division by another signal representative of the incident X-ray beam intensity in order to correct for fluctuations introduced by a number of sources: fluctuations in the storage ring orbit, the decay of storage ring current over time, and monochromator glitches [16]. On both XMaS and DUBBLE an ion chamber placed immediately before the sample provides the monitor signal which is stored by the data acquisition system on each beamline; *esaProject* is capable of reading these files and extracting the relevant data i.e. the beam monitor signal, so that normalisation of an entire stack can be done automatically. This process assumes that the measured signal is linear with the incident X-ray intensity; this is true for transmission and fluorescence measurements, but is not necessarily the case for

XEOL measurements due to the decoupled nature of the absorption and emission processes (discussed previously in Section 2.3) and can potentially lead to unwanted distortions in the final spectrum. However, no detrimental effects on the data acquired using XEOM1 resulting from normalization have yet been observed so all such data presented here have been normalized.

Finally, the most powerful image processing feature offered by *esaProject* is the capability to define a sub-region within an image and extract the signal integrated over the corresponding area from each other image in the stack. The resulting spectrum is representative of the XEOL emission emanating from this region only. In other words, it provides the capability to examine the XEOL emission from different *regions of interest* (ROIs) within the field of view of XEOM1, allowing the spatial variation in surface chemistry to be analysed. This is the primary feature which enables the full potential of XEOM1 to be reached. Defined ROIs have six possible shapes: rectangle, rotated rectangle, ellipse, triangle, line, and point. These primitives can be combined and overlapped to form an ROI of almost any shape. Moreover, ROIs are not required to form a single continuous region. Multiple defined areas can form a single ROI, and many ROIs can be defined for a single image stack. Following the designation of ROIs, the intensity within the corresponding regions in each image is integrated and a series of spectrum files are produced: one for each defined ROI and a final one for the remaining region (if any) outside the designated ROIs. Further processing can be done within the spectrum processing portion of *esaProject*, or the files can be imported into another program for further data reduction.

4.3.2 Athena

XEOL spectrum data has received additional treatment using *Athena* (mentioned in Section 2.2.2). As will be seen, the primary focus has been on collection of data in the XANES region of the absorption spectrum; the time currently required to acquire an image stack covering the full EXAFS region is prohibitive. As such, full refinement of structural parameters using a combination of *Athena* and *Artemis* is not possible. However, *Athena* itself provides some capabilities which are still useful for presentation of XANES data. The core level absorption observed in a measured spectrum sits on top of the absorption from previous edges. In order to remove this contribution (and any instrumental background) a spline is fitted to the pre-edge region of the spectrum and is subtracted from the data set (Figure 4.6). A further spline is fitted to the post-edge region which is used to normalise $\mu(E)$ between 0 and 1 (and determine the change in absorption at the edge step $\Delta\mu(E_0)$ in the full treatment). If the oscillations in the vicinity of the edge are large in amplitude and if the energy range of data points collected beyond the edge is small (compared with the typical range for a full EXAFS scan of several hundred electronvolts), the latter may not be an accurate representation of the post-edge trend and some distortion can occur.

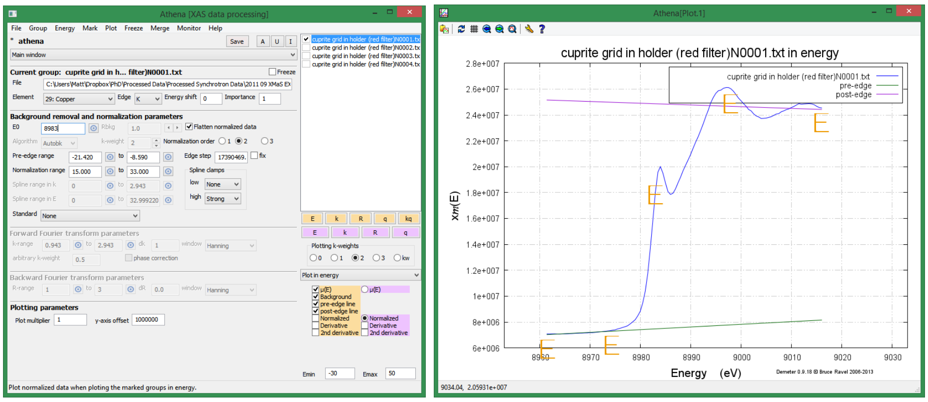

Current group: cuprite grid in h... filter)N0001.txt ☐ Freeze
File C:\Users\Matt\Dropbox\PhD\Processed Data\Processed Synchrotron Data\2011 09 XMaS Ex
Element 29: Copper Edge K Energy shift 0 Importance 1

Background removal and normalization parameters
E0 8983 Rbkg 1.0 ☑ Flatten normalized data
Algorithm Autobk k-weight 2 Normalization order ○ 1 ● 2 ○ 3
Pre-edge range -21.420 to -8.590 Edge step 17390469. ☐ fix
Normalization range 15.000 to 33.000
Spline range in k 0 to 2.943
Spline range in E 0 to 32.999220
Spline clamps low None high Strong
Standard None

Forward Fourier transform parameters
k-range 0.943 to 2.943 dk 1 window Hanning
arbitrary k-weight 0.5 ☐ phase correction

Backward Fourier transform parameters
R-range 1 to 3 dR 0.0 window Hanning

Plotting parameters
Plot multiplier 1 y-axis offset 1000000

Plotting k-weights ○ 0 ○ 1 ● 2 ○ 3 ○ kw
Plot in energy
☑ μ(E) ○ μ(E)
☑ Background
☑ pre-edge line
☑ post-edge line
☐ Normalized ● Normalized
☐ Derivative ☐ Derivative
☐ 2nd derivative ☐ 2nd derivative
Emin -30 Emax 50

Plot normalized data when ploting the marked groups in energy.

9034.04, 2.05931e+007

Figure 4.6: *Screenshots of the Athena main window and plotting view. Left: in the main window a number of different views for manipulation and analysis of the data can be selected, including those for normalization, calibration to a reference spectrum, alignment, deglitching etc. Right: the plotting window allows the spectra to be represented in energy-space, k-space, and real space. Here, the normalization of the extracted XEOL spectrum plotted in Figure 4.18 is shown, including the pre- and post-edge splines.*

For the purposes of determining the position and amplitude of the XANES oscillations, which is used for chemical identification here, this treatment is usually sufficient. However, when applied to XEOL-XANES data, there are some additional complications. Adriaens et al. [17] have shown that subtraction of the pre-edge background can be inappropriate in some cases. If excitation of the emission channels generating the pre-edge background continues as the X-ray energy moves over the absorption edge the edge step and XANES oscillations will sit on top of this signal; for the samples being studied here this would be most likely if there is a non-copper-based constituent in the corrosion product or some other surface contaminant. However, if emitters that generate the pre-edge signal turn off at the edge and are replaced by a set of radiative channels with differing optical yields the relative height of the edge step will change (see Section 2.3.2). Therefore, subtracting the pre-edge background will modify the gradient of the edge and shift the relative position of any features on the edge. A potential strategy for handling this situation is discussed in Section 5.5.

4.4 Assessment of Microscope Characteristics

4.4.1 First XEOM1 Images

Figure 4.7: *This image of the emission from an illuminated filament lamp among the first acquired using the completed XEOM optics and detector.*[8]*It is possible to distinguish the filament coils themselves and one of the filament support structures within the bulb (the dark shadow across the coils).*

When the XEOM optical column and lens components were assembled for the first time, many other components in the system were still under development. The image acquisition software was still relatively crude and only capable of capturing single images, and no sample stage had yet been constructed. Nevertheless, it was still possible to capture the first image on the test bench. The filament lamp which is usually used as a sample illuminator (see Section 3.2.3) served as the object for the initial test. One of the test images is shown in Figure 4.7 — the filament coil is clearly visible, demonstrating that the optics are capable of successfully forming an image. However, close inspection also reveals that some arc-shaped artefacts are also present; these will be discussed in Section 4.4.2 below.

---

[8] Image source: *'filament001.tif'*

The first deployment of XEOM1 at a synchrotron facility was on the DUBBLE beamline in December 2010. This beam time allocation was dedicated solely to testing of XEOM1 and was the first attempt at acquiring XEOL images. Alignment of the X-ray beam to the area of the sample within the field of view of XEOM1 was done by first affixing a piece of fluorescent paper, which emits strongly in the visible under X-ray bombardment, to a sample stub and monitoring this with a closed-circuit camera directed down one of the angle ports. Green fluorescence from the paper is clearly visible on the monitor. Precise alignment of the XEOM1 field-of-view over the beam footprint could then be done by imaging the fluorescent emission using the CCD camera (Figure 4.8). Motion of the stages on which XEOM1 is mounted enables the illumination region to be positioned completely within view, maximizing the visible secondary emission. A bare copper TEM grid was glued onto the paper with silver conductive paint which generates a 'shadow' of the mesh enabling an approximate focus to be obtained. This has subsequently been used as the standard sample for alignment of the system on both DUBBLE and XMaS.

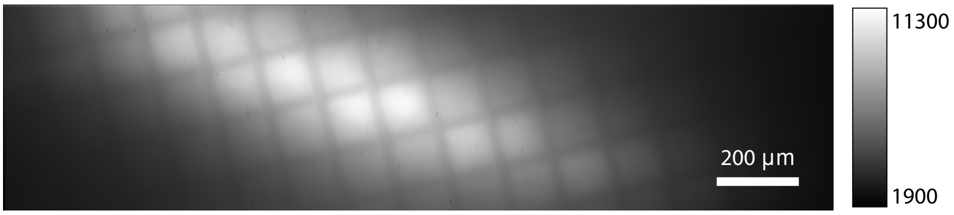

Figure 4.8: *Imaging the visible emission from X-ray fluorescent paper enables the beam footprint to be positioned within the field of view. A rough focus can be achieved by imaging the shadow of a TEM grid affixed to the centre of the paper.*[9]

The first true XEOM image was also acquired during this beam time allocation. Initial attempts were made to image a bare copper TEM mesh, and one coated in atacamite (a copper hydroxychloride $Cu_2Cl(OH)_3$), but we were unable to acquire an image from these samples. This result is slightly puzzling as previous measurements using ODXAS1 have had no difficulty in obtaining XEOL signals from either copper or atacamite. It was not until the sample was changed to a cuprite-coated mesh — thought to be tenorite-coated at the time (Section 4.2.3) — that a XEOM image of the grid (Figure 4.9) became discernible. In

---

[9] Image from 2010 12 DUBBLE — *'Align 1002.eccd'*

subsequent experiments it has been found that cuprite is the most reliable compound of those tested for obtaining XEOM images. The image was acquired with an input X-ray energy of 8.997 keV with an exposure time of 12 s. The peak measured intensity on a pixel was ~ 37000, greater than half of the dynamic range of the camera; however, it should be borne in mind that the initial images were acquired using unfiltered XEOL emission so such an image would not be suitable for chemical mapping applications.

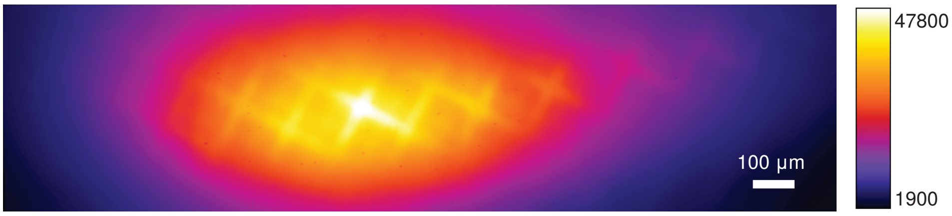

Figure 4.9: *A cuprite-coated copper TEM grid was the first sample from which a XEOM image was acquired.*[10]*It was later discovered that the protocol used to produce this sample actually produced a layer of cuprite, as discussed previously (Section 4.2.3).*

4.4.2 Sensor Defects

During initial testing of the imaging system, before XEOM1 had even been deployed at a synchrotron beamline, it became apparent that some unusual features were present in some images. Specifically, many images were found to contain a series of bright ‘arcs’ (see Figure 4.10) which do not correspond to any physical features on the object or illumination source being imaged. The appearance of these arcs is particularly troubling as they are discernible in XEOL data images. Two characteristics indicate that they are not caused by some internal process in the sensor itself:

1. They are not present if there is no source of illumination, or the shutter is closed i.e. in dark frames.
2. Their position and sharpness is dependent on the illumination characteristics.

---

[10] Image from 2010 12 DUBBLE — *‘TenoriteMesh12s000.eccd’*

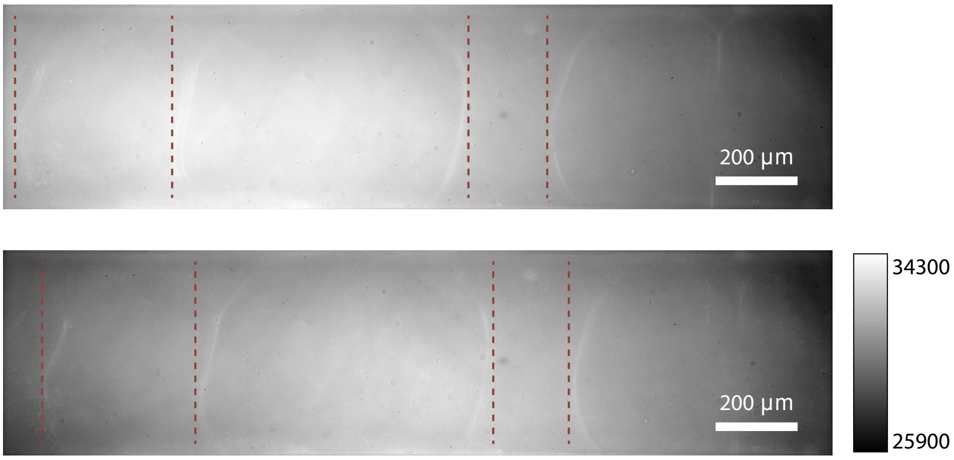

Figure 4.10: *Test images which demonstrate the artefacts observed in the FLI camera images.*[11]*These were produced by illuminating the optical system using a small filament lamp. Equivalent arc features are highlighted by the dotted lines. As the position of the lamp is changed, the artefacts shift so flat-field correction would not be sufficient to eliminate the problem.*

The first option to be considered was the possibility of light being reflected or scattered by the internal walls of the optical column. The aperture stop (the limits of the first lens in the XEOM1 optical system) defines the cone of light rays which will pass directly through all the subsequent lenses and reach the sensor directly. However, despite the light absorbing properties of the black acetal plastic from which the column is constructed, it is still conceivable that light entering the system from outside this cone could still reach the sensor. The first test to be carried out in order to rule out this possibility was to insert a field stop into the optical column. Whereas the aperture stop determines the brightness of the image, a field stop determines the field of view of the system if the resulting image is smaller than the sensor size — if this is the case, the image is said to be *vignetted*. However, inserting a field stop with the same diameter as the primary ray bundle will still allow the full image to be formed, but any stray light that could be scattered into the sensor will be blocked i.e. it acts as a light baffle. This is most effective if placed between the final lens and the sensor, but when this test was carried out it was found that it had no impact on reducing the arcs. A further possibility was that of specular reflections from the

---

[11] Image from 'Reflection and dust testing' — *'test001.eccd'* and *'test002.eccd'*

machined finish of the plastic surface. This was ruled out by a further test in which a tube of matte black flock paper was used to dull the inner surface of the final section of the optical column. Again, no suppression of the image artefacts was observed.

It was noted during the investigations into this problem that the surface of the CCD sensor in the FLI camera does not appear to be completely uniform. When viewed from an oblique angle, it can be noticed that the image produced by reflection of external light from the surface is distorted. The nature of the distortion suggests that the surface is not flat, as would be expected, but that the surface is ‘rippled’. Closer inspection of the ripples indicates that there is indeed a correlation between these and the image artefacts (illustrated in Figure 4.11). It is proposed that the surface of the sensor is slightly reflective (there is no anti-reflection coating) and the local curvature acts as a concave mirror which has a focal length approximately equal to twice the distance between the sensor and the inside face of the fused silica camera window. Consequently, the reflected light is focused back onto the CCD and the width of the image artefacts depends on the angular aperture of the source.

An additional unwanted feature which was apparent from fairly early on was a distribution of small dark circles across some images, also visible in Figure 4.10. As with the bright arcs, these are only apparent in situations where light is incident upon the sensor, and their positions also vary (although to a much lesser degree) depending on the illumination characteristics. These have been attributed to a build up of particulate matter on the surface of the sensor which appears to have increased in severity as the camera has continued to be in use. Considering that the front compartment of the camera is hermetically sealed, argon filled, and contains desiccant — these measures are intended to prevent the ingress of dust particles and water vapour (which would condense on the surface of the sensor when cooled) — this casts further doubt over the build quality of the camera.

4.4.3 Selection of the Large-area Sensor Camera

While it was always intended that the MicroLine ML1109 be replaced by a camera fitted with a large-area sensor, the requirements for the new device changed

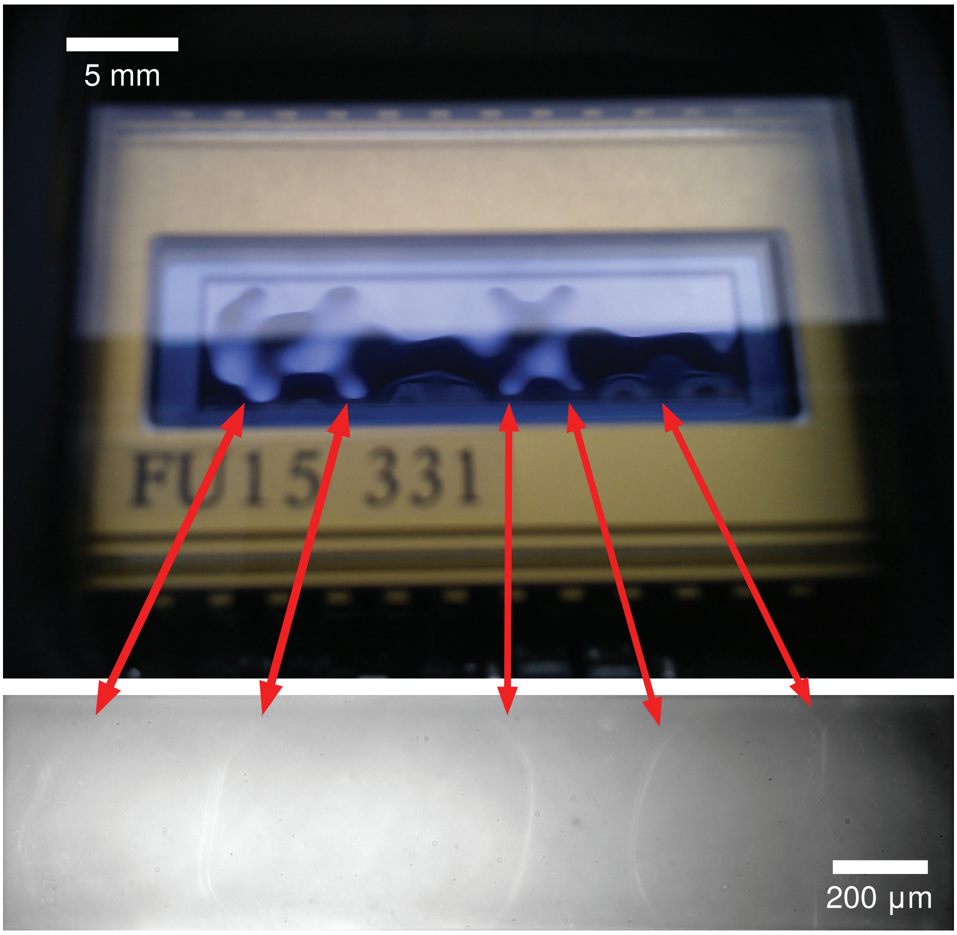

Figure 4.11: *Upon visual inspection, imperfections in the surface of the CCD sensor are clearly visible. Comparison of the imperfection geometry with a test image (same as Figure 4.10 [top]) shows a clear correspondence between the surface 'ripples' and the bright arcs.*

somewhat as a result of the problems previously described. The original candidate was another FLI MicroLine camera, the ML3041. With the same body as the ML1109 it possesses the same advantages in compactness and weight. Additionally, no changes would need to be made to the software to integrate this camera as all FLI cameras use the same SDK. However, despite the obvious advantages, the difficulties experienced in dealing with FLI and their hardware forced the consideration of alternative cameras — the Andor iKon-L 936 and the Apogee Alta F42-UV (specifications for all three cameras are given in Table 4.2).

Primary targets for the sensor in the new camera were a resolution of 2048 × 2048 with a comparable pixel density to the Hamamatsu S10140-1009

	FLI Microline ML3041	**Andor iKon-L 936**	**Apogee Alta F42-UV**
Sensor	Fairchild Imaging CCD 3041	e2v CCD42-40 NIMO	e2v CCD42-40 NIMO
Array size	2048 × 2048	2048 × 2048	
Pixel size	15 µm	13.5 µm	
Full well capacity (minimum)	85 000 e^-	100 000 e^-	
Typical dark current	0.3 e^- pixel^{-1} s^{-1} @ −40 °C	0.4 e^- pixel^{-1} s^{-1} @ −70 °C	
Sensor dimensions	30.72 × 30.72 mm	27.6 × 27.6 mm	
Digitization speed (maximum)	3 MHz	5 MHz	4 MHz
Typical system noise	9 e^- (maximum) @ 1 MHz	31.5 e^- RMS @ 5 MHz	10–12 e^- RMS @ 1 MHz
Typical maximum cooling (below ambient - air cooling only)	−55 °C	−90 °C	−65 °C
Linearity	> 99 %	> 99 %	–

Table 4.2: *Comparison of CCD camera candidate specifications. While the Andor iKon-L 936 and Apogee Alta F42-UV are fitted with the same sensor, the Andor exhibits better thermal noise performance due to its 4/5-stage thermoelectric cooling.*

i.e. quadrupling the active area of the CCD, and increasing the field-of-view of the microscope by the same factor to $\sim 2 \times 2$ mm. While it is not possible to adjust the X-ray optics on XMaS or DUBBLE to take full advantage of the extra viewing area — the area from which signal is measured is still limited by the beam footprint — it would still be beneficial if XEOM1 were to be deployed on a beamlime where an even larger footprint is achievable. Moreover, the larger field-of-view aids in alignment of the sample to the beam as the largest footprint achievable on both XMaS and DUBBLE has a large aspect ratio. This necessitates a reasonable degree of rotational alignment to avoid cropping the image with the rectangular sensor, a condition which is relaxed considerably by using a square one.

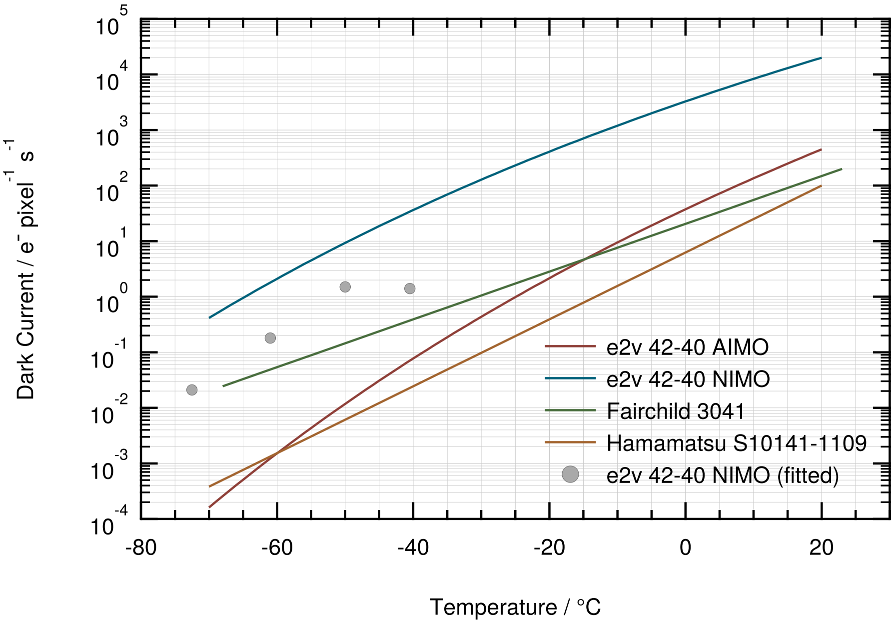

Figure 4.12: *Estimates of dark current behaviour have been made using the following: (a)* $Q_d/Q_{d0} = 122T^3\mathrm{e}^{-6400/T}$ *and* $Q_d/Q_{d0} = 1.14 \times 10^6 T^3 e^{-9080/T}$ *for the e2V NIMO and AIMO sensors respectively, where* Q_d *is the dark current at temperature* T [K] *and* Q_{d0} *is the dark current at* 293 K *(formulae taken from manufacturer-provided data sheets); (b) the manufacturer's assertion that the dark current doubles every* 5 °C *for the Hamamatsu S10141-1109 and every* 7 °C *for the Fairchild 3041. The dark current values for the actual sensor fitted are taken from the calibration documentation provided by Andor.*

An additional concern was the level of thermal noise exhibited by each camera. The overall thermal noise performance (summarized in Table 4.2 for the three candidate replacement cameras, plus the original ML1109) is dependent on both the rate of generation of thermal electrons in the sensor, and the ability of the cooling system to suppress this. The rate is limited in the Microline ML1109 by the performance of its thermoelectric cooler which can only achieve a maximum cooling of 65 °C below ambient — practically, this results in an operating temperature of approximately −40 °C at room temperature. Despite this, the overall performance is good due to the low level of thermal noise inherent to the Hamamatsu sensor itself. The standard sensor fitted in iKon-L camera is a back-illuminated CCD42-40 AIMO (e2v technologies (UK) Ltd., Chelmsford, UK) which offers better dark current suppression than the NIMO option. However, the AIMO sensor is not available with the UV-enhanced coating which is desirable in order to take full advantage of the optics bandwidth. Despite being fitted with the same sensor, the thermal noise performance of the Apogee camera is not as good since its compact cooling system is not as effective as that of the iKon-L which was ultimately selected. As can be seen in Figure 4.12, the performance of the particular sensor and cooling combination fitted to the camera which was received is actually better than expected, and is comparable with that of the sensor in the ML1109.

4.5 Filtered Imaging and Focusing

As mentioned in Section 3.1, the deliberate choice to use a single glass type has resulted in an inherently chromatic optical system. Testing has shown that reasonable images are still obtainable when the optical emission is unfiltered, but filtering is essential for them to be useful for chemical analysis. However, a consequence of filtering the XEOL emission is a significant reduction in photon flux reaching the detector. The effect of this is two-fold: the formation of images takes longer (slow experiments), and the total signal in XEOL spectra is lower (poor statistics). Clearly there is a trade-off to be made, although without good statistics the data will be of questionable value so overcoming the latter is ultimately the priority.

Increasing the counting time in order to improve the signal level — and reduce the statistical uncertainty as a consequence — can drastically extend the total experiment time. For example, a 112 point experiment carried out with

100 s exposures will take over three hours. The possibility of monitoring fast chemical processes is ruled out if acquisition times of this order are required, although time-lapse measurements would still be possible for more slowly progressing changes. Additionally, an allowance for extra time between image acquisitions must be made to accommodate the downloading and processing of each image. Moreover, the sensor readout noise increases for faster readout speeds so a slow readout is generally desirable from this point of view. The digitization speed of the Microline camera is fixed at 500 kHz, but on the Andor camera it can be varied between 50 kHz and 5 MHz. Clearly the faster rate will result in quicker readout times, but the reduction in noise from using the slowest rate is approximately a factor of 10 — an improvement in the signal by a factor of 100 from Poisson statistics. However, at 50 kHz the total readout time is nearly 100 s, far too slow for this application. Therefore, the images here have been acquired using a 3 MHz rate (less than 2 s per image). Binning, described in Section 3.3.2, has also been used to reduce the acquisition time when the signal level has been low. While this results in a loss of ultimate resolution, imaging at say 4×4 binning does not significantly degrade the mesh images, and further increases the signal quality by virtue of reducing the required exposure time and, consequently, the build-up of thermal signal. Binning also reduces the image readout time, so there is scope to further optimize the combination of digitization rate and binning for different signal levels in the future.

If it takes more than a few seconds to acquire an image, focusing the microscope becomes a challenging (and tedious) prospect. In its current state, the software is not sophisticated enough to automatically find the best focus. The current procedure is to continuously acquire images while scanning the focusing lens across its range while assessing each image by eye and judging when the best focus has been reached. The focus lens moves at a fixed speed so this only works if the acquisition time is short. If a longer exposure is required, the lens moves too far during each acquisition to determine to focal position; in this case, the lens must be stepped manually at short intervals between each image acquisition. Of course, the subjective nature of assessing image focus also poses a significant challenge, especially if the image is faint or if the contrast is low.

4.5.1 Dichroic Filters

The initial filters used in conjunction with XEOM1 were a set of Edmund Optics dichroic filters (Table 4.3). These have previously been used to gather colour filtered XEOL spectra using ODXAS1. The complete collection is made up of three additive filters (red, green, blue), three subtractive filters (cyan, magenta, yellow), and a pair of short/longpass filters. These particular filters were originally selected as the range of pass bands is sufficient to cover most of the useful range of the Hamamatsu PM tube used in ODXAS1 since this is only sensitive up to just over 800 nm. Given the chromatic nature of the XEOM1 optics, filters with multiple pass-bands (subtractive filters) or a very wide pass-band (long/shortpass filters) are of questionable value for imaging as light from only one band will form a focused image; light passing through other bands will only contribute to an unfocused background. Consequently, measurements have primarily been carried out using the RGB filters.

	Pass band (nm)	**Bandwidth** (nm)	**Centre wavelength** (nm)
Blue (52-531)	400–500	100	450
Green (52-534)	500–575	75	537
Red (52-528)	600–750	150	675
Cyan (52-537)	400–600	200	500
Magenta (52-540)	400–500/600–700	100/100	450/650
Yellow (52-543)	500–700	200	600

Table 4.3: *Manufacturer specifications for the Edmund Optics dichroic filters.*

4.5.2 Filtered Imaging Characteristics

When attempting to find a focus using the method described above, it was often found that several lens positions would produce a focused image with poorer focusing elsewhere. This behaviour is to be expected if no filter is placed in the optical column; broadband emission would likely produce a focus over a wide range of lens positions (although the contrast would probably be low), and a sample emitting only in narrow bands would allow a focus to be found at a number of more well-defined positions. However, once the light is filtered a focus should only be found about the range in lens position corresponding to the pass band of the filter. The presence of multiple foci in this case suggests that the filter has more than one pass band, likely outside the range over which the manufacturer gives its specifications.

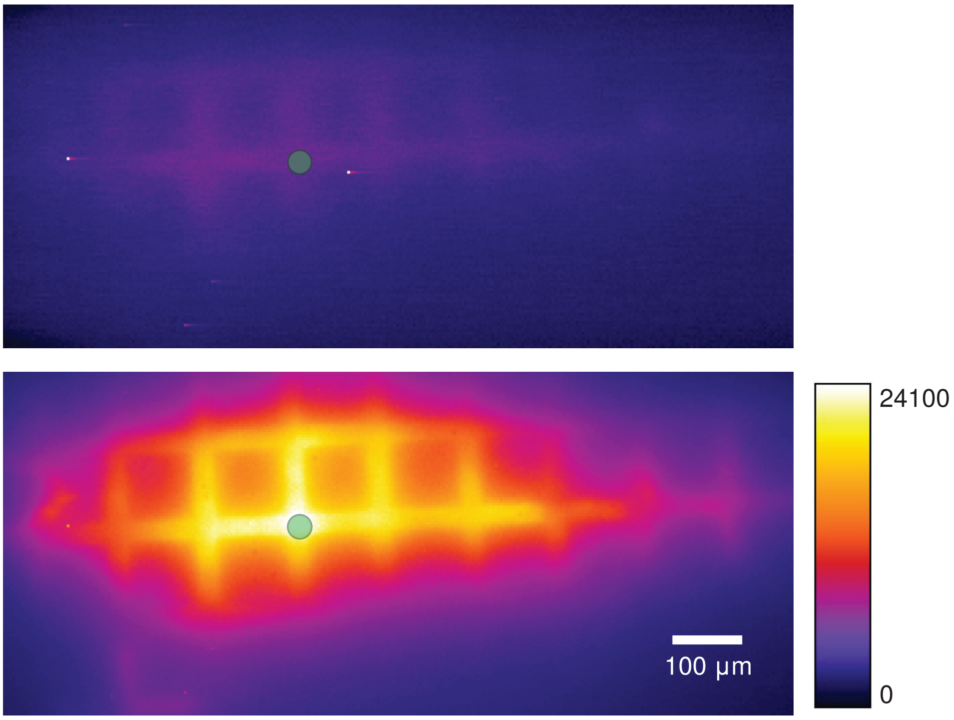

Figure 4.13: *XEOM images of a cuprite-coated copper grid viewed through (top) both the green and envelope filters, and (bottom) the green filter only.*[12]*The pixel values in the indicated equivalent regions are* ~ 600 *with both filters, but* ~ 24000 *with only the green filter.*

To aid with further investigation, additional filters (Table 4.4) were purchased to be used in combination with the existing filters. The UG1 is particularly useful since its passband covers only the visible region, which is approximately the range over which the dichroic filter transmission profiles are specified. The first definitive evidence that the manufacturer specifications are not complete was found when investigating the XEOL spectral content from a cuprite-coated copper grid. XEOM1 was set up on the DUBBLE beamline with the FLI camera in the primary detector position. The grid was affixed to the centre of a blank copper coupon and the X-ray photon energy was 9.016 keV i.e. set just above the copper edge in order to maximise the XEOL emission intensity. A 100 s image was acquired for two filter configurations: the green filter only, and the green filter plus the KG1 (Figure 4.13). It was found that the addition of the UG1 filter reduced the peak measured intensity by a factor of 40. Images of the same sample captured using the KG1 filter only contained no measurable signal (indicating a lack of emission in the UV), which suggests that the majority of the emission from the sample was in the infra-red region.

	Pass band (nm)	**Bandwidth** (nm)	**Centre wavelength** (nm)
KG1	300–400 (approx.)	100	350
UG1	300–750 (approx.)	450	525

Table 4.4: *Manufacturer specifications for the Schott UG1 and KG1 filters.*

This hypothesis was proved definitively by measurements of the transmission properties of each filter using a Shimadzu UVmini-1240 UV-Vis spectrophotometer. The scans, carried out by Pieter-Jan Sabbe (Department of Analytical Chemistry, Gent University), were taken over the full range of the instrument (190–1100 nm) and a baseline correction was applied to each spectrum. The raw data produced by the spectrophotometer are given in terms of optical density (OD) [18], which is related to the percent transmission T by

$$\mathrm{OD} = -\log\left(\frac{T}{100}\right) . \tag{4.5.1}$$

Therefore, a low OD corresponds to high transmission. For example, an OD of 2 corresponds to 1 % transmission, while an OD of 3 is equivalent to a transmission of 0.1 %.

The spectra, presented in Figure 4.14, give a clear confirmation that our suspicions were indeed correct — the filters have significant pass bands in regions outside the stated specifications. All three filters transmit light in the far-red/infra-red regions, and the main pass band of the blue filter extends into

---

[12] Images from 2011 12 DUBBLE — *'Cupritegrid_copper_green_envelope_filters000.eccd'* & *'Cupritegrid_copper_green_filter000.eccd'*

[13] Data sources: *'WS BDP BLC 2012mars29113330.txt'*, *'WS GDP BLC 22012mars29103541.txt'* & *'WS RDF VS BLC positon 32012mars28134020.txt'*

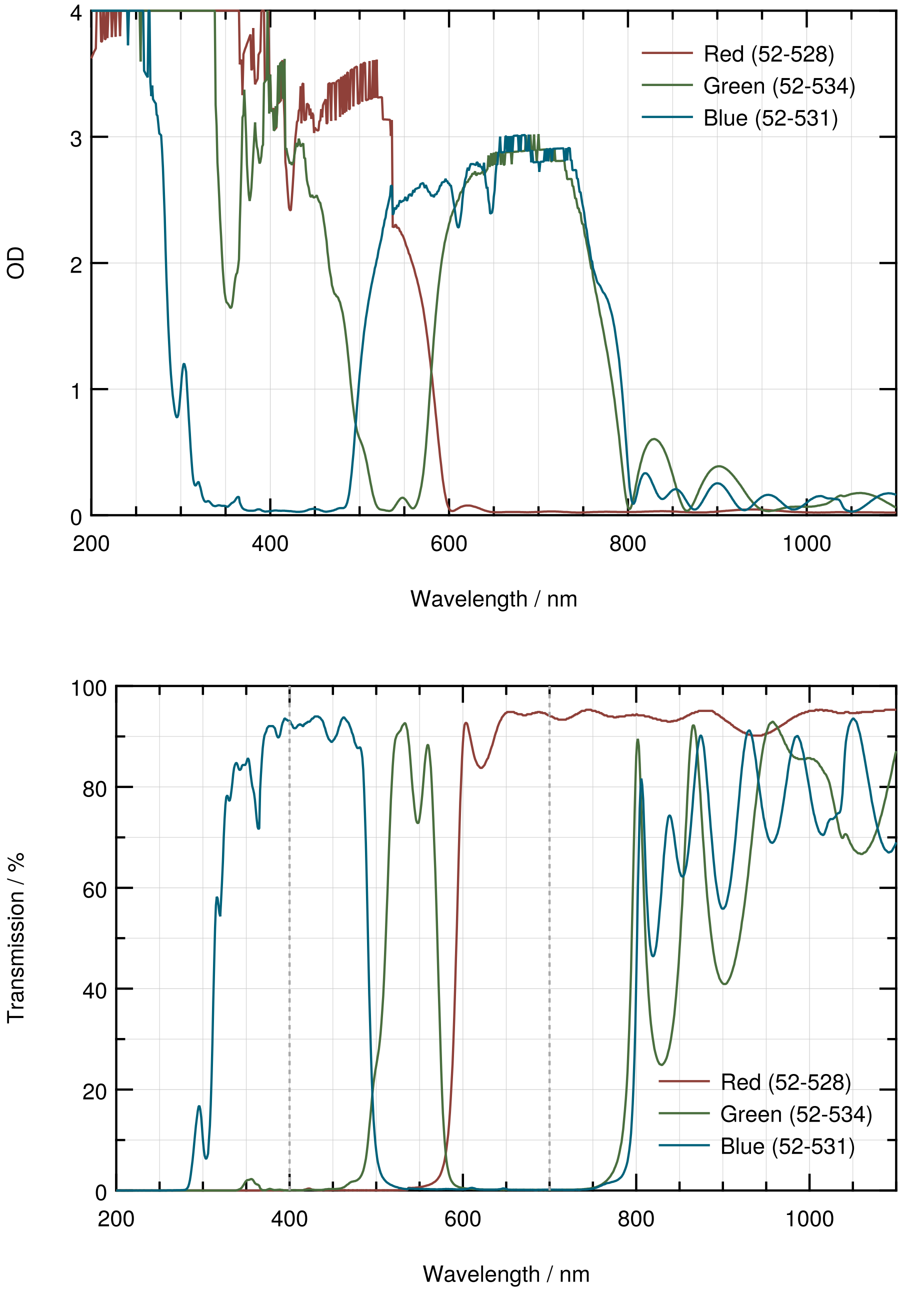

Figure 4.14: *Optical density (top) and transmission (bottom) profiles for the Edmund Optics dichroic filters.*[13] *The dashed lines indicate the limits of the region in which the manufacturer specifications define the transmission profile of the filters.*

the near-UV region. Consequently, this makes the dichroic filters unsuitable for imaging with XEOM1 and alternatives were required.

4.5.3 Fluorescence Line Filters

The requirements for the replacement filters were (a) narrower bandwidth, and (b) effective blocking outside the pass band across the entire trans-visible region. The chosen replacements were a set of Edmund Optics TECHSPEC® fluorescence line filters. These narrow bandwidth optical filters are intended for applications such as fluorescence microscopy, so they are available with a wide range of pass bands matching common fluorophores. Four filters were selected (Table 4.5) to cover pass bands in the UV, blue, green, and red regions of the electromagnetic spectrum. While the manufacturer specifications for these filters looked to be more reliable — transmission and OD curves covering our entire range of interest were supplied — their transmission properties were also tested using the spectrophotometer. These measurements were found to be in agreement with the manufacturer-supplied curves (Figure 4.15).

These particular filters were selected to roughly coincide with the nominal pass bands of the dichroic filters which allows for a more direct comparison in performance. However, since the CCD detectors in both cameras are sensitive to wavelengths up to greater than 1 μm (see Figure 3.9 in Section 3.2.2), in the future it would be beneficial to purchase additional filters which allow for filtered imaging in this extended wavelength range.

	Pass band (nm)	**Bandwidth** (nm)	**Centre wavelength** (nm)
UV (84-093)	352–402	50	377
Blue (67-027)	457–487	30	472
Green (67-031)	513–556	43	534.5
Red (84-103)	612–644	32	628

Table 4.5: *Specifications for the Edmund Optics TECHSPEC® fluorescence filters as given by the manufacturer.*

The new fluorescence filters have only been available for use at one beam-

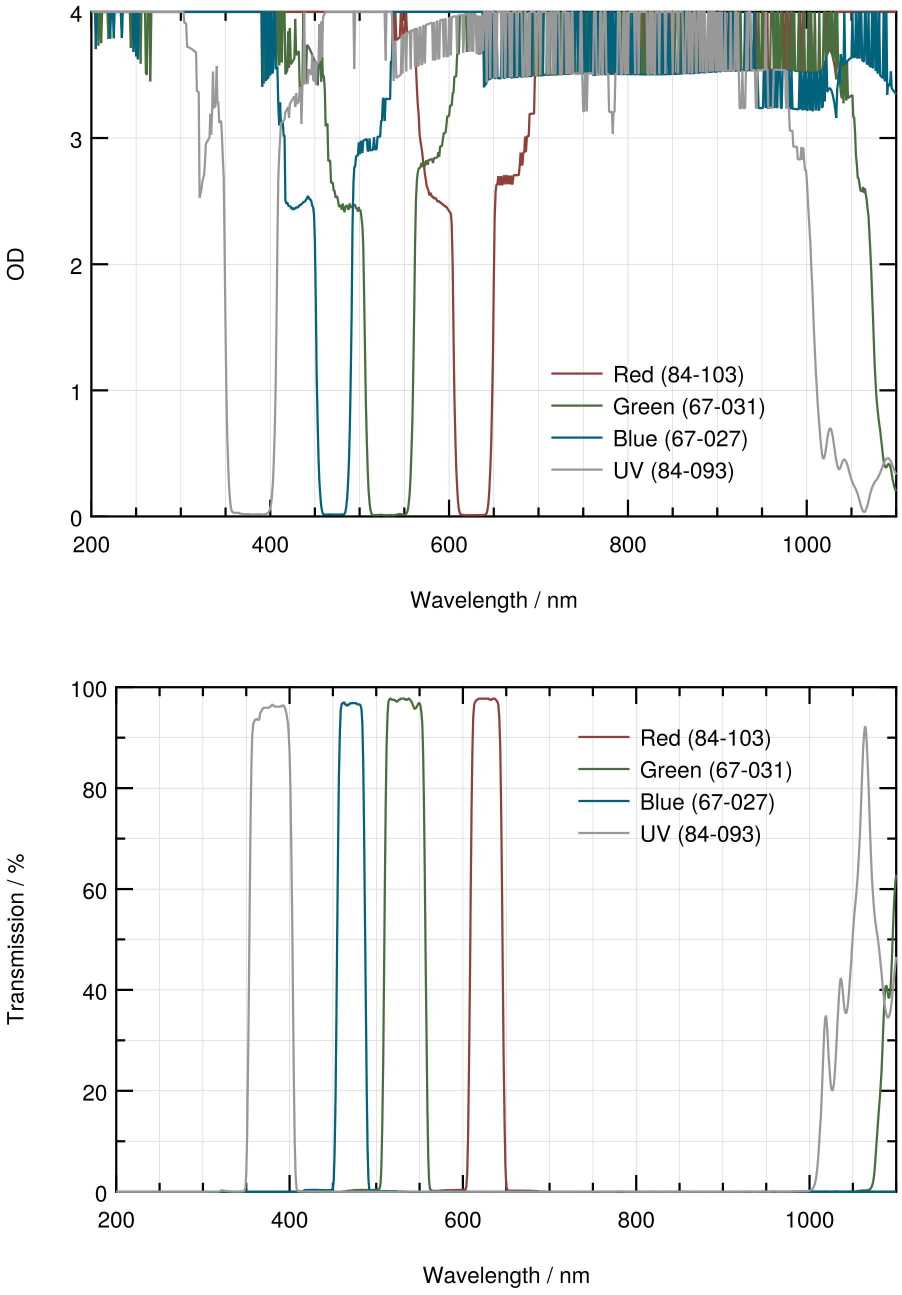

Figure 4.15: *Optical density (top) and transmission (bottom) profiles for the Edmund Optics TECHSPEC® fluorescence filters.*[14] *It is clear that the pass bands are much better defined and that that outside these regions the blocking is generally* $> \mathit{OD}\ 3$.

time allocation, but indications are that they are better suited to chemical mapping applications. Of course, more effective filtering results in an even greater loss of transmitted flux. These points will both be discussed in the following section.

4.6 Chemical Mapping

In principle, there are a number of analysis methods which may be used to extract chemical information from images captured using XEOM1. Each of these requires the use of multiple images, although the conditions under which they would be captured varies.

Arguably the simplest procedure makes use of filtering only. Under bombardment with X-rays of a particular energy, it is likely that the XEOL emission spectrum will differ for different compounds. If an image captured with a filter passing only a specific emission band produces an intensity map indicating the regions where the compound responsible for the emission is present, then a set of images gathered through different filters should map different compounds. This method is only effective if specific emission lines can unambiguously be associated with particular compounds. Hence, characterization of the technique using samples where there is a prior knowledge of both the chemical composition of the surface and the emission spectrum of the constituent compounds is essential. It is conceivable for such measurements to be carried out using a laboratory X-ray source, provided that the excitation yields suitable XEOL spectra. However, a synchrotron X-ray source still provides greater flexibility to optimize the excitation energy, select pre- or post-edge energies, and allows for significantly reduced acquisition times. High resolution XEOL emission spectra for the compounds of interest have not been obtained as XEOM1 does not yet possess spectroscopy capabilities (although this is planned — see Section 5.1) so this method has only crudely been explored through the use of filters alone.

---

[14] Data sources: *'WS UVF BLC2012avr.03181856.txt'*, *'WS BFF BLC2012avr.03172236.txt'*, *'WS GFF BLC2012avr.03162148.txt'* & *''WS RFF BLC2012avr.03175755.txt*

4.6.1 Difference Maps

A second processing method requires that two images be captured: one at an energy just below an absorption edge, and one just after the edge. The resultant of subtracting the two images is a spatial map of the absorption edge height. Since an absorption edge is only observed if the corresponding element is present, the image corresponds to an elemental map of the surface. In the case of a carefully tuned energy pre- and post edge, so as to select for a shifted edge, the imaging of oxidation state may also be possible, although there is a better way of doing this described below.

The example application of this processing method used here is unrelated to cultural heritage, but is illustrates the applicability of XEOM to other chemical systems. Figure 4.16 shows images of a sample of copper-doped bismuth selenide $Cu_{0.12}Bi_2Se_3$, a material under investigation for its properties as a topological insulator [19]. The nature of such materials is beyond the scope of this thesis, but there is interest in their potential as a route towards high-temperature superconductivity. The aim of this experiment was to gain some information regarding the distribution of copper atoms within the sample resulting from the growth method used.

Measurements of a sample (260410 II) grown by Prof. Geetha Balakrishnan (Department of Physics, University of Warwick) were carried out on the XMaS beamline. Images were acquired using the FLI camera before and after the copper absorption edge — 8.95 keV and 9 keV respectively — and, since the sample was only weakly emitting, the exposure time was 2000 s. The pre- and post-edge images themselves show little structure (apart from the arcs discussed in Section 4.4.2), but the difference image shows clear bright regions indicating that the copper at the surface layer is not distributed homogeneously, but has accumulated in pockets.

4.6.2 Image Stacks

The final, most information-rich analysis method requires that a stack of images be acquired as the X-ray energy is swept across an absorption edge, as described

---

[15] Images from 2011 02 XMaS — *'postedgebackgroundsubtracted.eccd'*, *'preedgebackgroundsubtracted.eccd'* & *'edgeheightbackgroundsubtracted.eccd'*

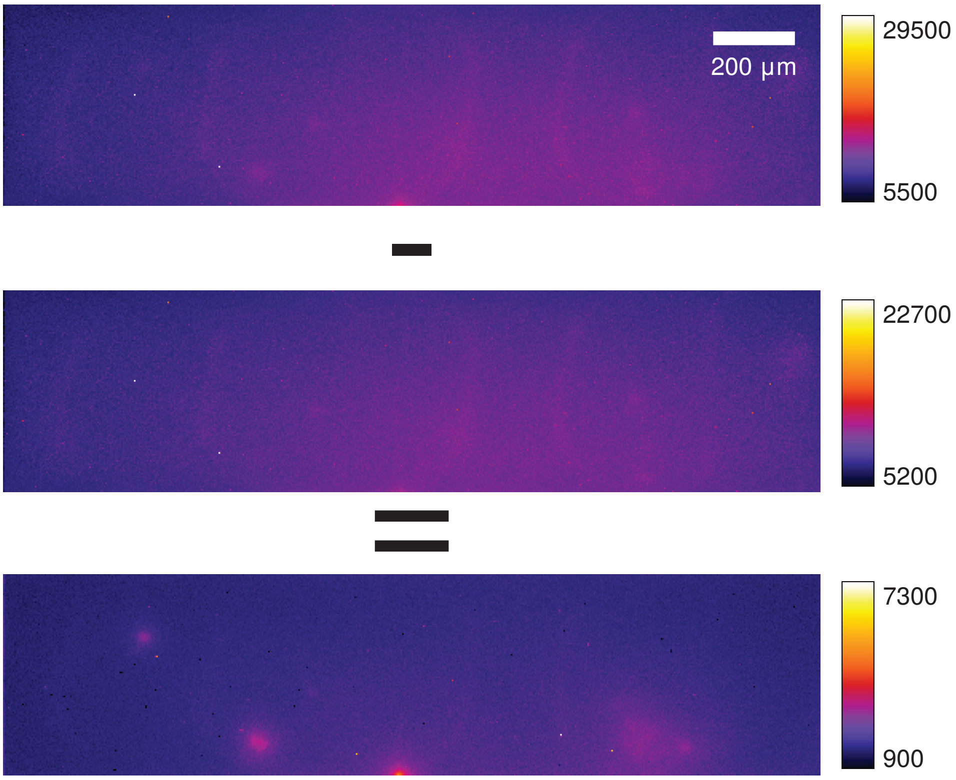

Figure 4.16: *Pre- (middle) and post- (top) copper edge images of a topological insulator $Cu_{0.12}Bi_2Se_3$. The resultant from subtracting the two images is a spatial map of the absorption edge height indicating the regions in which copper is present.*[15]

in Section 1.3. This is the mode in which it is intended that XEOM1 operated since the processing method described in Section 4.3.1 can ultimately be used to produce a *chemical* map of the surface.

Acquisition of the first image stack was done at the first XEOM1 deployment on the DUBBLE beamline. The sample was a cuprite-coated copper mesh affixed to a nantokite-coated coupon. A series of 400 images was acquired at X-ray beam energies from 8.96 to 9.2 keV with an exposure time of 1 s per point. At this stage, software automation of the stack acquisition had not yet been developed, so all image capture and monochromator stepping was done manually. No optical filter was used so much of the measured intensity results from light at unfocused wavelengths. Moreover, the ROI spectrum extraction capabilities of *esaProject* were not complete so only the integrated intensity each image could

---

[16] Image from 2010 12 DUBBLE — *'nantokitewithcupritegridtest002.eccd'*

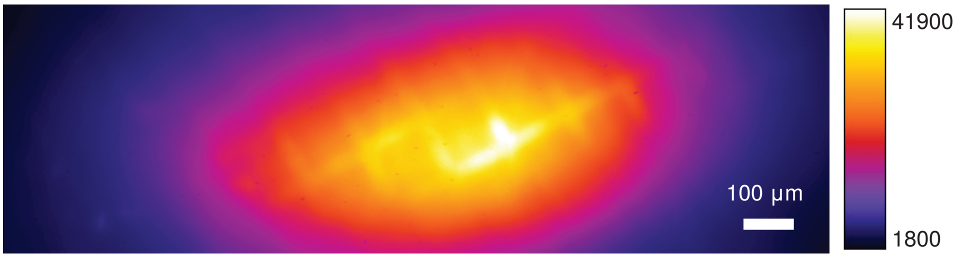

Figure 4.17: *XEOM image of the first sample of which an image stack was captured — a cuprite-coated mesh affixed to a nantokite-coated coupon.*[16]*This image was acquired using the FLI camera with an exposure time of* 20 s*. The XEOL emission is clearly dominated by that from the mesh.*

be determined. Hence, the resulting spectrum is representative of the average over the sample area within the field of view of XEOM1 (Figure 4.18) i.e. the same as a conventional optically-detected X-ray absorption spectrum. Nevertheless, it was important to demonstrate that the XAFS data are indeed present and obtainable from the image stack. The shape of the spectrum is a very close match to that of the cuprite reference — the mid-edge feature is particularly distinctive — indicating that the signal is dominated by that from the mesh. This is to be expected since the a greater intensity is measured on the observed areas corresponding to the mesh bars (Figure 4.17). However, it was quickly discovered that the visual appearance of the individual images is not necessarily a good indicator of how extracted spectra extracted from ROIs will appear.

During subsequent beam time allocations, image stacks acquired using XEOM1 typically consisted of 112 points acquired over an X-ray energy range 8.96 to 9.016 keV, which corresponds to steps of 0.5 eV. These parameters were selected to trade off between measuring a sufficiently large energy range, so that distinctive XANES features that distinguish different copper compounds will be captured, and not acquiring so many images that the total experiment duration becomes unreasonable, particularly for long exposure times (see previous discussion in Section 4.5). In fact, given that the energy resolution of both beamlines is $\sim 10^{-4}$ (see Section 4.1), which at 9 keV gives an energy resolution of ~ 1 eV, the energy step is smaller than necessary to resolve all the spectral features the beamline is capable of 'seeing'. This oversampling is particularly redundant below the absorption edge where there are no spectral features to be measured and it is only the overall background level which is of interest. An alternative

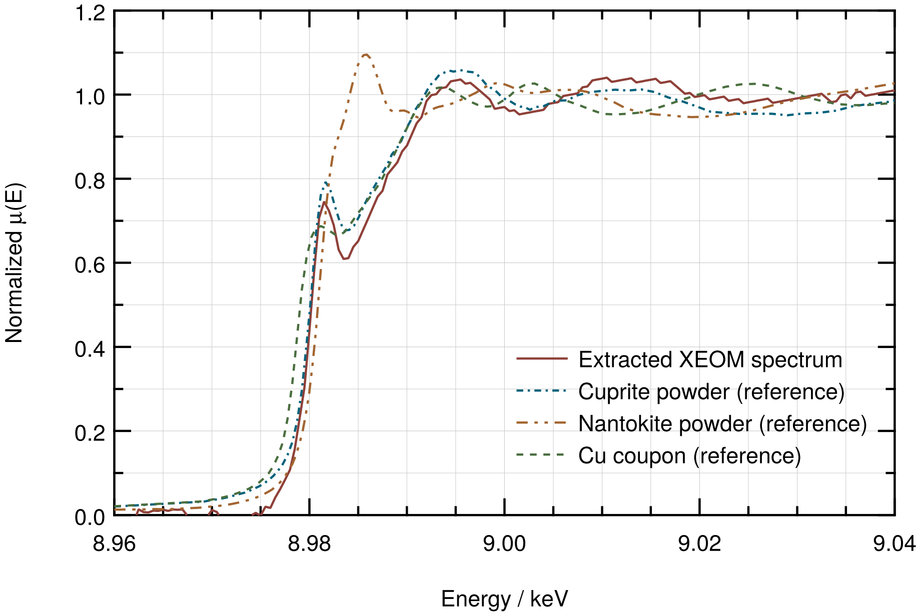

Figure 4.18: *XEOL spectrum extracted from an image stack of the sample illustrated in Figure 4.17 shown alongside reference spectra of several copper compounds. A close match to the cuprite reference spectrum confirms that the observed XEOM emission is predominantly from the mesh.*

scanning mode, `kscan`, is actually available in *spec* which is especially targeted towards XAFS measurements and allows different step sizes/acquisition times to be specified in the pre-/post-edge regions. Oversampling would not be a particular problem if the total scanning time was fast enough, but when a single scan can take several hours to cover only a limited energy range it amounts to a significant loss of time which could be used for additional measurements. The simplicity of a fixed step scan is advantageous during initial testing, but implementing the *k*-scan mode into the XEOM1 system would be very beneficial in the future, although there will be a challenge in ensuring that synchronization with the beamline system is reliable. Nevertheless, there is scope for immediately optimizing the compromise between scanning range and acquisition time by better matching the step size to the beamline capabilities.

Many image stacks have been acquired during testing of XEOM1 in an attempt to extract chemically distinct spectra from different regions of interest on a sample. However, most of this testing has been carried out using the

---

[17] Image from 2011 09 XMaS EX07 — *'cuprite grid in holder (red filter)083.eccd'*

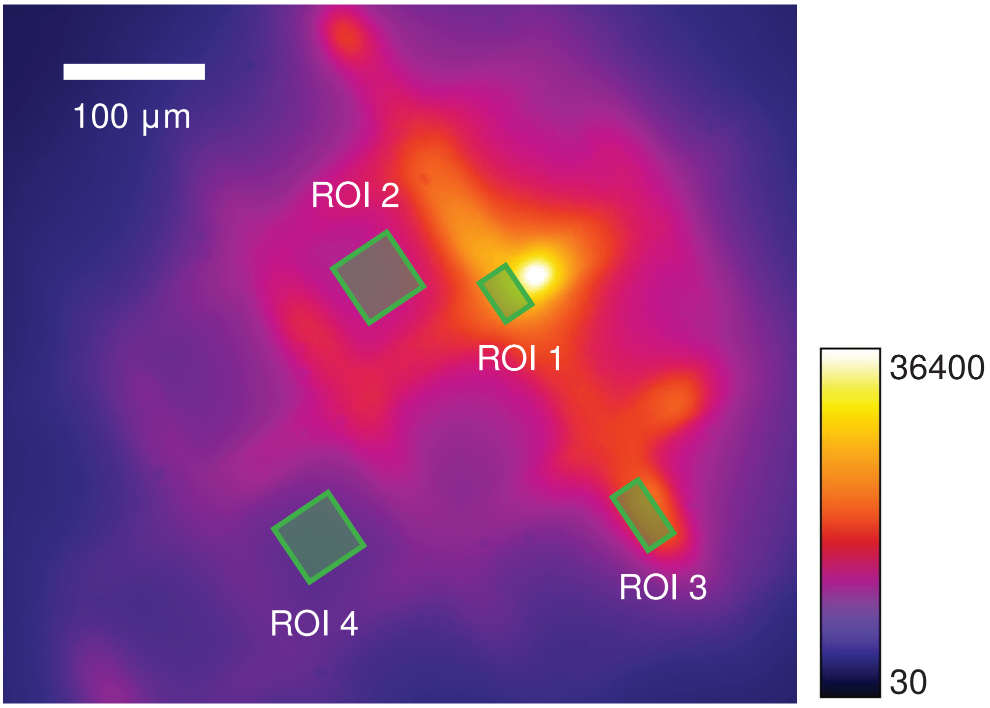

Figure 4.19: *XEOM image of a cuprite-coated copper grid mounted in the dedicated holder.*[17] *The X-ray beam energy was* 9.0115 keV, *an exposure time of* 15 s *was used, and the image was acquired through the red dichroic filter. ROIs used to extract the spectra plotted in Figure 4.20 are indicated by the green rectangles.*

dichroic filters. The extra pass bands of these filters (discussed in Section 4.5.1) in combination with the chromatic optical system of XEOM1 has been found to preclude spatial resolution of different chemical spectra. This is illustrated by measurements of a cuprite-coated copper mesh mounted in the special holder for the sample stub. Image stacks were acquired using the previously mentioned scan parameters through the red, green, and blue dichroic filters. Data from the red-filtered stack are presented here, but the green and blue-filtered data exhibit the same characteristics. As shown in Figure 4.19, an image of the mesh bars is clearly resolved. The spectra plotted in Figure 4.20 were extracted from the ROIs indicated: two on the bars themselves (ROIs 1 and 3), and two in the holes between the bars (ROIs 2 and 4). The sample holder is produced from acetal copolymer, a material selected for its lack of XEOL emission, so it is not expected that a copper edge be observed in ROIs 2 or 4. However, not only do the extracted spectra show a clear copper edge, they are identical to those extracted from the ROIs 1 and 3 which, as expected, are characteristic of cuprite. It is highly probable that the signal being detected here is the emission which is being transmitted by the undocumented pass bands of the dichroic filter. Since the focus lens position is not set for these wavelengths, the light is distributed across the entire surface of the sensor contributing to the anomalous spectra.

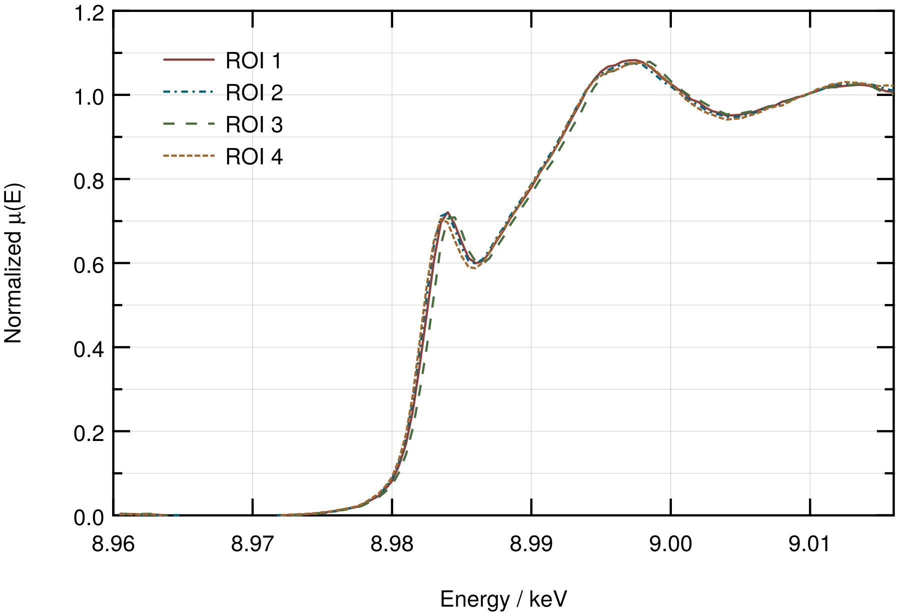

Figure 4.20: *XEOL spectra extracted from ROIs indicated in Figure 4.19. All four spectra have an identical shape viz. they are characteristic of cuprite. This is expected for ROIs 1 and 3 (on the mesh), but the spectra extracted from ROIs 2 and 4 should not contain any sign of a copper edge.*

Both the Andor camera and the fluorescence line filters have only been available at the latest beam time allocation at XMaS, so there has been very limited time to test XEOM1 using these newer components. However, indications are that they are both contributing to somewhat improved data quality. The bright arcs discussed in Section 4.4.2 do not appear in images acquired using the Andor camera, the final confirmation that the FLI camera is defective. Additionally, the narrow bandwidth and superior blocking of the new filters has been found to give better defined focal positions and multiple foci are no longer observed.

Figure 4.21 shows two images of a sample consisting of a nantokite-coated mesh on a cuprite-coated coupon. Image stacks were acquired through each of the fluorescence line filters with the following acquisition times: red – 270 s (much longer only to utilize overnight scan time), green – 35 s, blue – 35 s, UV – 1 s. In each case, the focus lens position was set to give the best image focus as determined by visual observation. Images acquired through the UV, green, and blue filters all showed an emission distribution like that illustrated in Figure 4.21 (top) i.e. it is dominated by emission from the coupon, and the mesh acts only to shadow the underlying surface. However, images acquired through the red filter appeared rather differently as shown in Figure 4.21 (bottom). The strongest emission is now observed from the grid rather the coupon, indicating that nantokite emits more strongly in the red. Additionally, only a small region of the mesh is emitting significantly, indicating that the nantokite coating does not form uniformly on the bars. This is in contrast with the first image where the intensity distribution follows that of the X-ray beam footprint, suggesting a more uniform layer of cuprite forms on the coupon.

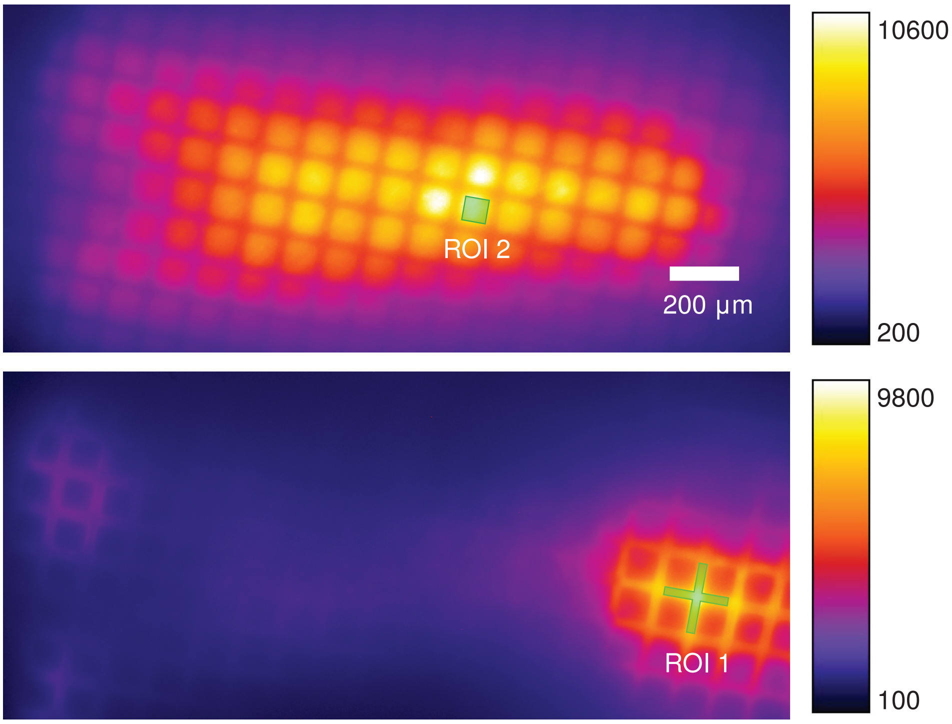

Figure 4.21: *XEOM images of a nanotokite-coated grid on a cuprite-coated captured with green (top) and red (bottom) filters inserted.*[18]*Both images were acquired at an X-ray energy of* 9 keV. *The green regions indicate the ROIs to extract the spectra plotted in Figure 4.22.*

This is the first sign of significant chemical differentiation which has been observed in images acquired using XEOM1. Areas where emission of red light occurs clearly correlate with regions where it is known that nantokite is present (the mesh) and emission in other colour bands correlates with regions where cuprite is present (the coupon). In fact, this acts as a demonstration of how XEOL emission in different wavebands for different compounds can be used to form a chemical map (as described at the beginning of this section). However, the primary aim has been to achieve chemical differentiation by comparing spectra extracted from different regions.

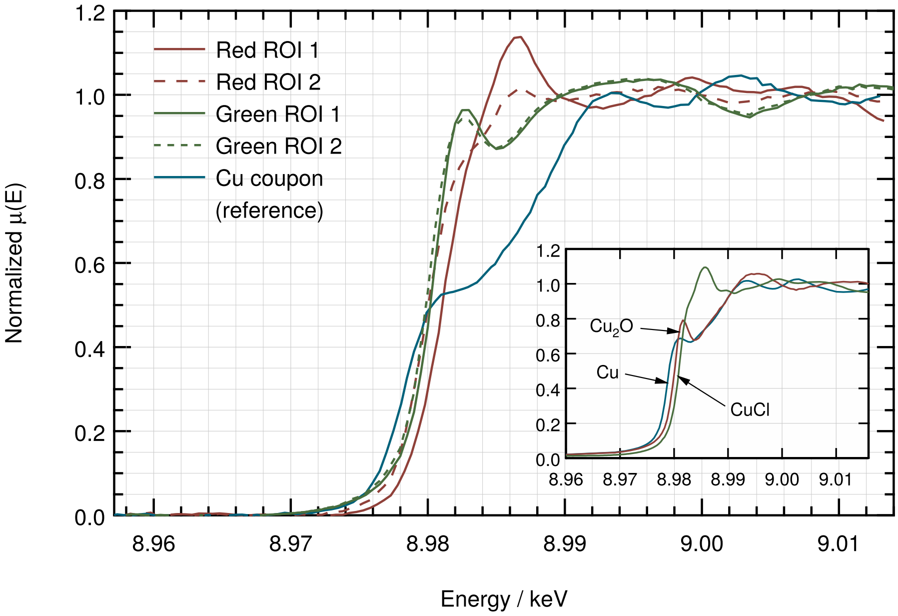

Figure 4.22: *Spectra extracted from ROI 1 and 2 (indicated in Figure 4.21) when applied to green and red filtered image stacks of a nantokite-coated mesh on a cuprite-coated coupon. Inset: reference spectra of cuprite and nantokite powders acquired during a previous beamtime at DUBBLE.*

Figure 4.22 shows XEOL spectra extracted from the two ROIs indicated in Figure 4.21. It is expected that the spectra extracted from ROI 1 will be characteristic of nantokite, regardless of the filter used, and spectra extracted from ROI 2 will be characteristic of cuprite. However, it is clear that this is not the case. Both spectra extracted from the stack acquired using the green filter are

---

[18] Images from 2012 10 XMaS EX14 — *'cuprite coupon nantokite grid green filter stack-080.eccd'* & *'cuprite coupon nantokite grid red filter stack-080.eccd'*

characteristic of cuprite. When compared with the reference XEOL-XANES spectrum obtained from cuprite powder, the amplitude of the post-edge oscillations is slightly suppressed. This is normally associated in conventional fluorescence XAS measurements with self-absorption effects [20] — for thick, concentrated samples the post-edge attenuation length is shorter due to increased absorption, so a smaller volume is sampled and the oscillation amplitude is suppressed — but this is not expected to occur in XEOL spectra due to the inherent surface sensitivity of the technique. Rather, the observed difference in intensity may be a consequence of changes in the decay channel and subsequent end states as the X-ray energy moves over the absorption edge, a possibility mentioned in Section 4.3.2.

For example, the pre-edge emission will result from inefficient excitation of L-level Auger transitions in the copper atoms, plus possible contributions from excitation of other constituent elements and surface contaminants. At the edge itself, K-level absorption takes over so the principal non-radiative electron decay mechanism switches across to a KLL Auger transition e.g. $KL_1L_{2,3}$ (not possible before the edge). If the pre- and post-edge de-excitation channels are different it would not be surprising to find that the end states are either different, or excited with greater or lesser efficiency. In this case, it would appear that the change in de-excitation channel results in a reduced visible photon flux beyond the edge, despite a greater absorption of X-rays. These observations are in partial agreement with [17] as a change in the visible emission of cuprite was observed as the X-ray energy moved across the Cu edge. However, in that case the change occurred while the X-ray energy corresponded to a point in the initial portion of the rising edge, so the relative position of the inter-band transition feature w.r.t. the post edge level was comparable to that observed in a conventional fluorescence spectrum. Here, that same feature is observed at a position very close to the post-edge level suggesting that the change in emission occurs at an X-ray energy corresponding to a point just after this feature. Nevertheless, this serves to illustrate one of the extra complications in interpreting XEOL data which arises from the de-coupled nature of the X-ray absorption and visible photon emission processes.

The spectra extracted from the stack acquired using the red filter are largely characteristic of nantokite, as indicated by the intense white line, but some differences between the spectra are now observed. The spectrum extracted from ROI 1 (the mesh) appears to be pure nantokite; it is a very close match to the reference. However, the intensity of the white line in the spectrum extracted from ROI 2 (the coupon) is somewhat reduced. In addition, there are indications of a feature on the edge which correlates with that observed in the cuprite spectrum. Moreover, the edge shift is not as great as would be expected for pure nantokite and is more in line with that of cuprite. These characteristics would usually indicate the presence of a mixture of nantokite and cuprite in the region enclosed by ROI 2. However, given that ROI 2 encloses an area from which it is expected to only measure the cuprite-coated coupon, it is more likely that the shape of the spectrum is a result of the same optical aberrations which have previously been observed. Therefore, it must be concluded that although the new filters have improved the blocking of unwanted light to the point where chemical differentiation is now observed in differently filtered images of the same sample, the spatial resolution is still not sufficient for clear chemical differentiation to be observed in ROI extracted XEOL spectra.

Nevertheless, it is still possible to gain some insight through inspection of the raw intensity spectra before they have been converted to normalised $\mu(E)$. Figure 4.23 shows the same spectra as plotted in Figure 4.22 (plus the UV and blue filtered data), but now the measured intensities have only been normalised to the beam monitor signal (accounts for decay of flux and monochromator glitches) and to the exposure times used for each stack.

The observed intensity from both ROIs is by far the strongest when extracting spectra from the stack acquired using the UV filter (this could be predicted based on the very short exposure time required for this stack). In contrast, the weakest signal is observed when the red filter is used. However, an examination of the material properties finds that this is not necessarily correlate with the expected emission pattern. Cuprite is a semiconductor with a direct bandgap of 1.9–2.4 eV [21, 22] so one might expect radiative recombination of electrons and holes to produce photons in the 516–652 nm range. This bandwidth partially intersects with the pass bands of both the green and red fluorescence filters. Nantokite is also a semiconductor, but with a larger direct bandgap of 3.4 eV [23]; this corresponds to an optical wavelength of 364 nm (covered by the UV filter). Since the ROIs map to two different regions on the sample and

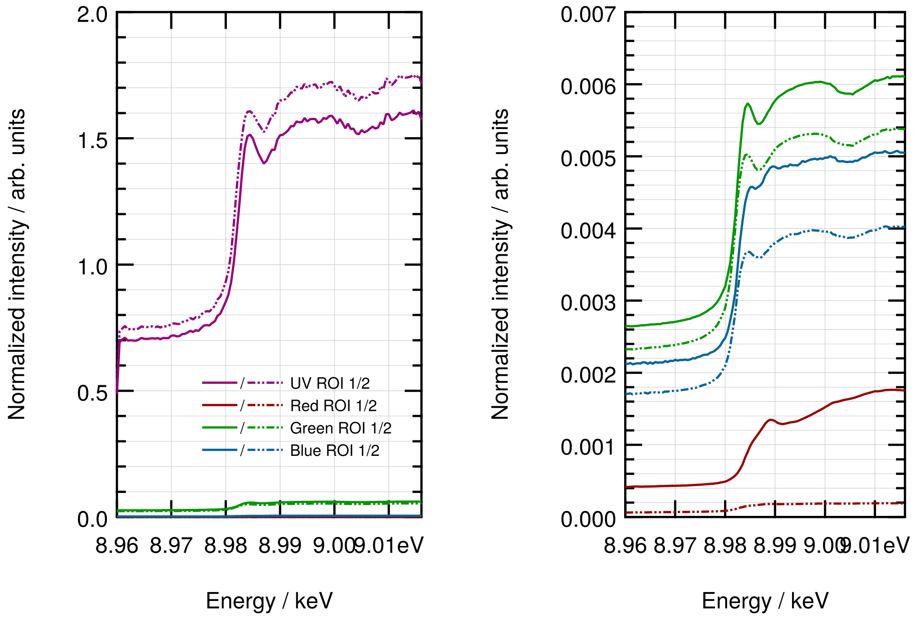

Figure 4.23: *Raw intensity spectra extracted from ROI 1 (solid) and 2 (dashed), as indicated in Figure 4.21, using UV, red, green and blue filters. Spectra have been normalised to the beam monitor signal and to exposure time. Left: raw spectra — the relative intensity of the red and blue emission is so small that these spectra are not discernable on this scale. Right: the UV spectrum has been removed from plot and a multiplication factor of* 0.1 *has been applied to the data extracted from the green-filtered stack.*

their areas are different, the relative intensities can only be compared between spectra extracted from the same ROI. However, while the absolute UV emission intensities from the two ROIs cannot be directly compared, the intensity of the UV spectra relative to other filters and the shape of the spectrum that the cuprite is strongly emitting in at least part of the bandwidth covered by the UV filter. Some emission is observed in the wavebands associated with the band gap energy, but this clearly does not tell the whole story and reinforces the case for the addition of spectroscopy capabilities to XEOM1 (see Section 5.1).

Despite being the weakest emission band in both ROIs, the raw red-filtered spectra show the most interesting spectral features, as have already been seen in the normalized $\mu(E)$ spectra (Figure 4.22). However, the additional processing which was previously applied hides information about the height of the absorption edge step. Spectra extracted from stacks acquired using filters other than red have an average post-edge emission level of approximately 2.2–2.3 times that of the pre-edge level. However, the red-filtered spectra show different behaviour: the spectrum extracted from ROI 2 has an edge step of 2.6×, but the spectrum extracted from ROI 1 has an initial post-edge level of 3.1× which increases to 4.1× by the end of the scan. This is indicative of a spectral shift in the visible emission caused by evolution of the electron decay processes as the incoming X-ray energy increases beyond the absorption edge. Importantly, this is only observed in the spectra which show characteristics of nantokite XANES [24] suggesting that this effect is only occurring in the nantokite coating the copper-mesh. This also correlates with the greatest emission intensity being observed from the mesh itself only in the red-filtered XEOM images.

4.7 Summary

This chapter began with a description of the set-up of the XEOM1 system on the two beamlines at which it has been deployed, and the differences between the interface with the beamline systems themselves. This was followed by an overview of the types of sample which have been used for testing XEOM1 and the corrosion protocols which have been used to produce them. The software which has been used for processing and analysis of both the XEOM images and the extracted spectra have been described.

The remainder of this chapter focused on the experimental testing of XEOM1 which has driven its continued development. Data from the initial measurements were presented, including those which allowed for the identification of hardware defects which prompted the replacement of the primary imaging camera. Next, the use of filtered imaging was described, and a comparison between the two different types of filter which have been used has been given. Finally, data from the first attempts at chemical mapping were presented. These have demonstrated that chemical differentiation is achievable through the use of different coloured filters, but that there is still more work to be done before it will be possible to produce detailed chemical maps from a single image stack.

References

[1] D F Paul, M J Cooper, and W G Stirling. Design of an x-ray beamline on a bending magnet at the ESRF for magnetic and high resolution diffraction. *Rev. Sci. Instrum.*, 66(2):1741, 1995.

[2] S D Brown, et al. The XMaS beamline at ESRF: instrumental developments and high-resolution diffraction studies. *J. Synchrotron Radiat.*, 8(6):1172–1181, 2001.

[3] M Borsboom, et al. The Dutch-Belgian beamline at the ESRF. *J. Synchrotron Radiat.*, 5(Pt 3):518–20, May 1998.

[4] O Glatter and O Kratky, editors. *Small Angle X-ray Scattering*. Academic Press, London, 1982.

[5] M V Petoukhov and D I Svergun. Applications of small-angle X-ray scattering to biomacromolecular solutions. *Int. J. Biochem. Cell Biol.*, 45(2): 429–37, February 2013.

[6] Heng Liu, et al. QXAFS system of the BL14W1 XAFS beamline at the Shanghai Synchrotron Radiation Facility. *J. Synchrotron Radiat.*, 19(6):969–75, November 2012.

[7] E Fonda, et al. The SAMBA quick-EXAFS monochromator: XAS with edge jumping. *J. Synchrotron Radiat.*, 19(Pt 3):417–24, May 2012.

[8] J B Khazaie and C Boulin. Time frame generator for x-ray detectors and data acquisition systems for synchrotron radiation applications in molecular biology. *IEEE Trans. Nucl. Sci.*, 43(1):197–201, 1996.

[9] R B Faltermeier. A Corrosion Inhibitor Test For Copper-based Artifacts. *Stud. Conserv.*, 44:121–128, 1998.

[10] T Beldjoudi. Synthèse des Travaux. Technical report, Valectra, 1999.

[11] K P Fitzgerald, et al. Atmospheric corrosion of copper and the colour, structure and composition of natural patinas on copper. *Corros. Sci.*, 48 (9):2480–2509, September 2006.

[12] F Mathis, et al. HMTY-KM (black copper) and the Egyptian bronzes' collection of the Musée du Louvre. *J. Cult. Herit.*, 10(1):63–72, January 2009.

[13] D A Scott. *Copper and Bronze in Art: Corrosion, Colorants, Conservation*. Getty Trust Publications, 2002.

[14] M G Dowsett, et al. Optically detected X-ray absorption spectroscopy mea-

surements as a means of monitoring corrosion layers on copper. *Anal. Chem.*, 80(22):8717–24, 2008.

[15] A Adriaens, et al. Insights into electrolytic stabilization with weak polarization as treatment for archaeological copper objects. *Anal. Bioanal. Chem.*, 387(3):861–8, 2007.

[16] G Van Der Laan and B T Thole. Determination of glitches in soft X-ray monochromator crystals. *Nucl. Instrum. Meth. A*, 263(2-3):515–521, 1988.

[17] A Adriaens, et al. Real time observation of X-ray induced surface modification using simultaneous XANES and XEOL-XANES. *Anal. Chem.*, 85(20): 9556–9563, 2013.

[18] W J Smith. *Modern Optical Engineering: The Design of Optical Systems*. McGraw-Hill, New York, 3rd ed. edition, 2000.

[19] Y S Hor, A J Williams, and J G Checkelsky. Superconductivity in CuxBi2Se3 and its Implications for Pairing in the Undoped Topological Insulator. *Phys. Rev. Lett.*, 104:1–4, 2010.

[20] G Bunker. *Introduction to XAFS: A Practical Guide to X-ray Absorption Fine Structure Spectroscopy*. CUP, 2010.

[21] I Grozdanov. Electroless chemical deposition technique for Cu2O thin films. *Mater. Lett.*, 19:281–285, 1994.

[22] C M McShane and K-S Choi. Photocurrent enhancement of n-type Cu2O electrodes achieved by controlling dendritic branching growth. *J. Am. Chem. Soc.*, 131(7):2561–9, March 2009.

[23] N J Doran and A M Woolley. The band structure of CuCl. *J. Phys. C*, 12: 321, 1979.

[24] A Adriaens, et al. An in-situ X-ray absorption spectroelectrochemistry study of the response of artificial chloride corrosion layers on copper to remedial treatment. *J. Anal. At. Spectrom.*, 24(1):62, 2009.

Chapter 5

Further Work

Although considerable effort has been put into getting XEOM1 to its current state of development, there are clearly still routes available for further evolution of the hardware. Of course, the primary target for improvement is the chemical differentiation, or lack thereof, observed in XEOL spectra extracted from image stacks. However, in terms of specific hardware developments and related investigations, there are several areas in which ongoing work can be concentrated.

5.1 XEOL Spectroscopy

Over the course of this project it has become very clear that the capability to measure the optical spectrum of the XEOL emission from a sample would be extremely useful. Not only can this provide information about the sample — determination of specific emission lines and comparison with reference spectra may reveal details of the composition and electronic structure — but it will also aid in the selection of the appropriate filters for acquisition of image stacks. Currently, the limited selection of filters available in combination with their narrow pass bands means that only a portion of the trans-visible region is covered. The strongest emission peaks for a particular sample could be at wavelengths outside this region, so the ability to effectively target the filter selection for maximum signal acquisition would be a significant step towards minimising experiment duration.

The addition of a spectroscopy arm to XEOM1 was originally within the scope of this project, but tackling both the hardware defect issues and the problem with a lack of chemical differentiation became a priority. A concept for this development, based on the current optical design, is shown in Figure 5.1. It utilises a diffraction grating placed within the primary column in order to disperse light of different wavelengths across the surface of an area detector i.e. a spectrographic system (one in which a wide spectral region is imaged at once [1]). The initial primary detector, the FLI camera, would become the spectroscopy detector in this design.

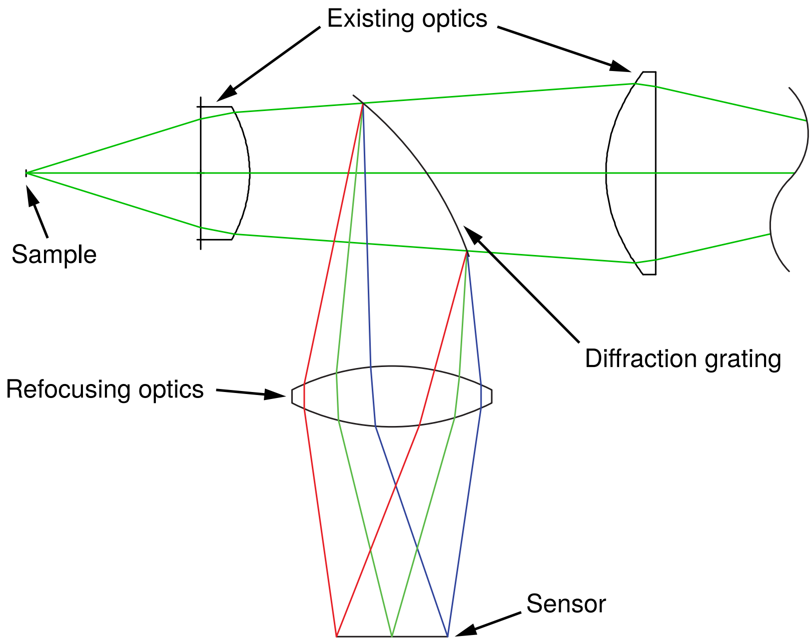

Figure 5.1: *Schematic concept design for the addition of a secondary optical branch to XEOM1 aimed at XEOL spectroscopy.*

If the spectrograph is to be integrated into the current design, a concave reflection grating to be introduced between the first two lenses would likely be the best choice. It is possible to manufacture holographic or variable line spacing (VLS) gratings for which the focal plane of the spectrum is flat [2], making them ideal for use with an area detector. Secondary focusing optics may be required to in order to make most efficient use of the rectangular sensor. For example, two anamorphic lenses may be necessary. Such lenses have two different radii of curvature in orthogonal directions, although in practice one of these radii will be infinite i.e. it will be a cylindrical lens; light will be focused into a line as opposed to a point. Hence the need for two lenses, one of which would be rotated by 90° about the optical axis: one to distribute the spectrum across the length of the sensor in order to optimize the wavelength resolution, and a second to condense the image in the orthogonal direction to maximise measured intensity.

Further design work would need to be done in order to determine the optical requirements for the spectrograph components, plus geometrical and mechanical factors need to be considered. It may not even be feasible to adapt the current optical design to include a spectrographic arm. In this case other options would need to be considered, such as coupling an external spectrometer via an optical fibre.

5.2 New Optics Concept

The philosophy behind the original optics design was that of maximum light collection capability with respect to both bandwidth and overall intensity. As described in Section 3.1, this motivated the decisions to build a large numerical aperture system from a single optical glass. The low XEOL exhibited by fused silica was also a factor in the decision. Ultimately, this has resulted in an optical system which exhibits high chromatic aberration, making filtering of the XEOL emission an absolute necessity for well-resolved imaging.

On order to build polychromatic optics the system must contain optical elements figured from at least two different glasses with distinct refractive indices. However, the majority of glasses have optical characteristics which prevent transmission in most or all of the UV part of the electromagnetic spectrum. Recently, truly broadband[1] achromatic lenses have become available — for a price. A CaF_2-UVFS-CaF_2 triplet lens provides a consistent focal length for wavelengths raging from 193 to 1000 nm, but cost upwards of £1600 per lens (Edmund Optics Ltd., York, UK) [3]. A system of fully-corrected optics would be beneficial for capturing images over wide bandwidths (even unfiltered), although this benefit is lost when targeting specific emission bands in very narrow bandwidths. Additionally, a lens of this type could not be used as the first element in the

---

[1] When used by optics manufacturers, ‘broadband’ often only refers to the visible portion of the spectrum.

optical system since CaF_2 exhibits high XEOL emission — the earliest reported XEOL-XAS spectrum was taken from CaF_2 [4] — so, at the very least, a UVFS flat would be required beforehand.

A more radical approach to building a polychromatic system would be to use reflective optics. Mirrors are naturally achromatic which immediately eliminates the problem of chromatic aberration. However, the Al-MgF_2 UV-enhanced broadband coatings used to give an optical range comparable to that of UV-grade fused silica only have a reflection efficiency of 80–90 % (Princeton Instruments Inc., Trenton, USA) [5]. Therefore, the optical system would have to be carefully designed to minimise the number of reflecting surfaces used or a significant portion of the XEOL emission entering the system will be lost.

5.3 Filter Wheel

In order to isolate and image specific emission bands associated with particular compounds it is clearly necessary to select the appropriate colour filter. The e2v sensor installed in the Andor camera is sensitive over a 200–1100 nm range, but it is not possible to fully utilize this using the four fluorescence line filters currently available. The problem is easily solved by purchasing a number of new filters in order to target emission in pass bands which it is not currently possible to isolate. However, XEOM1 only has the capacity to hold one filter at a time so changing it currently requires entering the experimental hutch and swapping the filter manually. This represents an additional time overhead between measurements which it would be desirable to avoid, especially if more filters are to be used.

Streamlining the filter changing process can be achieved by replacing the single filter holder with a carrier capable of holding multiple filters simultaneously which can be remotely operated from outside the experimental hutch. A mechanical design for such a device has already been produced by Prof. Mark Dowsett, as shown in Figure 5.2, but it has not yet been manufactured. The EIU already has spare capacity to drive the additional stepper motor required, but some new functionality will need to be written into eCell Controller. A feedback mechanism utilising a rotary potentiometer, similar to that used for the focusing lens (Section 3.2.1), will allow the position of the wheel to be determined.

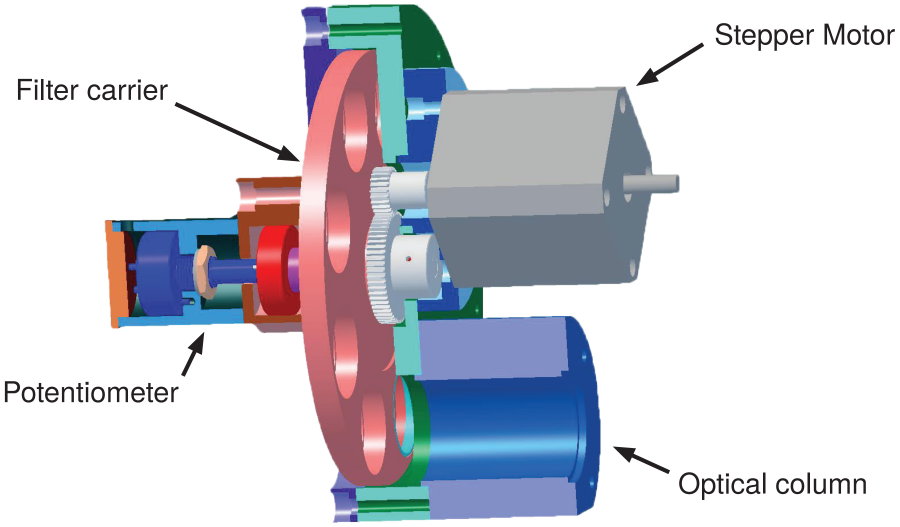

Figure 5.2: *3D section view of the filter wheel design exported from Alibre Design (now Geomagic Design 2013), 3D Systems Inc. Design by Mark Dowsett* © EVA Surface Analysis *2013.*

Associating each filter with a rotary position will allow for the mechanism to be driven to the correct position by simply selecting the desired filter in the software. A slightly more sophisticated software implementation would require that only the desired wavelength be selected, and both the filter wheel and focusing lens would move to the corresponding positions simultaneously.

5.4 X-ray Beam Effects

When synchrotron-based analyses are used in the context of cultural heritage research they are often claimed to be non-destructive [6–8]. However, a high intensity photon beam can result in radiation damage and chemical changes due to photoreduction have been reported in studies of iron gall ink on historical manuscripts [9]. Moreover, a recent investigation into synchrotron X-ray induced surface modification has been carried out using ODXAS1 [10]. Microbeam XANES and XEOL-XANES measurements showed clear evolution of nantokite into paratacamite (another copper hydroxychloride, a polymorph of atacamite) under X-ray bombardment, and other observed features in the data were attributed to surface cleaning by the beam and the melting of lead grains in lead bronze.

In fact, a further motivation for building XEOM1 was to investigate whether the use of a macro-scale X-ray beam for full-field XEOL imaging reduces the susceptibility of the sample to X-ray induced effects when compared a μ-beam used for scanning probe imaging i.e. does the X-ray flux density at the sample have an impact on the severity of any observed destructive effects. Even if the application of synchrotron X-rays to a heritage artefact has no immediate impact, either visually or manifested in the data, there is potential for the long term stability of the object to be affected. An instance where a “non-destructive” analytical technique has caused long-term damage to an artefact has been particle-induced X-ray emission spectroscopy (PIXE) measurements of the painting *Madonna Dei Dusi* by Leonardo da Vinci [11]. Differential spectra i.e. spectra obtained at different proton energies, were acquired in order to identify pigments and to obtain information about the stratigraphy of paint and varnish layers. At the time of the measurements there was no visible effect on the painting, but over the following 12 months, white patches developed where the proton beam had been [12]. Given the time-scales over which it is desired to preserve historical artefacts, it is unfortunate when analysis done now causes deterioration of the artefact many years in the future, so this is clearly an area of investigation worth exploring.

5.5 Data Processing

In Section 4.3.2 an alternative strategy for post-processing of XEOL spectra mentioned and will be described here. A disconnect between the pre- and post-edge emission processes can result in a background level which does not correspond to the ‘zero’ level of the subsequent XAFS spectrum. In this situation distortion of the edge gradient and relative position of edge features can occur if a conventional pre-edge subtraction is applied. In the extreme case that none of the pre-edge emission channels continue to be excited after the edge, the following procedure can be applied:

1. Locate the edge position

2. Fit a spline to the pre-edge background until just before the edge
3. Fit a second spline to the lower portion of the edge and extrapolate towards zero
4. Subtract the second spline from the first producing a function which goes to zero by the centre of the edge
5. Subtract this from the dataset

Clearly the bounds for the spline fitting must be carefully chosen, as is the case when using *Athena*, to avoid distorting the data, but an implementation could reasonably written such that a sensible first choice is made by the algorithm for most data sets; this functionality is currently being incorporated into *esaProject*.

The intermediate case, where the pre-edge emission channels continue to contribute to the post-edge signal with reduced efficiency, is more challenging. Without prior knowledge of how the decay channels and end states change as the X-ray energy moves across the absorption edge it is unclear how the background profile to be subtracted can be determined. In this case, comparison with XANES data obtained via fluorescence or transmission measurements should give a good indication of how the undistorted spectrum appears, and this can be used to guide the processing of the XEOL data.

Even in the simpler cases where either the XANES data sit on top of the pre-edge emission or the emission channels switch off completely at the edge, the processing of the data requires at least some manual intervention. This is acceptable when applied to only a handful of spectra, but in principle it is possible to generate over 4 million spectra per image stack if spectrum extraction were to be done on a pixel-by-pixel basis (the usefulness of such an exercise is highly dependant on the statistics of the resulting spectra). Therefore, a greater degree of automation for these processing tasks is highly desirable.

5.5.1 Linear Combination Fitting and Principal Component Analysis

The next step after the aforementioned processing is to represent the spatial variation in the extracted XEOL spectra in order to produce a final chemical map. Therefore, it is necessary to find a way of quantifying spectral differences in a manner which can easily be represented in an image. One approach is to apply a technique known as linear combination fitting (LCF) [13]. When the sample consists of a mixture of absorbing atoms in inequivalent sites, i.e. different chemical states, the measured spectrum $\mu_{\text{meas}}(E)$ corresponds to a weighted average of the $\mu_k(E)$ corresponding to each site

$$\mu_{\text{meas}}(E) = \sum_k c_k \mu_k(E) \, , \tag{5.5.1}$$

where c_k are the weighting coefficients, and $\sum_k c_k = 1$. In principal, a suitable collection of reference spectra from different compounds may be fitted to the measured data in order to determine the fraction of each compound present. In practice, it is not always straightforward to accurately determine the c_k since both the measured and reference data need to be of sufficiently high quality, and should ideally be recorded under similar conditions. Nevertheless, generating a map of the coefficients provides a relatively straightforward method of representing the spatial distribution of compounds present on the sample.

A related procedure is that of principal component analysis (PCA) which finds a linear combination of basis spectra so as to minimise the number of these spectra needed to reproduce the measured spectrum accurately. While it is not guaranteed that the new set of spectra will represent any physical spectra of interest, the number of these basis spectra is indicative of the number of major components in the data and can be useful for understanding the intrinsic complexity of the spectrum [14].

5.6 eCell

As with ODXAS1, the front end of XEOM1 was designed to couple with an electrochemical cell, the eCell (see Section 2.4), to enable spectroelectrochemical analyses to be carried out. Since development of both the hardware and software related to the XEOM1 system is still ongoing and characterisation of the optical system using test samples is not yet completed, it would be premature to begin more complex electrochemistry experiments at this stage. Even once the issues with the optical performance have been resolved, it is not clear whether imaging of a surface through both a layer of electrolyte and a polymer window is feasible. Measurements of the absorption spectra of various copper compounds immersed in sodium sesquicarbonate solution (a treatment commonly used by conservators for the passivation of corrosion in copper-based artefacts) have already been carried out using ODXAS1 [15]. Samples were held in the filled eCell behind a 10 μm thick low-density polyethelene (LDPE) window such that a $\sim$ 125 μm layer of electrolyte covered the surface of the sample. It was determined that the window itself had no discernible effect on the measured signal, but the presence of the liquid was found to cause a considerable increase in noise levels and it also introduced an additional background signal as a result of XEOL emission from the sodium salt solution. An additional complication when extending this approach to the imaging system of XEOM1 will be the effect of the window bulge (from hydrostatic pressure within the sealed eCell) causing the liquid layer to act as an additional lens. This will likely introduce distortion into the resulting images and may be difficult to compensate for since a reliable method of reproducing particular window deformations has not yet been found. Nevertheless, if XEOM1 and eCell can indeed be used together, there is great potential for gaining further insights into the behaviour of dynamic corrosion processes.

For example, time-lapse XRD measurements have previously been used to monitor the conversion of nantokite corrosion on a copper coupon into cuprite through exposure to sodium sesquicarbonate using the eCell [16, 17]. It was noted upon visual inspection that the surface modification occurred inhomogeneously, but this is not apparent from the XRD patterns due to the averaging effect of using a large footprint X-ray beam. However, if XEOM measurements could be carried out with sufficient time resolution they could potentially reveal exactly how the conversion of nantokite to cuprite progresses.

5.7 Beyond Heritage Science

Development of XEOM1 has so far been driven by its potential applications in heritage science, particularly in the area of surface corrosion and prevention thereof. Of course, there are a huge number of other fields in physics, chemistry, and biology where chemical mapping techniques are already in use, and many of these represent areas in which XEOL microscopy could be applied.

Results presented in this thesis already demonstrate the applicability of the technique to measurements of semiconductor materials (see Section 4.6.1) and the use of scanning probe XEOL mapping of nano-scale structures has already been reported elsewhere [18]. Full-field XEOL microscopy will be able to obtain the same information, but is better suited to imaging a comparatively large area (on the order of millimetres) at micron-scale resolution and may avoid the potential for radiation damage induce by high flux density micro/nanoprobe measurements. XAFS is commonly used in the study of catalysts [19] where surface chemistry on the micron scale is of interest [20]; the strengths of XEOL microscopy are well suited to performing such measurements. Corrosion occurs in materials manufactured today [21] and brings with it many of the same surface chemistry challenges as have already been discussed, so naturally XEOL microscopy is equally well suited to meet these challenges as it is for corrosion in heritage artefacts.

These scientific fields represent only a few possibilities for areas in XEOL microscopy could be of use, but serve to demonstrate the wide variety in potential applications for the technique. Ultimately, XEOL microscopy can potentially be of use in any area where there is a desire for surface specific chemical mapping and the types of complementary information provided by the technique are of interest.

5.8 Summary

In this final chapter a number of areas for continued work were identified. Some of these relate directly to the XEOM1 hardware such as the addition of spectroscopy capabilities for identification of specific XEOL emission lines, a re-engineering of the optical system in order to try and improve performance, and the automation of the filter changing mechanism. Others relate to the more general field of XEOL microscopy such as the impact of the synchrotron X-ray beam on the samples (particularly in relation to heritage science), routes for improvement of data processing methods, and the potential for measurement of dynamic chemical processes. Finally, the application of a XEOL microscope to other scientific areas was discussed.

References

[1] C Palmer. *Diffraction Grating Handbook*. Newport Corporation, 6th edition, 2005.

[2] E G Loewen and E Popov. *Diffraction Gratings and Applications*. CRC Press, 1997.

[3] Edmund Optics. URL http://www.edmundoptics.com/.

[4] A Bianconi, D Jackson, and K Monahan. Intrinsic luminescence excitation spectrum and extended x-ray absorption fine structure above the K edge in CaF2. *Phys. Rev. B*, 17(4):2021, 1978.

[5] Princeton Instruments. URL http://www.princetoninstruments.com/.

[6] E Dooryhée, et al. Non-destructive synchrotron X-ray diffraction mapping of a Roman painting. *Appl. Phys. A*, 81(4):663–667, June 2005.

[7] J Dik, et al. Visualization of a lost painting by Vincent van Gogh using synchrotron radiation based X-ray fluorescence elemental mapping. *Anal. Chem.*, 80(16):6436–42, 2008.

[8] K Janssens, et al. The use of synchrotron radiation for the characterization of artists' pigments and paintings. *Annu. Rev. Anal. Chem.*, 6:399–425, January 2013.

[9] M Wilke, et al. The oxidation state of iron determined by Fe K-edge XANES - application to iron gall ink in historical manuscripts. *J. Anal. At. Spectrom.*, 24(10):1364, 2009.

[10] A Adriaens, et al. Real time observation of X-ray induced surface modification using simultaneous XANES and XEOL-XANES. *Anal. Chem.*, 85(20): 9556–9563, 2013.

[11] N Grassi, et al. Differential PIXE measurements for the stratigraphic anal-

ysis of the painting "Madonna Dei Dusi" by Leonardo da Vinci. *PIXE 2004*, pages 843.1–834.3, 2004.

[12] P A Mandò and M G Dowsett. Personal communication.

[13] G Bunker. *Introduction to XAFS: A Practical Guide to X-ray Absorption Fine Structure Spectroscopy*. CUP, 2010.

[14] SR Wasserman and PG Allen. EXAFS and principal component analysis: a new shell game. *J. Synchrotron Radiat.*, 6:284–286, 1999.

[15] M G Dowsett, et al. Optically detected X-ray absorption spectroscopy measurements as a means of monitoring corrosion layers on copper. *Anal. Chem.*, 80(22):8717–24, 2008.

[16] M G Dowsett and A Adriaens. Cell for simultaneous synchrotron radiation X-ray and electrochemical corrosion measurements on cultural heritage metals and other materials. *Anal. Chem.*, 78(10):3360–5, May 2006.

[17] K Leyssens, et al. Simultaneous in situ time resolved SR-XRD and corrosion potential analyses to monitor the corrosion on copper. *Electrochem. Commun.*, 7(12):1265–1270, 2005.

[18] G Martínez-Criado, et al. Scanning X-ray excited optical luminescence microscopy in GaN. *Appl. Phys. Lett.*, 89(22):221913, 2006.

[19] Y Iwasawa, editor. *X-Ray Absorption Fine Structure for Catalysts and Surfaces*. World Scientific, 1996.

[20] S O Krabbenborg, et al. Reactivity mapping with electrochemical gradients for monitoring reactivity at surfaces in space and time. *Nat. Commun.*, 4 (2):1667, January 2013.

[21] M A Baker. The application of surface imaging techniques to the study of pitting corrosion initiation in stainless steels. *Surf. Interf. Anal.*, 20:535–543, 1993.

Chapter 6

Conclusions

6.1 Project Summary

Development of XEOM1 has required a significant amount of design and construction work. A set of custom optics have been designed to meet the requirements imposed by the application to full-field XEOL measurement with the most significant of these being the need to maximise captured photon flux, the requirement of a long working distance in order to allow access for the X-ray beam, and the restriction on optical glass to one which does not itself exhibit XEOL emission. The optical column housing these components not only provides a light-tight environment for the optics, but also supports multiple detectors — including the primary CCD camera — and a variety of auxiliary hardware components.

A great deal of work has also gone into implementing the control system for XEOM1. The obsolescence of several components used in the ODXAS1 system forced an upgrade to more modern hardware. This required that the useful functionality of the old system (primarily that relating to operation of the eCell) be re-implemented, while also expanding its capabilities in order to operate the new hardware associated with XEOM1. In fact, this has allowed a number of previously separate components to be consolidated into a single multi-purpose electronics interface unit so the newer system is actually more compact, despite the greatly expanded capacity. A significant update has also been made to the control software, *eCell Controller*, in order to accommodate the new hardware, and to provide the interface for operating XEOM1 in a number of different experimental modes.

A crucial achievement with regard to the portability of the instrument was the synchronisation mechanism developed for acquisition of image stacks. Without synchronisation it would be extremely difficult to reliably capture image data which is suitable for extraction of XANES spectra. Importantly, it was possible to develop a synchronisation method which is sufficiently decoupled from the beamline system that it should be possible to use XEOM1 on any beamline provided that a single line is available to either (a) send a pulse to initiate stepping of the monochromator, or (b) receive a pulse to inform the XEOM system that the monochromator has stepped and is ready for the next data point.

Several obstacles have been encountered during development of XEOM1. It was discovered that the FLI CCD camera initially used as the primary imaging detector has some serious flaws. Defects with the CCD sensor itself were found to introduce imaging artefacts and poor hermetic seal has allowed dust to enter the sensor cavity. An upgrade of the camera an Andor large-area sensor unit has resolved these issues.

It has also been found that, when using the existing combination of optics and filtering, the X-ray absorption spectra extracted from ROIs are generally lacking in significant chemical differentiation. Features in some extracted spectra have shown hints that other compounds are present (typical for a mixture), but it is be expected that spectra from ROIs containing completely different compounds would be totally distinct and this is clearly not the case. Despite this, it has still been possible to demonstrate the application of several analysis methods to the data acquired using XEOM1.

Producing a pre-edge/post-edge difference image is a simple and fast method for elemental mapping since only two images are required. While the example given in Section 4.6.1 required a long exposure time (over 30 min) due to the weakly emitting sample, difference maps for more strongly emitting compounds, e.g. cuprite, could be produced in a matter of seconds. Additionally, examination of ROI-extracted XEOL spectra has still enabled some insight to be gained into the changes in electron decay and photon emission processes for cuprite and nantokite around the Cu edge. It has been found that the use of processing techniques routinely applied to conventional XAS data (conversion to normalised $\mu(E)$ via spline fitting and background subtraction) can introduce significant distortion of certain features, particularly those on the edge itself. Reverting back to the inspection of raw (normalised) spectra actually reveals that information is lost when additional processing is applied.

The acquisition times required to collect sufficient light from a sample in order to produce an image of the surface have been found to vary a great deal. If the emission is unfiltered, exposure times of 1 s or less are often sufficient (cuprite and nantokite are particularly strong emitters). However, the use of filters, which is currently a requirement for extracting chemical information, increases exposure times dramatically. In many cases at least 20 s is required, in some cases several minutes is sufficient, but in extreme cases exposure times of over 30 min have been necessary. This currently limits the analysis of samples which require long exposure times to difference mapping and single filtered images comparison. Only when the exposure time is, at most, on the order of a few minutes is the acquisition of an image stack a viable option. Even then, a relatively small energy range (56 eV) over the XANES region can still take several hours to acquire.

6.2 Beam Time Allocations

Aspects of this project highlight the difficulty of developing new instrumentation for a synchrotron-based technique without frequent access to a beamline. Set-up of XEOM1 and its auxiliary components, plus alignment and optimization of the X-ray beam typically consumes half a day of beam time. Additionally, several beam time allocations on XMaS were split: part of the time was available for XEOM experiments, but the remaining time was dedicated to XRD measurements utilizing the 2D MarCCD 165 detector (Marresearch GmbH, Norderstedt, Germany). While these experiments are generally more straightforward so set-up and measurement times are much shorter, they still amounted to several days beam time unavailable for XEOM testing.

Fortunately, it has been possible to deploy XEOM1 at seven beam time allocations, most of which have been a full 15 shifts (5 days). Also, we have a good working relationship with the staff from the XMaS beamline — XMaS is managed jointly by the University of Liverpool and the University of Warwick —

so there have been several occasions on which we have been given the opportunity to set up the instrumentation on the day prior to the start of our beam time allocation, easing the set-up time issue.

An additional complication which has been encountered is related to the operating mode of the synchrotron storage ring. The maximum operating current of the storage is 200 mA which generates the highest available photon fluxes in the beamlines. Given the low signal levels detected when measuring filtered XEOL emission, it is usually desirable to use the highest photon flux available. We have been fortunate to have had most beam time allocations during periods where the storage ring is operating in a high current mode, most commonly 7/8 + 1 (868 electron bunches in 7/8 of the ring, and single 2 mA bunch in the middle of the remaining 1/8 gap); a request for an allocation during operation in a particular mode can be included as part of the beam time proposal. However, two beam time allocations have occurred when the storage ring was operating in 16 bunch mode (16 equally-space electron bunches) with a maximum current of 90 mA. This represents a more than 50 % loss of flux which correspondingly increases the required data acquisition times. Moreover, the lower current mode results in a shorter electron beam lifetime, so more frequent refills are required. Avoiding running experiments over refill times, which can result in artefacts in the acquired data, is more difficult in this case.

6.3 Implications For Previous Results

The XANES spectrum of nantokite exhibits a very strong white line. Previous measurements of the XEOL emission from nantokite-coated copper coupon showed that the intensity of the white line is dependant on the filter colour, and it was found that the greatest intensity is observed when using the green filter. Upon initial discovery that the Edmund Optics dichroic filters that were used for this experiment (and many more besides) transmitted light in pass bands outside their specifications, there was concern that the conclusions drawn would be made invalid. However, all older experiments were carried out using ODXAS1 with the Hamamatsu PM tube as the primary detector. While this detector is sensitive up to 850 nm, by its quantum efficiency falls below 10 % by 750 nm so the impact of the extra pass bands is minimal.

6.4 Final Thoughts

Development of new scientific instrumentation is an iterative process. The work presented here represents some significant steps towards the end goal of a portable microscopy and spectroscopy instrument capable of producing high quality surface chemical maps. However, there is clearly still much work to be done: improvement of the optics, enhancement of functionality (spectroscopy, filter wheel), and continued development of the supporting software (*eCell Controller* and *esaProject*). Nevertheless, a large portion of the infrastructure for deploying the microscope is now in place. The control system already allows for automation of most of the XEOM1 hardware and is ready to operate additional hardware components as they become available. The adaptability of XEOM1 has been demonstrated through deployment on two different beamlines at the ESRF and few (if any) modifications should be necessary for use on other beamlines in the future. It has also been shown that imaging of XEOL emission from surface corrosion is viable and that through operation in different acquisition modes a great deal of information about the sample can be extracted. Once the previously mentioned improvements to XEOM1 have been made, the study of samples relevant to the development of protection systems for cultural heritage artefacts can begin.

Appendix A

XMaS WAGO Macros

In order to enable triggering of the XMaS beamline system using the XEOM1 hardware some simple macros were written. Macro 1 polls the WAGO box channel into which the XEOM1 trigger signal is sent. If the trigger signal is detected, the polling loop is broken and the macro exits. Queueing Macro 1 so that it runs before the beamline system initiates a measurement on all connected detectors prevents the measurement from occurring until the XEOM1 trigger signal is sent. Queueing and dequeuing of this synchronisation macro is done using Macros 2 and 3 respectively.

Macro 1

```
def wago_trig_wait '{
  local v doit

  while (1) {
    v = wago_readch("trig")

    if (v==1) doit=1

    if ((v==0) && (doit==1)) break
  }
}'
```

Macro 2

```
def wago_trig_on '{
  cdef("measure0","wago_trig_wait;","_wago_trig_wait_")
}'
```

Macro 3

```
def wago_trig_off '{
  cdef("","_wago_trig_wait_","delete")
}'
```